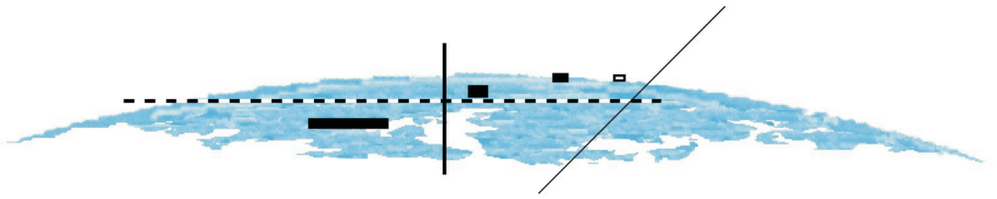

GeoForschungsZentrum Potsdam

in der Helmholtz-Gemeinschaft

Jan Henninges

Thermal Properties of Gas-Hydrate-Bearing Sediments and Effects of Phase Transitions on the Transport of Heat Deduced from Temperature Logging at Mallik, NWT, Canada

Scientific Technical Report STR05/11

Impressum

GeoForschungsZentrum Potsdam
in der Helmholtz-Gemeinschaft
Telegrafenberg
D-14473 Potsdam

e-mail: postmaster@gfz-potsdam.de
www: http://www.gfz-potsdam.de

Gedruckt in Potsdam
Juli 2005

ISSN 1610-0956

Die vorliegende Arbeit ist in elektronischer Form erhältlich unter:
http://www.gfz-potsdam.de/bib/zbstr.htm

Jan Henninges

Thermal Properties of Gas-Hydrate-Bearing Sediments and Effects of Phase Transitions on the Transport of Heat Deduced from Temperature Logging at Mallik, NWT, Canada

---

Von der Fakultät VI:
Bauingenieurwesen und Angewandte Geowissenschaften
der Technischen Universität Berlin
zur Erlangung des akademischen Grades:

Doktor der Naturwissenschaften
Dr. rer. nat.

genehmigte Dissertation

Berlin 2005
D 83

Scientific Technical Report STR05/11

Promotionsausschuss:

Vorsitzender:	Prof. Dr. B. Horsfield
Berichter:	Prof. Dr. H. Burkhardt
Berichter:	Prof. Dr. H. Villinger
Berichter:	Dr. E. Huenges

Tag der wissenschaftlichen Aussprache: 22. April 2005

Acknowledgements

This work was performed at the GeoForschungsZentrum Potsdam and was supported by the German Ministry of Education and Science (BMBF) and Deutsche Forschungsgemeinschaft (DFG) within the framework of the GEOTECHNOLOGIEN program, No. G0556A.

I especially thank Dr. E. Huenges for the initiation and supervision of the project. I am deeply indebted to Prof. Dr. H. Burkhardt, who kindly supervised this thesis and shared many fruitful discussions with me. The willingness of Prof. Dr. H. Villinger, University of Bremen, to examine the thesis is greatly appreciated.

My special thanks are addressed to my colleagues of Section 5.2 'Geothermics' at GFZ Potsdam: Dipl.-Ing. J. Schrötter assisted during the field experiment at Mallik and Dr. K. Erbas introduced me to DTS measurement and data processing technology. I express my gratitude to Dr. E. Spangenberg, Dr. J. Kulenkampff and Dr. G. Zimmermann for many discussions and their critical comments to the manuscript. Furthermore the technical staff at GFZ, C. Karger, S. Meyhöfer and T. Schläfke, supported the performance of numerous DTS calibration measurements.

The Mallik 2002 Gas Hydrate Production Research Well Program participants include seven partners (Geological Survey of Canada (GSC), Japan National Oil Corporation (JNOC), GeoForschungsZentrum Potsdam (GFZ), United States Geological Survey (USGS), United States Department of Energy (USDOE), India Ministry of Petroleum and Natural Gas (MOPNG), BP-Chevron-Burlington joint venture group) and was supported by the International Continental Scientific Drilling Program (ICDP). In this connection I especially want to emphasize the excellent cooperation with our colleagues from the Geological Survey of Canada: I thank S. R. Dallimore, leader of Mallik Science Team, for his active support of the DTS temperature survey at Mallik, and A. E. Taylor for introducing me to the peculiarities of geothermics in permafrost regions. F. M. Nixon, J. F. Wright and the staff at the Inuvik Research Centre provided invaluable logistical support during the October 2002 and September 2003 post-field site visits. Mrs. B. Medioli kindly provided lithological data from sieve and XRD analysis from the Mallik core samples.

I am much obliged to my parents for their continuous love and support.

Abstract

Detailed knowledge about the thermal properties of rocks containing gas hydrate is required in order to quantify processes involving the formation and decomposition of gas hydrate in nature. This work investigates the influence of methane hydrate on the transport of heat in hydrate-bearing rocks. Both the thermal conductivity of gas-hydrate bearing sediments and the thermal effects of phase transitions are analyzed.

In the framework of the Mallik 2002 program three wells penetrating a continental gas hydrate occurrence under permafrost were successfully equipped with permanent fiber-optic distributed temperature sensing cables. Temperature data were collected over a period of 21 months after completion of the wells. The analysis of the disturbed well temperatures after drilling revealed a strong effect of phase transitions on temperature changes. For the first time, the effects of induced temperature changes within a gas hydrate deposit were monitored in-situ. The resulting temperature gradient anomalies could be successfully utilized to determine the base of the gas hydrate occurrences and the permafrost layer at about 1103-1104±3.5 m and 599-604±3.5 m below ground level respectively.

At the end of the 21-month observation period, the well temperature returned close to equilibrium with the formation temperature. At the base of the gas hydrate occurrences a temperature of 12.3 °C was measured, which is about 0.7 K below the stability temperature predicted by thermodynamic calculations considering a pressure gradient of 10.12 kPa m^{-1} and a sea-water salinity of 35 ppt. Under the stated conditions, the base of the stability zone of methane hydrate at Mallik would lie at about 1140 m below ground level.

Thermal conductivity profiles were calculated from the geothermal data as well as from a petrophysical model derived from the available logging data and application of mixing-law models. The results indicate, that variations of thermal conductivity are mainly lithologically controlled with a minor influence from hydrate saturation. The results of the geometric mean model showed the best agreement to the thermal conductivity profiles derived from geothermal data. Average thermal conductivity values of the hydrate-bearing intervals range between 2.35 W m^{-1} K^{-1} and 2.77 W m^{-1} K^{-1}.

A simplified numerical model of conductive heat flow was set up in order to assess the temperature effect of phase transitions within the gas hydrate bearing strata. Within the model the mobilization of latent heat during the phase transition was considered (enthalpy method), taking into account the stability conditions for methane hydrate at Mallik (pressure, temperature, pore fluid and gas phase composition) as well as effects of hydrate decomposition on the thermal rock properties. The modelling results indicate, that the regeneration of hydrate after the recovery of stability conditions is inhibited.

Kurzfassung

Um Prozesse im Zusammenhang mit der Bildung und der Zersetzung von Gashydraten in der Natur quantifizieren zu können, ist eine detaillierte Kenntnis der thermischen Eigenschaften von gashydratführenden Gesteinen notwendig. Diese Arbeit untersucht den Einfluss von Methanhydrat auf den Wärmetransport in porösen Gesteinen. Sowohl die Wärmeleitfähigkeit gashydratführender Sedimente als auch der Einfluss von Phasenübergängen wird untersucht.

Im Rahmen des Mallik 2002 Forschungsbohrprogramms wurden drei Bohrungen, die ein kontinentales Gashydratvorkommen unter Permafrost durchteufen, erfolgreich mit faseroptischen Messkabeln zur ortsverteilten Temperaturmessung ausgestattet. Über einen Zeitraum von 21 Monaten nach der Fertigstellung der Bohrungen wurden Temperaturmessungen durchgeführt. Die Auswertung der durch den Bohrprozess verursachten Temperaturstörungen zeigt einen starken Einfluss von Phasenübergängen auf Temperaturänderungen. Erstmals wurden die Auswirkungen einer künstlich induzierten Temperaturänderung innerhalb eines natürlichen Gashydratvorkommens in situ beobachtet. Die hierdurch verursachten Anomalien des Temperaturgradienten wurden erfolgreich zur Bestimmung der Basis der Gashydratvorkommen und des Permafrosts herangezogen, die jeweils bei rund 1103-1104±3.5 m, bzw. 599-604±3.5 m unterhalb der Geländeoberkante liegen.

Am Ende des 21-monatigen Beobachtungszeitraumes hat sich die Bohrlochtemperatur weitgehend der Formationstemperatur angeglichen. An der Basis der Gashydratvorkommen wurde eine Temperatur von 12.3 °C bestimmt. Dieser Wert liegt rund 0.7 °C unter der von thermodynamischen Berechnungen vorhergesagten Stabilitätstemperatur, wenn man von einem Druckgradienten von 10.12 kPa m^{-1} und einer Salinität des Porenwassers von 35 ppt ausgeht. Unter den angegebenen Bedingungen liegt die Grenze des Stabilitätsbereichs von Methanhydrat bei ungefähr 1140 m unter Gelände.

Profile der Wärmeleitfähigkeit wurden sowohl aus geothermischen Daten als auch aus einem petrophysikalischen Modell, welches aus den vorliegenden Bohrlochmessdaten abgeleitet wurde, und der Anwendung von Mischungsgesetzmodellen berechnet. Die Ergebnisse weisen darauf hin, dass Veränderungen der Wärmeleitfähigkeit im Wesentlichen durch lithologische Wechsel verursacht werden. Der Einfluss der Hydratsättigung ist nur von untergeordneter Bedeutung für die effektive Wärmeleitfähigkeit des Gesteins. Die Ergebnisse des geometrischen Mittel Modells stimmen am besten mit den Wärmeleitfähigkeitsprofilen, die aus geothermischen Daten abgeleitet wurden, überein. Mittlere Werte der Wärmeleitfähigkeit der hydratführenden Intervalle liegen zwischen 2.35 W m^{-1} K^{-1} und 2.77 W m^{-1} K^{-1}.

Ein vereinfachtes numerisches Modell für konduktiven Wärmetransport wurde eingesetzt, um den Temperatureffekt von Phasenübergängen in den gashydrathaltigen Schichten zu berechnen. Das Modell beinhaltet die Umsetzung latenter Wärme während des Phasenübergangs (Enthalpie-Methode); Weiterhin wurden die Stabilitätsbeding-

ungen für Methanhydrat in Mallik (Druck, Temperatur, Zusammensetzung des Porenwassers und der Gasphase) und der Einfluss der Zersetzung von Hydrat auf die thermischen Gesteinseigenschaften berücksichtigt. Die Modellergebnisse deuten darauf hin, dass die Neubildung von Hydrat nach Wiedererlangen der Stabilitätsbedingungen gehemmt ist.

Contents

Acknowledgements iii

Abstract iv

Kurzfassung v

List of Figures ix

List of Tables xi

List of Abbreviations xii

1. Introduction 1
- 1.1. Motivation . . . 1
- 1.2. State of the Art . . . 2
- 1.3. Contributions Made in this Work . . . 5

2. The Geology at Mallik in a Regional Context 7
- 2.1. Regional geology . . . 7
- 2.2. Geology at Mallik . . . 9
- 2.3. Temperature Field and Permafrost . . . 10
- 2.4. Gas Hydrate Occurrences . . . 15

3. Distributed Temperature Measurements at Mallik 18
- 3.1. The Method of Distributed Temperature Sensing . . . 18
- 3.2. Calibration and Accuracy of the DTS 800 M10 . . . 21
- 3.3. Temperature Logging at Mallik . . . 24
- 3.4. Post-processing of DTS Temperature Data . . . 26
- 3.5. Geothermal Conditions and Influences by Drilling . . . 31

4. Estimation of the In-situ Thermal Conductivity 44
- 4.1. Methods for the Determination of Thermal Conductivity . . . 44
- 4.2. A Petrophysical Rock Model from Logging Data . . . 44
- 4.3. Thermal Conductivity Profiles from Mixing Law Models . . . 48
- 4.4. Thermal Conductivity Profiles from Geothermal Gradient . . . 54
- 4.5. Comparison of Calculated Thermal Conductivity Profiles . . . 57

5. A Simplified Model for Methane Hydrate Destabilization **59**
5.1. Physical Reaction and Properties 59
5.2. Volumetric Balance 59
5.3. Stability Conditions for Methane Hydrate at Mallik 62
5.4. Stability Zone for Methane Hydrate at Mallik 64

6. Numerical Simulation of the Temperature Effect of Phase Transitions **67**
6.1. Simulation Scenarios 67
6.2. The Stefan Problem and the Enthalpy Method 67
6.3. Set-up of the Numerical Model 69
6.4. Boundary Conditions and Discretization of Time 72
6.5. Modelling Results 75
6.6. Discussion 80

7. Summary and Conclusions **81**

A. Photo Documentation **84**

B. Geophysical Well Logs of Mallik 3L-38, 4L-38, and 5L-38 **88**

C. Details of Drilling and Cementing Operations, Mallik 3L-38 Well **95**

D. Simulation Results: Horner Plots of Calculated Temperatures **101**

E. Simulation Results: Radial Profiles of Calculated Temperatures **106**

Bibliography **111**

List of Figures

1.1. Global map of known and inferred gas hydrate occurrences 3
1.2. Stability diagrams for gas hydrates 4
1.3. Thermal conductivity of gas, water, ice, and hydrates 5

2.1. Location map of the Mackenzie Delta - Beaufort Sea area 8
2.2. Upper Cretaceous to Holocene sequence stratigraphy 8
2.3. Reflection seismic profile 9
2.4. Geophysical well logs of Mallik 2L-38 11
2.5. Depth to the base of the ice-bearing permafrost 13
2.6. Photo of core sample with visible gas hydrate 17

3.1. Functional diagram of an optical time-domain reflectometer 19
3.2. Schematic spectrum of scattered light 19
3.3. Raman anti-Stokes back-scatter signal as a function of temperature . . . 20
3.4. Single-ended and double-ended DTS measurement configurations 21
3.5. Example of DTS calibration measurement results 22
3.6. DTS temperature resolution as a function of integration time 23
3.7. Map of the Mallik site and well locations 24
3.8. Schematic cross section of the field experiment 25
3.9. Cable clamp for the installation of DTS cables 26
3.10. Frequency spectrum of measured DTS temperature data. 29
3.11. Comparison of raw and filtered DTS temperature data 29
3.12. Temperature differences of successive DTS temperature profiles 30
3.13. Horner-plot of measured temperatures, Mallik 3L-38 and 4L-38 33
3.14. Temperature profiles and temperature gradient, Mallik 3L-38 37
3.15. Temperature profiles and temperature gradient, Mallik 4L-38 38
3.16. Temperature profiles and temperature gradient, Mallik 5L-38 39
3.17. Geothermal gradients, lithological units and hydrate saturation 40
3.18. Detail temperature and gradient, base IBPF 42
3.19. Detail temperature and gradient, base GHZ 42

4.1. Model for hydrate-bearing sediment 45
4.2. Thermal conductivity profiles from mixing law models 52
4.3. Thermal conductivity profiles calculated from geothermal data 56
4.4. Comparison of thermal conductivity profiles 58

5.1. Volumetric balance of phases within the pore space 61
5.2. Stability diagram for methane hydrate at Mallik 66

6.1. Schematic enthalpy-temperature curve 68
6.2. Schematic diagram of the 2D-axisymmetric model domain 69
6.3. Finite element model mesh 70
6.4. Time-history plot of calculated temperatures (Scenario A) 76
6.5. Calculated temperature profiles and temperature gradients (Scenario A) 76
6.6. Time-history plot of calculated temperatures (Scenario B1) 78
6.7. Calculated temperature profiles and temperature gradients (Scenario B1) 78
6.8. Calculated temperature profiles and temperature gradients (Scenario B2) 79
6.9. Calculated temperature profiles and temperature gradients (Scenario B3) 79

A.1. Calibration of DTS system 85
A.2. The Mallik drilling rig during the thermal stimulation experiment 85
A.3. Installation of DTS cables 86
A.4. Wireline DTS log with combined P/T memory tool 86
A.5. Steel box for the protection of the surface ends of the DTS cables 87
A.6. Long-term DTS monitoring 87

B.1. Correlation of gamma-ray logs of Mallik 3L-38, 4L-38, and 5L-38 wells . 89
B.2. Gamma-ray logs and computed shale content 90
B.3. Thorium-Potassium cross plot 91
B.4. Apparent porosity and gas hydrate saturation, 880-1000m interval . . . 92
B.5. Apparent porosity and gas hydrate saturation, 1000-1120m interval . . . 93

C.1. Drilling mud temperatures, Mallik 3L-38 well 96
C.2. Drilling report, Mallik 3L-38 well, Jan. 5, 2002 (p. 1) 97
C.3. Drilling report, Mallik 3L-38 well, Jan. 5, 2002 (p. 2) 98
C.4. Drilling report, Mallik 3L-38 well, Jan. 6, 2002 (p. 1) 99
C.5. Drilling report, Mallik 3L-38 well, Jan. 6, 2002 (p. 2) 100

D.1. Horner plot (Scenario A) 102
D.2. Horner plot (Scenario B1) 103
D.3. Horner plot (Scenario B2) 104
D.4. Horner plot (Scenario B3) 105

E.1. Radial temperature profiles (Scenario A) 107
E.2. Radial temperature profiles (Scenario B1) 108
E.3. Radial temperature profiles (Scenario B2) 109
E.4. Radial temperature profiles (Scenario B3) 110

List of Tables

2.1. Depth of sequence boundaries at Mallik 10
2.2. Lithological units of cored interval of Mallik 5L-38 12
2.3. Depth of ice-bearing permafrost at Mallik 14
2.4. Depth of gas hydrate occurrences at Mallik 17

3.1. Comparison of DTS and electronic memory tool temperatures 22
3.2. Well completion and DTS installation statistics at Mallik 25
3.3. Summary of drilling operations and DTS logging schedule at Mallik . . 26
3.4. Reference depths for correlation of DTS data 28
3.5. Horner-plot data, Mallik 3L-38 34
3.6. Horner-plot data, Mallik 4L-38 34
3.7. Temperature profile data, depths of permafrost and hydrate occurrences 43

4.1. Physical properties of selected minerals 46
4.2. Average mineral composition of shale 47
4.3. Major log-derived gas hydrate intervals at Mallik 5L-38 49
4.4. Thermal conductivities of components for mixing law models 51
4.5. Average calculated thermal conductivity values 53

5.1. Physical properties of structure I methane hydrate 60
5.2. Average hydrate gas composition at Mallik 64
5.3. Equilibrium temperatures for methane hydrate at 11.25 MPa 65

6.1. Description of simulation scenarios 67
6.2. Thermal input parameters 71
6.3. Non-linear material model for hydrate-bearing sediment 71
6.4. Loadsteps and applied boundary conditions 74
6.5. Simulated temperature gradient anomalies 77

B.1. Coal and dolomite cemented sandstone layers 94

List of Abbreviations

Symbol	Definition
A	Slope of linear fit in Horner plot (K)
BHT	Bottom-hole temperature (°C)
$c_{(T)}$	Specific heat capacity (J kg^{-1} K^{-1})
CBT	Cement-bond tool
CCL	Casing-collar-locator log
CEC	Cation exchange capacity
CGR	Computed gamma ray intensity, corrected for Uranium content (API)
d, Δ	Incremental change
dz	Vertical distance (m)
D_{corr}	Corrected distance of DTS data points (m)
DMR	Density-magnetic-resonance method
$DPHI$	Gamma-gamma density log apparent porosity
DST	Drill-stem test
DTS	Distributed temperature sensing
FFT	Fast Fourier transformation
g	Acceleration of gravity (m s^{-2})
Γ	Geothermal gradient (K m^{-1})
GHZ	Gas hydrate zone
GR	Gamma-ray intensity (API)
GR_{max}	Maximum gamma-ray intensity, corresponding to shale (API)
GR_{min}	Minimum gamma-ray intensity, corresponding to clean sand (API)
GRI	Gamma-ray index
h	Height of water column (m)
H	Enthalpy (J m^{-3})
H_{bot}	Depth of lowermost DTS data point (m)
H_{ref}	Elevation of uppermost DTS data point relative to common depth datum (m)
H_{top}	Depth of uppermost DTS data point (m)
HFK	Potassium (K) concentration (%)
$HGEN$	Heat generation rate boundary condition (W m^{-3})
HNGS	Hostile natural gamma ray sonde
HSGR	Standard gamma ray intensity (API)
HTHO	Thorium (Th) concentration (ppm)
IBPF	Ice-bearing permafrost
K_e	Kersten's number (-)
λ	Thermal conductivity (W m^{-1} K^{-1})
λ_{ari}	Effective thermal conductivity, arithmetic mean model (W m^{-1} K^{-1})
λ_{geo}	Effective thermal conductivity, geometric mean model (W m^{-1} K^{-1})

Symbol	Definition
λ_{har}	Effective thermal conductivity, harmonic mean model (W m^{-1} K^{-1})
λ_n	Thermal conductivity of n-th component (W m^{-1} K^{-1})
λ_{zz}	Thermal conductivity in vertical direction (W m^{-1} K^{-1})
L	Latent heat of phase transition (J m^{-3})
L1	Non-hydrate-bearing layer
L2	Hydrate-bearing layer
LS	Load step number
mGL	Depth below ground level (m)
mKB	Depth below rotary kelly bushing (m)
mSL	Elevation above sea level (m)
m_x	Molecular weight of component x per formula unit (g $mole^{-1}$)
M	Guest molecule
M_x^h	Mass fraction of component x stored in hydrate (-)
M.L.C.	Mixed layer clays
n	Total number of DTS data points
n_i	Weight fraction of i-th component relative to total weight
N	Hydration number
NMR	Proton nuclear magnetic resonance
OTDR	Optical time-domain reflectometry
ϕ	Porosity
P	Pressure (Pa)
P_0	Atmospheric pressure (Pa)
q	Rate of heat flow per unit area (heat-flow density) (W m^{-2})
Q	Heat flow per unit length of borehole (W m^{-1})
r	Distance in radial (r-z-coordinates) direction (m)
ρ	Density (kg m^{-3})
RAV	Running average
σ	Standard deviation, standard error
S	Initial in-situ salinity (ppt)
S^*	Salinity after hydrate decomposition (ppt)
S_h	Gas hydrate saturation, relative to pore volume
S_w	Water saturation, relative to pore volume
S_w^*	Partial water saturation after hydrate decomposition
t	Time (s)
t_s	Shut-in time (s)
t_c	Circulation time (s)
T	Temperature (°C)
T_∞	Equilibrium temperature (°C)
TCMR	Magnetic-resonance log apparent porosity
$TEMP$	Temperature degree of freedom within numerical calculations (°C)
TGY	Calculated temperature gradient in vertical (axial) direction (K/km)
TVD	True vertical depth (m)
V	Volume (m^3)
v_n	Ratio of volume of n-th component to total volume (-)

Symbol	Definition
v_x^h	Volume of component x per unit volume of sediment (-)
V_m^*	Relative amount of methane gas retained in the sediment
V_{sh}	Shale content, relative to total volume (or weight) of rock matrix
V_x^h	Volume of component x per unit volume of hydrate (-)
x_i	Depth of DTS measurement point (m)
z	Distance in vertical (cartesian coordinates) or axial (r-z-coordinates) direction (m)
z_{DTS}	Depth of DTS data point (m, relative to common depth datum)

List of Indices

Symbol	Definition
cmt	Cement slurry
dry	0 % water saturation
dol	Dolomite
h	Hydrate
i	Index number of DTS data point
m	Methane
ma	Rock matrix
sat	100 % water saturation
sd	Sand
sh	Shale
w	Water or pore fluid
z	Vertical direction

1. Introduction

1.1. Motivation

Worldwide vast volumes of methane could be stored in naturally occurring gas hydrates, a crystalline solid predominantly composed of methane and water. Possible implications on human welfare exist, because natural gas hydrate is a potential

- future energy resource (methane = abundant and 'clean' fuel)
- climate factor (methane = efficient greenhouse gas)
- geohazard (stability of continental slopes, drilling hazard).

In the past 30 years a growing number of studies were dedicated to the investigation of natural gas hydrates. Nevertheless the major questions about gas hydrates are still not fully resolved: What is the global volume of methane stored in gas hydrates? What is the role of gas hydrate in the global carbon cycle and its effect on climate? Is the production of methane from gas hydrates economically feasible?

In order to address these questions, more knowledge about the geological conditions under which gas hydrates are occurring and appropriate geophysical exploration methods has to be gained. The Mallik 2002 Gas Hydrate Production Research Well Program [1] (hereafter referred to as the *Mallik 2002 program*) was set up in order to investigate the in-situ conditions of one of the most concentrated gas hydrate occurrences currently known, located at the coast of the Mackenzie Delta, Northwest Territories, Canada. The scientific results of the Mallik 2002 program are compiled in a compendium volume (*Dallimore and Collett*, 2005) with contributions of over 100 researchers from over 30 research institutes, which also contains excerpts of the work in hand (*Henninges et al.*, 2005a).

Temperature is of outstanding importance for the stability of gas hydrates. Detailed studies of the in-situ temperature field of gas hydrate occurrences are required in order to evaluate the stability conditions. Experiments have to be designed in order to monitor the effects of dynamic changes of the stability conditions as a result of external forcing. Within recent years, fiber-optic distributed temperature sensing (DTS) has been introduced as a new technology for the measurement of temperature in boreholes. The experimental data serves for the derivation of petrophysical parameters and the calibration of numerical simulators for the prediction of processes involving the formation and decomposition of gas hydrates.

[1] The Mallik 2002 program participants included seven partners (Geological Survey of Canada (GSC), Japan National Oil Corporation (JNOC), GeoForschungsZentrum Potsdam (GFZ), United States Geological Survey (USGS), United States Department of Energy (USDOE), India Ministry of Petroleum and Natural Gas (MOPNG), BP-Chevron-Burlington joint venture group) and was supported by the International Continental Scientific Drilling Program (ICDP).

Apart from the importance for the subsurface temperature field, the thermal properties of hydrate bearing rocks are a controlling factor for all processes involving the formation and decomposition of gas hydrate in nature, which are inevitably coupled with the transport of heat within the formation. The thermal conductivity of pure hydrate is about 20 % lower than the thermal conductivity of water, and up to 80 % lower than that of ice (Figure 1.3). Because of the low thermal conductivity of pure hydrate it has often been proposed, that the presence of gas hydrate should have a significant influence on the bulk rock thermal conductivity and the geothermal gradient within hydrate-bearing formations (e.g. *Ruppel*, 2000). But the influence of hydrate composition and micro-structure, as well as the saturation within a porous medium on the bulk rock thermal conductivity has not been determined yet.

1.2. State of the Art

1.2.1. Gas Hydrate Occurrences and Distribution Worldwide

Gas hydrate deposits are known and inferred to occur at a number of locations worldwide (Figure 1.1), which can be grouped into two different categories:

a) Continental polar regions

b) Submarine continental slopes and rises

Estimates of the global volume of methane stored in gas hydrates are varying about three orders of magnitude. *Kvenvolden* (1988) favors a rather conservative estimate of the global inventory of about 1×10^4 Gt (1 gigaton = 1×10^{12} kg) of methane carbon, which is equivalent to about 2×10^{16} m^3 of methane gas under standard conditions. This amount greatly exceeds the amounts of other components of the global carbon cycle, and it is about twice as high as the total amount of carbon in all other fossil fuel deposits, which are estimated to a sum of about 5×10^3 Gt.

At Mallik, gas hydrate accumulations occur within a sedimentary succession between about 800 m and 1,100 m below ground level (see Section 2.4), which is overlain by a thick permafrost layer extending to a depth of about 600 m below ground level (see Section 2.3). Although up to about 20 % of the global gas hydrate volume is attributed to continental permafrost-associated gas hydrate occurrences, knowledge about especially this kind of deposit is yet sparse.

1.2.2. Factors Controlling Gas Hydrate Stability

The size and distribution of natural methane hydrate occurrences and the release of gaseous methane through the decomposition of methane hydrate are predominantly controlled by the subsurface pressure and temperature conditions (e.g. *Ruppel*, 2000). Generally, the gas hydrate stability zone (GHSZ) at a given location is limited to the interval where the temperature-depth profile intersects and remains below the stability curve for methane hydrate (Figure 1.2).

Some details of the physical reaction leading to the formation of gas hydrates, their composition, structure and physical behavior are reviewed in Chapter 5.

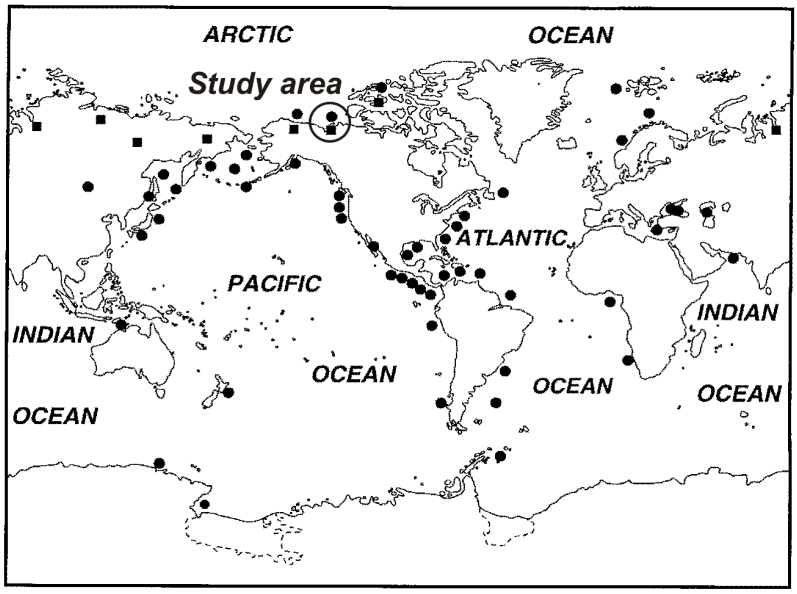

Figure 1.1.: Global map of known and inferred gas hydrate occurrences in oceanic regions of the outer continental margins (circles) and in continental permafrost regions (squares). Location of the Mackenzie Delta - Beaufort Sea region marked with circle. Modified from *Kvenvolden* (1999).

Until the Mallik 2002 project, only a very limited amount of data from field-scale experiments for the investigation of the response of a hydrate occurrence to external forcing under controlled conditions was available. *Bily and Dick* (1974) have published some results of closed chamber tests which were performed within hydrate-bearing intervals in two Mackenzie Delta wells in 1972. The Messoyakha field in the northeast of western Siberia has often been referenced as a site where gas might have been produced from a natural gas hydrate occurrence (*Sloan*, 1998, p. 525-533). Since 1969 gas from a reservoir overlain by gas hydrates was produced, and the depressurization of the reservoir could have induced decomposition of the gas hydrates. The contribution of gas from hydrate decomposition is nevertheless still a matter of ongoing discussion.

1.2.3. Thermal Properties

The direct measurement of thermal conductivity on hydrate-bearing rock samples is generally hampered by the difficulties and uncertainties arising from possible degradation of hydrate during sample retrieval and preparation. Furthermore measurements have to be performed under in-situ conditions in order to maintain the proportion of the phases present within the pore space.

The thermal conductivity of pure methane hydrate was determined as 0.45 W m^{-1} K^{-1} at 216.2 K (*Cook and Leaist*, 1983). But until now, there is a lack of thermal conductivity data measured on rock samples and only a limited number of laboratory measurements on artificially produced samples have been published.

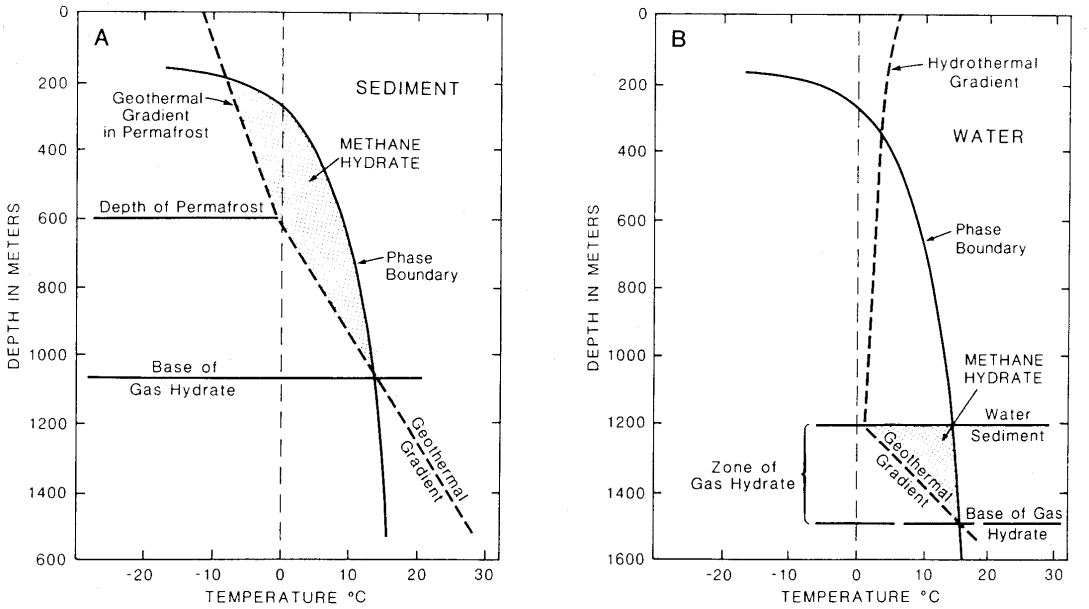

Figure 1.2.: Stability diagrams for gas hydrates in a continental permafrost setting (A) and a marine continental margin setting (B) (from *Kvenvolden*, 1988).

Stoll and Bryan (1979) performed measurements of the thermal conductivity of mixtures of sand, water, gas and hydrate. They concluded, that the thermal conductivity of a propane hydrate saturated sand with 40 % porosity was reduced about 23 % compared to water saturated conditions. Figure 1.3 contains a compilation of most of the data published until 1998. Measurements performed on samples of hydrate in sediment in general yielded values similar to those performed on samples of water in sediment, with values of about 2.5 - 3.0 W m^{-1} K^{-1}.

Waite et al. (2002) performed measurements of thermal conductivity on porous mixtures of methane hydrate and quartz sand with varying percentages of hydrate content. On the basis of their observations *Waite et al.* (2002) concluded, that the bulk rock thermal conductivity was influenced by two different effects: Increases of the bulk rock thermal conductivity were interpreted as the result of enhanced intergranular contact, while decreases were attributed to the low thermal conductivity of the hydrate itself.

The specific heat capacity and the enthalpy of decomposition of methane hydrate have been determined within a number of different laboratory studies (e.g. *Rueff et al.*, 1988, see Section 5.1).

1.2.4. Numerical Simulation of Hydrate Formation and Decomposition

Since the early 1980s, various methods for the modelling of gas hydrate decomposition and formation processes have been developed. An overview of the methods and models deployed for investigating the recovery of gas from hydrated reservoirs is contained in *Sloan* (1998, p. 513-525). Numerical models have been developed to predict the effects of changes in pressure (depressurization), temperature (thermal stimulation), or

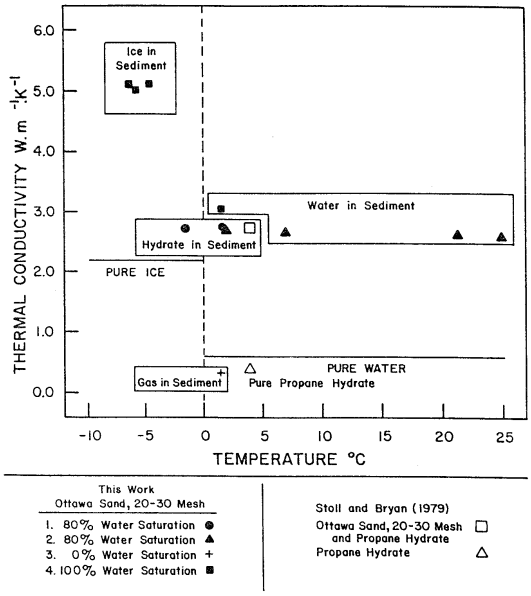

Figure 1.3.: Thermal conductivity of gas, water, ice, and hydrates, both with and without unconsolidated sediment (from *Sloan*, 1998).

chemical composition (inhibitor injection). Most approaches were based on strongly simplified assumptions about the physical processes and parameters involved.

To date several advanced simulation codes are under development. EOSHYDR2 (*Moridis*, 2002) is an extension of the fluid and heat flow numerical simulator TOUGH2 (*Pruess*, 1991), with the capability to account for multiple components and phases, as well as either equilibrium or kinetic decomposition of hydrate. Nevertheless the results of such simulators is still inconsistent and speculative, but the results of the Mallik 2002 program have yielded valuable field and laboratory data which will enable the required calibration and validation of the numerical models. Numerical simulation modelling studies of the Mallik 2002 thermal stimulation test have been performed by *Kurihara et al.* (2005) and *Moridis et al.* (2005).

1.3. Contributions Made in this Work

This work investigates the influence of methane hydrate on the transport of heat in porous rocks. Both the effect on the static temperature field (i.e. thermal conductivity) and temperature changes are analyzed based on temperature logging data collected during the Mallik 2002 program. For acquisition of the temperature data, three wells penetrating a continental gas hydrate occurrence under permafrost (reviewed in Chapter 2) were successfully equipped with permanent fiber-optic distributed temperature sensing cables (Chapter 3).

Formation temperatures and geothermal gradients are determined from the temperature profiles recorded over a period of 21 months after drilling of the wells (Section 3.5.1). New implications for the distribution of permafrost and hydrate occurrences at Mallik

are derived from the transient response of the well temperatures after drilling (Section 3.5). For the first time, the temperature effect of decomposition of gas hydrate was monitored in situ. These results are also published in *Henninges et al.* (2005a).

The in-situ thermal conductivity is estimated using two independent approaches: The effective thermal conductivity of gas hydrate bearing sediments is calculated using different mixing-law models (Chapter 4). The required rock composition is derived from a petrophysical model and the available well-log data. The appropriate mixing-law model is verified by independent calculation of thermal conductivities from geothermal data. Thermal conductivity profiles are calculated from the measured geothermal gradients and an estimate of local heat-flow density based on Fourier's law of heat conduction.

Considering the stability conditions for methane hydrate at Mallik (Chapter 5.3), a numerical model is set up in order to assess the effect of phase transitions within the gas hydrate bearing strata (Chapter 6). The temperature changes resulting from the thermal influences during the drilling of the well at the base of the hydrate occurrences are simulated using a simplified model of conductive heat flow. Both the mobilization of latent heat during the phase transition (enthalpy method) and the effects of hydrate decomposition on the thermal rock properties and the salinity of the pore fluid are considered.

2. The Geology at Mallik in a Regional Context

2.1. Regional geology

The study area is located in the northwestern part of the Canadian arctic, near the border to Alaska. The Mackenzie Delta is bounded by the Beaufort Sea to the north and the topographic rises to the west (Richardson Mountains) and east (Caribou Hills), which are forming the landward boundaries of the delta. The Mallik site is located at the northern edge of Richards Island (Figure 2.1), which is separated from the mainland through the East Channel of the Mackenzie River.

For the understanding of the geology of the Mackenzie Delta - Beaufort Sea region a substantial database from over 250 exploratory wells and many tens of thousands km of reflection seismic data is available from the exploration for hydrocarbons. An overview of the geology of the Canadian Beaufort shelf and the adjacent land areas can be found in *Dixon and Dietrich* (1990). The Upper Cretaceous to Pleistocene stratigraphy has been described by *Dixon et al.* (1992). A comprehensive compilation and interpretation of the available geological, geophysical and geochemical data is contained in *Dixon* (1996).

Within the study area, the Beaufort Sea and adjacent land areas are underlain by thick sedimentary successions of the Beaufort - Mackenzie Basin. The development of the passive continental margin dates back to Lower Cretaceous time (130 Ma - 80 Ma), during which continental breakup and sea-floor spreading had occurred (*Dixon and Dietrich*, 1990). The hereafter deposited Upper Cretaceous to Holocene sediments are reaching thicknesses of over 12,000 m a short distance seaward of the present coastline (*Dixon et al.*, 1992). The Upper Cretaceous to Holocene rocks have been subdivided into eleven major transgressive-regressive sequences (Figure 2.2), which are locally separated by major regional unconformities.

The major structural features in the study area are large-scale northeast- and east-trending normal faults, with mainly down-to-basin throw. A prominent Upper Miocene unconformity marks the end of this tectonic period, and the younger strata are essentially undeformed (*Dixon et al.*, 1992).

The Quaternary cover of the Mackenzie Delta can broadly be grouped into two separate regions: The surficial deposits on Richards Island and the Tuktoyaktuk Peninsula are mainly of Pleistocene (Wisconsinan) age, deposited in fluvial, deltaic and lacustrine environments. There is evidence, that a trough-like basin was formed in the area of the 'modern' delta by glacial erosion during the Wisconsinan glaciation (e.g. *Judge et al.*, 1987). The modern delta itself (see Figure 2.1) would therefore be of Holocene age.

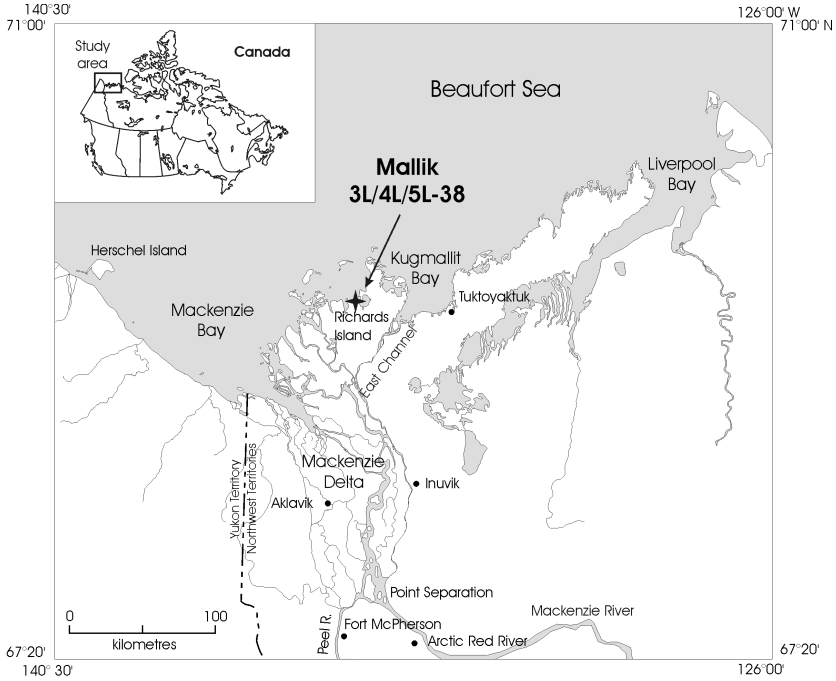

Figure 2.1.: Location map of the Mackenzie Delta - Beaufort Sea area, modified from *Dallimore and Burn* (1997).

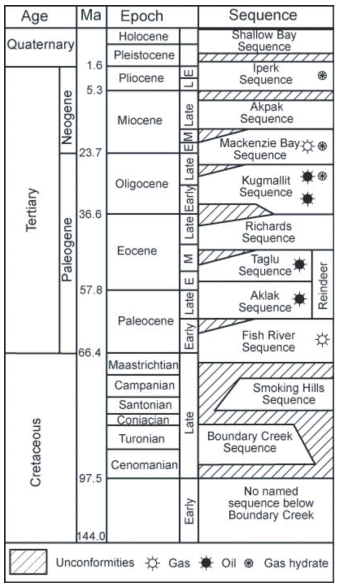

Figure 2.2.: Upper Cretaceous to Holocene sequence stratigraphy of the Mackenzie Delta - Beaufort Sea area (modified from *Dixon et al.*, 1992).

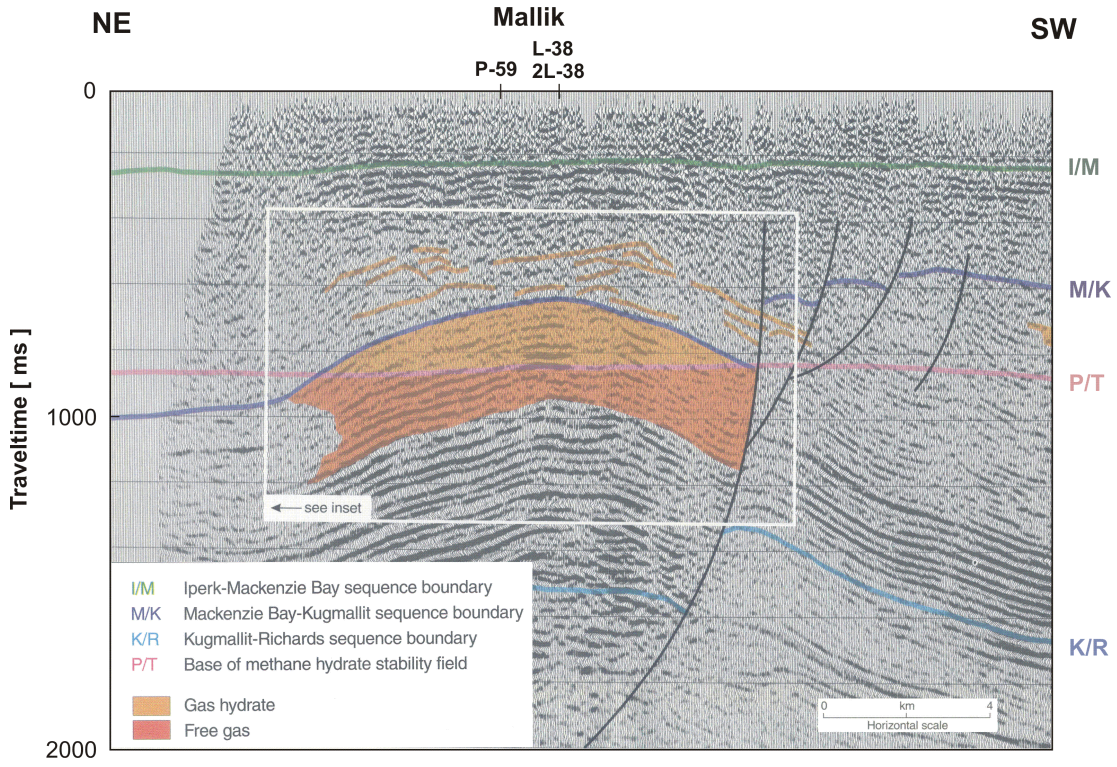

Figure 2.3.: Reflection seismic profile with inferred sequence boundaries, fault traces and gas hydrate occurrences. Inferred free gas occurrence below the gas hydrates was not confirmed by the results of the Mallik 2002 program (Detail of seismic profile 85251, modified from *Collett et al.*, 1999).

2.2. Geology at Mallik

The local structure of the subsurface in the area of the Mallik site has been intensively studied during hydrocarbon exploration. *Collett et al.* (1999) have evaluated the available data in order to delineate the extent of the gas hydrate occurrences on Richards Island. The Mallik site is characterized by anticlinal structure which is bounded by a large-scale normal fault with a down-to-basin throw (Figure 2.3). These structural features are limited to the Richards, Kugmallit and Mackenzie Bay strata, whereas the overlying Iperk Sequence rocks are undeformed. Comparison of several seismic profiles reveals, that the Mallik anticline has a southeastern trend and plunges to the northwest (*Collett et al.*, 1999).

On the basis of the available seismic-reflection records and well-log data from the Mallik L-38 and 2L-38 wells (Figure 2.4), *Dallimore and Collett* (1999) and *Collett et al.* (1999) have identified the Iperk, Mackenzie Bay, and Kugmallit sequences proposed by *Dixon et al.* (1992). Figure 3.7 shows a site map and the location of the wells. The respective depths of the sequence boundaries identified for different well locations are listed in Table 2.1. In order to facilitate the comparison of the different depth values, all depth values were correlated to ground level as a common depth datum. At the

Table 2.1.: Depth of sequence boundaries at Mallik correlated to ground level. mKB: meters below kelly bushing; mGL: meters below ground level; mSL: meters above sea level; I-MB: Iperk - Mackenzie Bay sequence boundary; MB-K: Mackenzie Bay - Kugmallit sequence boundary. References: 1: *Dallimore and Collett* (1999, p. 37); 2: *Dallimore et al.* (1999, p. 14); 3: *Jenner et al.* (1999, p. 66); 4: *Medioli et al.* (2005, in press).

Well name	Reference	Depth datum	KB (mGL)	GL (mSL)	I-MB (mKB)	MB-K (mKB)	I-MB (mGL)	MB-K (mGL)
L-38	1	GL	8.99	0.88	n/a	n/a	350.0	918.0
2L-38	2	KB	7.05	1.26	346.0	n/a	339.0	n/a
2L-38	3	KB	7.05	1.26	n/a	926.5	n/a	919.5
5L-38	4	KB	4.60	1.00	n/a	932.6	n/a	928.0

Mallik site the ground level can be regarded as almost constant at about 1 m above sea level.

During both the Mallik 2L-38 and the Mallik 2002 program core samples were retrieved from the hydrate-bearing strata including the boundary between the Mackenzie Bay and Kugmallit sequences. The lithology generally varied between unconsolidated sands and gravels, to compact sandstones and shales. *Medioli et al.* (2005) identified six informal lithological units within the cored interval of the Mallik 5L-38 well between 885.63 mKB and 1150.79 mKB (Table 2.2). These units can laterally be traced with only minor offsets in depth between the Mallik 3L-38, 4L-38, and 5L-38 wells using the available gamma-ray logs (Figure B.1).

Within the succession of sand- and silt-dominated sedimentary units a number of thin (0.1 m to 1.7 m) dolomite cemented sandstones and low-rank coal beds are occurring. These intervals can clearly be recognized on the available geophysical well logs (e.g. Figure B.4 and Figure B.5). The low-rank coal beds are characterized by low gamma-ray intensities, low densities, high neutron porosities and high resistivities. The dolomite-cemented sandstone beds were identified by high densities, high resistivities, low neutron- and NMR-porosities.

The low-rank coal beds and the dolomite-cemented sandstone beds were used as marker horizons for the correlation between the coring and well-logging data of the Mallik 5L-38 well (Table B.1), which was required for comparisons between these two data sets (e.g. Chapter 4). The observed offsets between the log depths and core depths range between ± 2.5 m and can be regarded as typical values for borehole data of this type.

2.3. Temperature Field and Permafrost

Apart from large-scale heat-flow studies spanning the entire arctic region of the North American continent (e.g. *Langseth et al.*, 1990), a number of regional- and local-scale geothermal studies have been performed in the Mackenzie Delta - Beaufort Sea region in the framework of permafrost and gas hydrate studies. A comprehensive database of

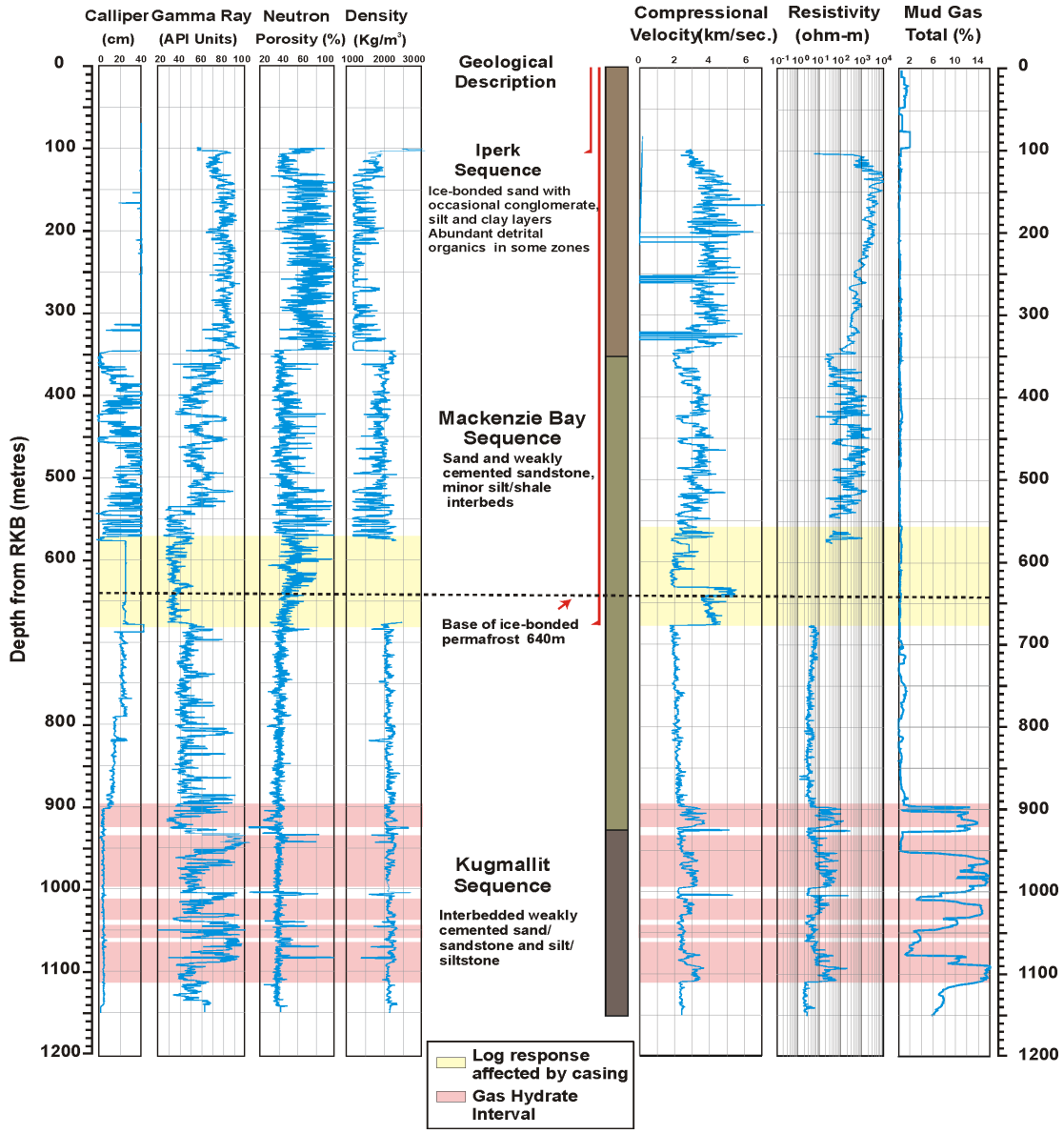

Figure 2.4.: Geophysical well logs of Mallik 2L-38 (from *Dallimore et al.*, 1999).

Table 2.2.: Depths to top of lithological units of cored interval of Mallik 5L-38 (meters below kelly bushing). Lithological units and core depths after *Medioli et al.* (2005). The depth correlation was performed on the basis of the available gamma-ray logs (Figure B.1).

Unit	Description	Core depth 5L-38	Log depth 3L-38	Log depth 5L-38	Log depth 4L-38
1	Sand with silt and pebble interbeds	885.6	885.6	885.6	885.6
2	Silt and low-rank coal	932.6	931.0	930.5	932.2
3	Sand with silt and pebble interbeds	944.4	942.6	942.4	944.3
4	Silt and low-rank coal	1004.7	1001.6	1002.3	1002.5
5	Sand	1087.6	1085.0	1085.2	1087.5
6	Silt with sand and clay interbeds	1142.7	1135.8	1141.3	1135.2

precise ground temperature logs in the permafrost regions of northern Canada, entitled *The Canadian Geothermal Data Collection*, is available (*Taylor et al.*, 1998, and references therein). This collection mostly includes temperature profile data of up to several hundred m depth down to the permafrost base. Studies of the temperature field in the deeper subsurface below the permafrost were based on thermally disturbed bottom-hole temperature (BHT) measurements and drill-stem test (DST) data from deep (i.e. several thousand m) petroleum exploration wells and estimates of thermal conductivity (e.g. *Majorowicz et al.*, 1990). At Mallik, none of the previous drilling projects had included a reliable measurement of the formation temperature after sufficient shut-in time (for a discussion on the measurement or estimation of the formation temperature see Section 3.5 below).

For the delineation of the methane hydrate stability field at Mallik, *Majorowicz and Smith* (1999) performed constructions of temperature profiles based on the assumption of steady-state, conductive heat flow. Heat-flow density was calculated from the linear interpolation of industry BHT and DST temperature data and the estimated average thermal conductivity. Using this method, calculated heat-flow densities for the Mallik region ranged between 39 mW m^{-2} and 55 mW m^{-2}. For the Mallik L-38 well a value of 55±8 mW m^{-2} was calculated.

Apart from the industry borehole temperature data, *Majorowicz and Smith* (1999) used the depth to the base of the ice-bearing permafrost as a constraint to the subsurface temperature field. Because the occurrence of ice-bearing permafrost can also be detected by independent geophysical logging methods, the depth to the base of permafrost is often used within geothermal studies in permafrost environments (e.g. *Majorowicz et al.*, 1990).

The definition of *permafrost* is based exclusively on temperature, and describes any surficial deposit or bedrock, in which a temperature below 0 °C has existed for a time

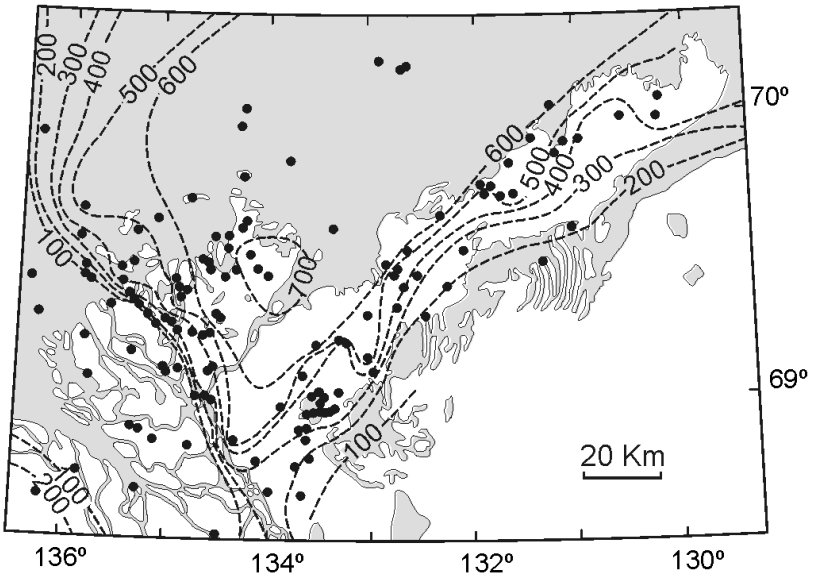

Figure 2.5.: Depth to the base of the ice-bearing permafrost, Mackenzie Delta - Beaufort Sea region (modified from *Judge et al.*, 1987).

greater than two years. It therefore not necessarily includes the presence of ice, as intuitively might be assumed. But a significant change of the physical properties of a porous sediment or rock around freezing temperature only comes along if water is contained and transformed to ice. Therefore the term *ice-bearing permafrost* (IBPF) has been introduced in order to indicate the presence of ice within the respective substrate. By analysis of precision temperature logs *Taylor and Judge* (1981) had observed, that the depth of the base of the IBPF can be about 5 m to 50 m less than to the 0 °C isotherm in the Mackenzie Delta area. The freezing point depression of ice within permafrost is attributed to a combination of effects resulting from pressure, chemistry of the pore water and soil particle effects. For practical purposes it may be assumed, that the base of the IBPF corresponds to the -1 °C isotherm (*Majorowicz and Smith*, 1999).

Different geophysical methods can be applied in order to measure or predict permafrost thickness (e.g. *Taylor and Judge*, 1981). Figure 2.5 shows the depth to the base of the ice-bearing permafrost in the Mackenzie Delta - Beaufort Sea region, which was determined on the basis of thermal and other geophysical (mostly electrical and acoustic) logs from a total of 161 exploratory wells. The permafrost section is reaching a maximum thickness of over 700 m in the area of Richards Island. Towards the southwest into the modern delta the thickness is rapidly decreasing to values below 100 m.

The depths of the ice-bearing permafrost estimated for the different well locations on the Mallik site (Figure 3.7) are listed in Table 2.3. In order to facilitate the comparison of the data, all depth values were correlated to ground level as a common depth datum,

Table 2.3.: Depth of ice-bearing permafrost at Mallik correlated to ground level. mKB: meters below kelly bushing; mGL: meters below ground level; mSL: meters above sea level; IBPF: base of ice-bearing permafrost. References: 1: *Judge et al.* (1987); 2: *Dallimore and Collett* (1999, p. 37); 3: *Dallimore et al.* (1999, p. 14); 4: *Henninges et al.* (2005a, in press).

Well name	Reference	Depth datum	KB (mGL)	GL (mSL)	IBPF (mKB)	IBPF (mGL)	Determination method
L-38	1	GL	8.99	0.88	n/a	613	Electrical resistivity, acoustic velocity
L-38	2	GL	8.99	0.88	n/a	640	Log response (?)
2L-38	3	KB	7.05	1.26	640	633	Electrical resistivity
3L-38	4	KB	4.60	1.00	604	599	Temperature
4L-38	4	KB	4.60	1.00	609	604	Temperature
5L-38	4	KB	4.60	1.00	605	600	Temperature

which at the Mallik site can be regarded as almost constant at about 1.0 m above sea level.

Judge et al. (1987) determined the base of IBPF at the Mallik L-38 well at 613 m below ground level [1]. At the Mallik 2L-38 well, a depth of about 633 m below ground level was estimated from the Laterolog response (*Dallimore et al.*, 1999, p. 11). Within this study, the depth to base of ice-bearing permafrost at the Mallik 3L-38, 4L-38 and 5L-38 wells was determined between 599 m and 604 m below ground level (Table 3.7), using the transient temperature response of a well drilled in permafrost (Section 3.5.3, see also *Henninges et al.*, 2005a). Despite the good overall agreement of the data it should be noted, that temperature data can be regarded as the most reliable information for the determination of the location of the base of the IBPF. The interpretation of other geophysical data might be ambiguous in this context, for instance due to the eventual presence of a melting annulus resulting from the thermal disturbance around a borehole a short time after drilling.

The strong influence of the surface temperature history on the subsurface temperature field is evident from the regional variation of permafrost thickness. The thick permafrost of the eastern Mackenzie Delta and the adjacent Beaufort shelf is attributed to subaerial conditions during the last glaciation period within the Pleistocene (Wisconsinan), whereas the western region was probably insulated from low air temperatures by overlying ice sheets (*Judge et al.*, 1987).

Taylor (1999) performed numerical calculations of the recent temperature field at Mallik based on different assumptions about the paleoenvironmental history of the site. The influence of the distribution of land and surface water bodies on local variations of the temperature field is mostly limited to the permafrost section, but long-term changes were also predicted for the deeper subsurface below.

[1] Depth datum not indicated in original publication, therefore ground level was assumed.

2.4. Gas Hydrate Occurrences

Bily and Dick (1974) documented the first discovery of gas hydrate in the Mackenzie Delta area in the Mallik L-38 and Ivik J-26 wells, drilled by Imperial Oil in 1972. Since then, gas hydrate occurrences have been reported for up to 52 well locations in the Mackenzie Delta - Beaufort Sea region (*Judge and Majorowicz*, 1992), mostly based on evidence derived from characteristic well-log responses attributed to the presence of gas hydrates. Direct evidence of gas hydrates was reported for two locations on Richards Island; Hydrate-bearing drill cores have been retrieved from the permafrost interval of the 92GSCTAGLU borehole (*Dallimore and Collett*, 1995) and from the sub-permafrost section of the Mallik 2L-38 (*Dallimore et al.*, 1999) and 5L-38 (*Dallimore et al.*, 2005, Figure 2.6) wells.

Majorowicz and Osadetz (2001) provided a comprehensive inventory of potential methane hydrate accumulations in Canada. Estimations of this kind are usually relying on the following factors:

- Estimated extent of methane hydrate stability zone.
- Amount of data available from exploration wells drilled in the area of investigation.
- Accuracy of method applied for estimation of gas hydrate saturation from geophysical measurements.

According to the estimates of *Majorowicz and Osadetz* (2001), as much as 0.24 - 8.7×10^{13} m^3 of methane could be stored in hydrate form in the Mackenzie Delta - Beaufort Sea region. The great bandwidth of the given numbers is an indicator of the yet highly speculative nature of such estimates, because they are relying on the above conditions and assumptions.

The subsurface pressure and temperature field and the composition of the pore fluid and gas phase are the main controlling factors for the stability of methane hydrate (for a detailed discussion see Chapter 5.3). Estimates of the extent of the methane hydrate stability zone strongly rely on the availability of data or the validity of assumptions about the above parameters.

In boreholes, gas hydrate occurrences were traditionally deduced from a strong increase in methane content of the drilling mud, combined with high electrical resistivity and increased sonic velocity of the respective intervals (e.g. *Bily and Dick*, 1974; *Collett*, 1993; *Dallimore and Collett*, 1999). Nevertheless, quantitative estimates of the in-situ hydrate saturation using the above methods are difficult, primarily because the log response is ambiguous and only a very limited amount of suitable sample material, which is required in order to calibrate potential geophysical methods of detection, is available (*Spangenberg*, 2001). *Kleinberg et al.* (2003) have proposed proton nuclear magnetic resonance (NMR), in conjunction with another measurement of porosity, as an appropriate method in order to quantitatively determine gas hydrate saturation from geophysical well logs (see also Chapter 4).

On the basis of reflection seismic and well-log data *Collett et al.* (1999) have mapped four significant gas hydrate and associated free-gas accumulations on Richards Island

in the vicinity of the Mallik site. According to their results the occurrence of gas hydrate is restricted to the crests of large anticlinal features. At Mallik, gas hydrate occurrences are inferred and known to occur inside the Kugmallit and Mackenzie Bay strata along the crest of the Mallik anticline (Figure 2.3). A series of high- and low-amplitude reflectors on the seismic profile was interpreted as an interbedded succession of gas-hydrate-bearing sandstones and non-gas-hydrate-bearing shale layers. Amplitude phase reversals have been reported to occur locally at the predicted base of the gas hydrate stability field within the Mallik anticline (*Collett et al.*, 1999). A pronounced and extensive seismic reflection, indicating the base of the hydrate occurrences like in many marine environments (bottom simulating reflector, BSR), has not been observed at Mallik, which was attributed to the complex geological structure of the subsurface in the Mallik area.

A total of 99 m of hydrate-bearing sand were interpreted to be penetrated by the Mallik L-38 well within the interval between 820 m and 1103 m (*Bily and Dick*, 1974). In a re-examination of the log-data from the Mallik L-38 well, *Dallimore and Collett* (1999) identified 10 separate hydrate-bearing intervals with a total thickness of 111.4 m. The results of the Mallik 2L-38 data generally confirmed the assumed gas hydrate occurrences derived from the Mallik L-38 well logs (*Dallimore et al.*, 1999). The uppermost gas hydrate zone from the Mallik L-38 well was not identified in Mallik 2L-38, where the onset of the hydrate-bearing interval is reported to occur about 79 m further below (*Collett et al.*, 1999, see Table 2.4). Results of the well-log analysis for the Mallik 5L-38 well deploying the Density-Magnetic Resonance Method (*Kleinberg et al.*, 2005, see Section 4.2.2) are indicating a similar extent of the zone of hydrate occurrences as in the Mallik 2L-38 well. The depths to the top and bottom of the gas hydrate occurrences derived from different well logs from the Mallik site are listed In Table 2.4. In order to facilitate the comparison of the data, all depth values were correlated to ground level as a common depth datum, which at the Mallik site can be regarded as almost constant (1.0±0.2 m above sea level).

Within this study, the base of the gas hydrate occurrences was determined from temperature logs of the Mallik 3L-38 and 4L-38 wells in analogy to the transient temperature response of a well at the permafrost base (Section 3.5.3, *Henninges et al.*, 2005a). All determined depths of the bottom of the gas hydrate bearing strata are showing a close agreement.

According to estimates of *Majorowicz and Smith* (1999), the methane hydrate stability zone at Mallik lies between 220±10 m and 1100±100 m below ground level. The bottom of the observed hydrate occurrences therefore correlates well with the predicted base of the methane hydrate stability zone. Although thermodynamically stable up to a depth of about 220 m, no gas hydrate was observed at a depth above 810 m below ground level.

Table 2.4.: Depth of gas hydrate occurrences at Mallik correlated to ground level. mKB: meters below kelly bushing; mGL: meters below ground level; mSL: meters above sea level; GHZ-T: top of gas hydrate occurrences; GHZ-B: bottom of gas hydrate occurrences. References: 1: *Dallimore and Collett* (1999, p. 37); 2: *Collett et al.* (1999, p. 366); 3: *Henninges et al.* (2005a, in press); 4: *Kleinberg et al.* (2005, in press).

Well name	Reference	Depth datum	KB (mGL)	GL (mSL)	GHZ-T (mKB)	GHZ-B (mKB)	GHZ-T (mGL)	GHZ-B (mGL)
L-38	1	GL	8.99	0.88	n/a	n/a	810.10	1102.30
2L-38	2	GL	7.05	1.26	n/a	n/a	888.80	1101.90
3L-38	3	KB	4.60	1.00	n/a	1108.00	n/a	1103.40
4L-38	3	KB	4.60	1.00	n/a	1109.00	n/a	1104.40
5L-38	4	KB	4.60	1.00	891.00	1107.00	886.40	1102.40

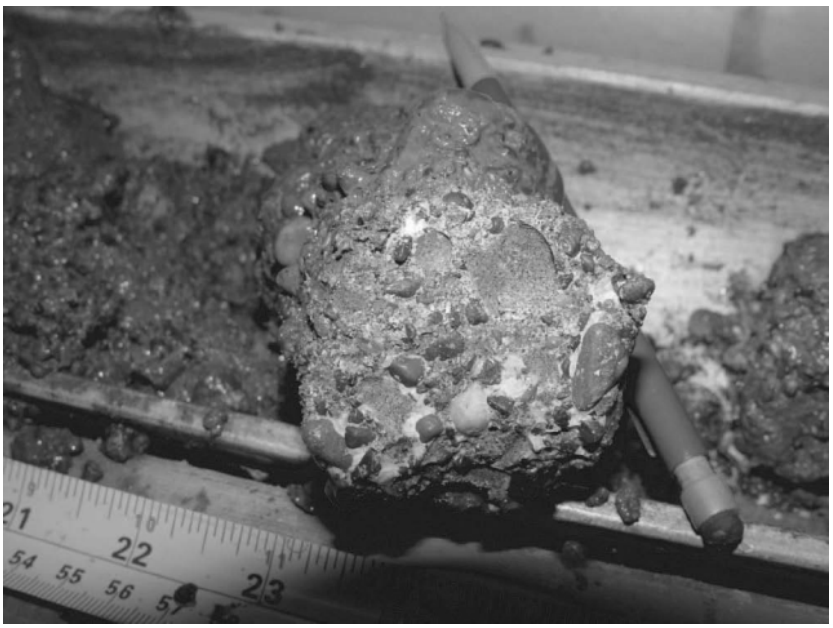

Figure 2.6.: Photo of core sample with visible gas hydrate forming matrix of 2 m thick conglomerate at approximately 915 m depth, Mallik 5L-38 well (from *Dallimore et al.*, 2005).

3. Distributed Temperature Measurements at Mallik

3.1. The Method of Distributed Temperature Sensing

Within recent years, fiber-optic distributed temperature sensing (DTS) has been introduced as a new technology for the measurement of temperature in boreholes (e.g. *Hurtig et al.*, 1993; *Förster et al.*, 1997). *Wisian et al.* (1998) compare DTS to other conventional temperature logging methods. Through the deployment of DTS technology, quasi-continuous temperature profiles can be measured with high temporal resolution. In comparison to other conventional temperature logging equipment, generally a lower accuracy of the temperature data in the order of a few tenths °C up to several °C has to be accepted.

3.1.1. Measurement Principle

A description of the principles of distributed fiber-optic sensing and further references can be found in *Hartog and Gamble* (1991) and *Grattan and Meggitt* (1995). DTS is based on the method of optical time-domain reflectometry (OTDR, Figure 3.1). Short laser pulses are injected into an optical fiber and the backscattered and reflected light is measured as a function of time. Thermally driven molecular vibrations are resulting in a difference of the wavelength of parts of the backscattered light to the wavelength of the incident light (Raman scattering, Figure 3.2). The shorter-wavelength Raman band (anti-Stokes band) is caused by transfer of energy from phonons in the optical fiber to photons of the backscattered light. The intensity of the anti-Stokes band is temperature dependent (Figure 3.3) and the spectrum of the backscattered light can be analyzed to determine the temperature of incremental sections along the optical fiber. The position of a measurement along the optical fiber is determined from the travel time of the signal and the known speed of the light propagating through the optical fiber.

3.1.2. Measurement Configurations

The used DTS system can be operated in two different configurations, which are referred to as single-ended and double-ended processing modes. In single-ended mode, measurements are performed from one end of a single optical fiber line (Figure 3.4 a). For the calculation of temperature the optical loss along the fiber, which is to be determined individually for a specific fiber, has to be compensated (differential loss correction, see Section 3.2). In double-ended mode, measurements are performed from both ends of the optical fiber line (Figure 3.4 b). This requires, that the optical fiber line is installed in a loop configuration with both ends connected to the DTS instrument. Advantages

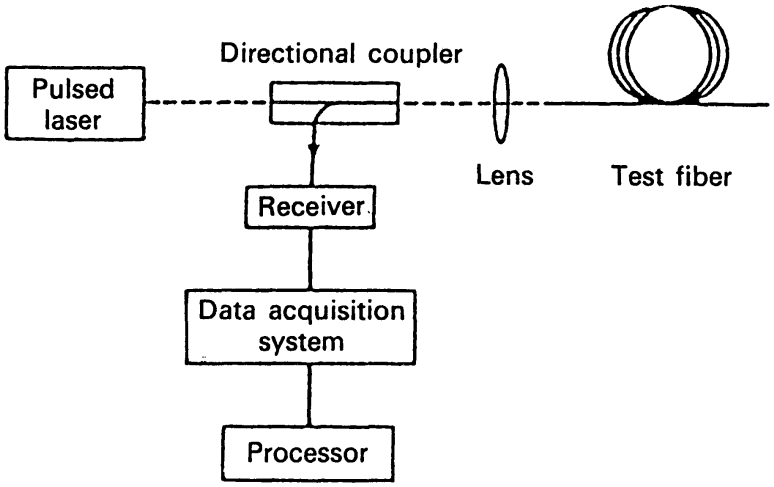

Figure 3.1.: Functional diagram of an optical time-domain reflectometer (from *Hartog*, 1995).

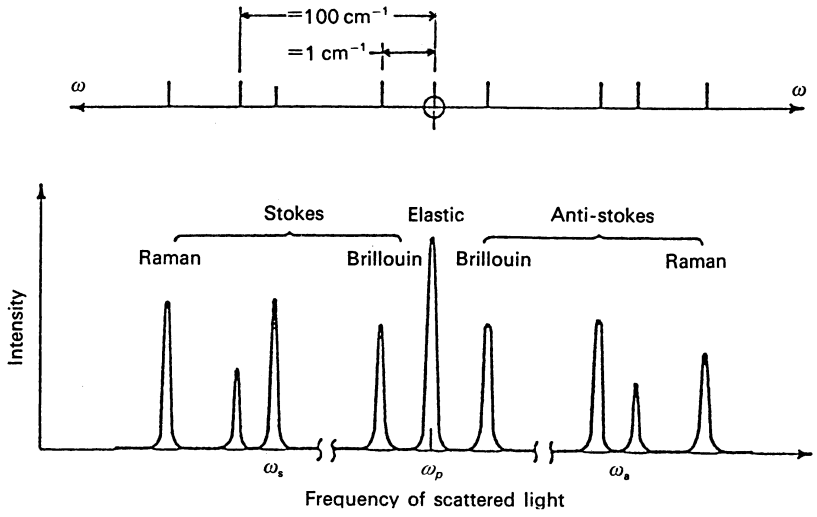

Figure 3.2.: Schematic spectrum of scattered light. ω_p = frequency of incident light, ω_s = frequency of Stokes Raman scattering, ω_a = frequency of anti-Stokes Raman scattering (from *Hayes and Loudon*, 1978, p. 25, in *Rogers*, 1995).

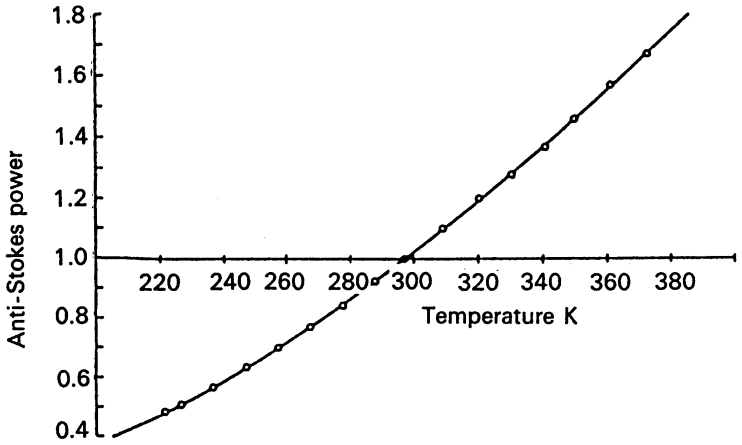

Figure 3.3.: Raman anti-Stokes back-scatter signal measured as a function of temperature. Results have been normalized to unity at 24 °C (from *Hartog*, 1995).

of the double-ended mode are, that no compensation for the optical loss is required and that the signal noise is lower than within single-ended mode. Both single- and double-ended processing modes were used for the DTS temperature surveys at Mallik.

3.1.3. Examples of Application

For temporary DTS installations, the sensor cable is lowered into the borehole, and after data acquisition the sensor cable is again retrieved (e.g. *Hurtig et al.*, 1993; *Förster et al.*, 1997; *Büttner and Huenges*, 2003). In contrast to conventional wireline logging, where the logging tool is moved along the section of the borehole to be scanned, the DTS cable remains in place during the measurement of the temperature profiles. Installations of this type have been performed up to a maximum depth of 4265 m and a temperature of 143 °C in a geothermal well in Germany (*Henninges et al.*, 2005b).

For long-term monitoring or in cases when full access to the interior of the borehole is needed, the sensor cables are installed in the annulus behind the borehole casing. This approach was used for temperature monitoring in the three wells of the Mallik 2002 program (Section 3.3). Permanent installations of this type are of special interest in the exploration and production sector of the hydrocarbon industry for the monitoring of flow conditions in oil and gas wells. The first permanent installations were performed up to several hundred meters depth in 1993 (*Grosswig et al.*, 2001). Lately intricate installation procedures with hydraulic injection of the optic fiber into small diameter control lines are under development. First installations have been reported over distances of up to 4300 m (TVD = 1500 m) in a horizontal production well with a maximum temperature of up to about 80 °C (*Laurence and Brown*, 2000).

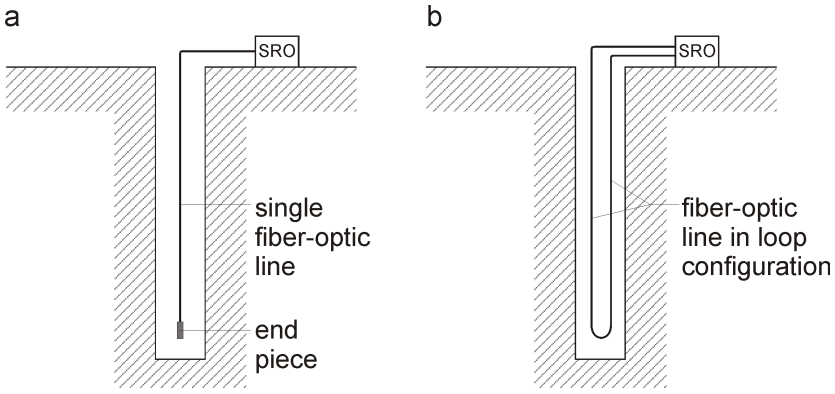

Figure 3.4.: Schematic diagram of single-ended and double-ended processing mode DTS configurations.

3.2. Calibration and Accuracy of the DTS 800 M10

The DTS instrument (opto-electronic unit manufactured by Sensa, UK, model DTS 800 M10) deployed in this study enables the measurement of temperature profiles up to a length of about 10 km. Up to four sensor cables can be connected to the DTS instrument, which can be scanned in sequential order. The spatial resolution is equal to about 1 m, which is determined by the 10 ns pulse width of the laser source. Through a method referred to as *interleaving* the sample spacing can be reduced up to about 0.25 m.

The measurement accuracy (difference between measured and true absolute temperature, systematic error) depends on the calibration and stability of the system. Individual calibrations for the DTS instrument and each fiber-optic sensor cable were carried out. During the calibration procedure, approximately 20 m of the sensor cable were exposed to a steady temperature inside a water bath with cyclic changes of the water bath temperature between -10 °C and +40 °C. The calibration parameters were iteratively adjusted until the deviation of the measured and actual temperature differences remained below a threshold value of 0.5 % (Figure 3.5).

Under controlled conditions within the laboratory, the measured temperatures showed an accuracy of ±0.3 °C after calibration. This accuracy was also achieved during the field experiment, which was verified by independent downhole temperature measurements with an electronic memory tool deployed in the Mallik 3L-38 and 4L-38 wells (Table 3.1, Figure A.4).

The temperature resolution (repeatability of measurement, random error) depends on a number of different factors, including the number of averages for a single measurement (i.e. integration time, length of time interval over which measurement is averaged), the signal processing mode, the fiber length, as well as the distance relative to the beginning of the fiber. While the fiber length and the position of a particular measurement interval are invariable features characteristic to an individual DTS installation, the number of averages can be influenced through choice of spatial resolution and integration time during the measurement as well as subsequent stacking of the measurement data.

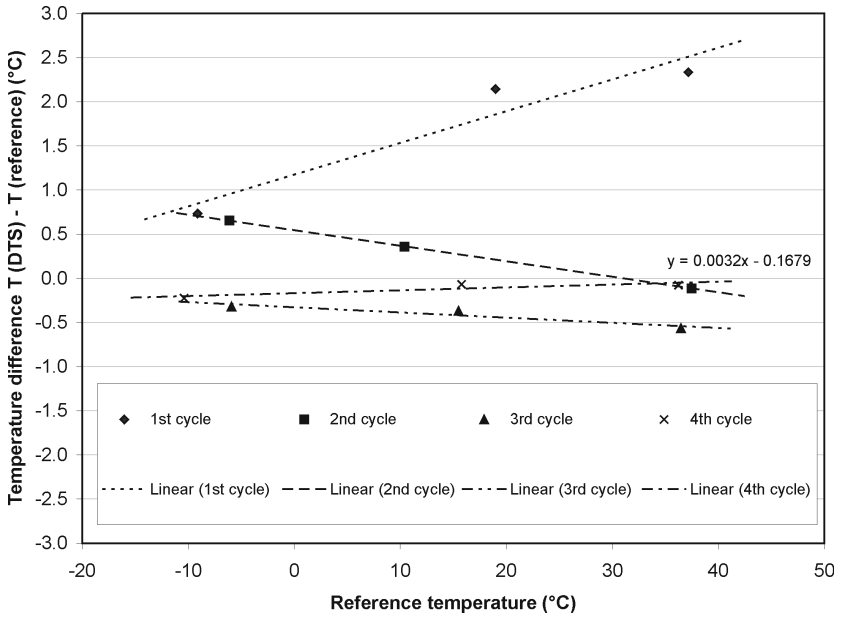

Figure 3.5.: Example of DTS calibration measurement results, Mallik 3L-38 sensor cable (M03, Loop 2). T(DTS): DTS temperature averaged over 20 m interval in water bath; T(reference): water bath temperature measured with a precision platinum resistance thermometer. Calibration parameters were adjusted after each measurement cycle with measurements at three different temperature levels.

Table 3.1.: Comparison of DTS and electronic memory tool temperatures. T_{DTS} = DTS temperature, T_{probe} = electronic memory tool temperature, dT = temperature difference ($T_{probe} - T_{DTS}$).

Well name	Date and time	Depth (mKB)	T_{DTS} (°C)	T_{probe} (°C)	dT (°C)
Mallik 3L-38	Feb. 18, 2002, 16:00	49.0	-5.3	-5.0	-0.3
Mallik 3L-38	Feb. 18, 2002, 18:00	1152.9	13.7	13.6	0.1
Mallik 4L-38	Mar. 09, 2002, 18:30	1135.3	12.6	13.0	-0.4

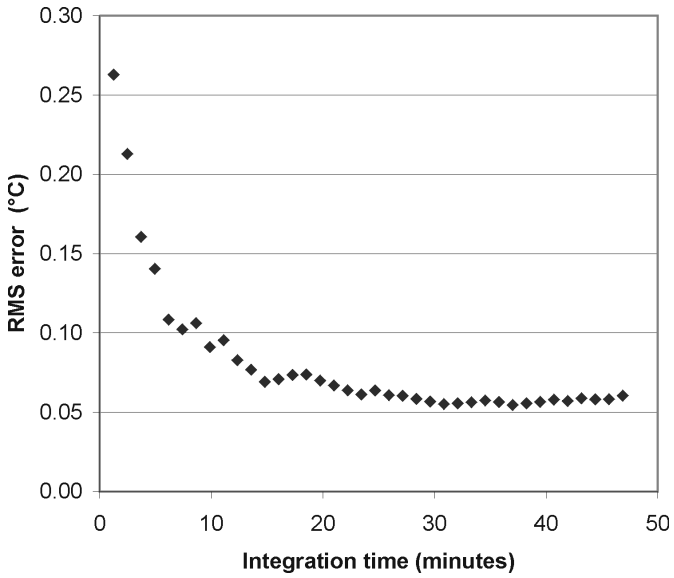

Figure 3.6.: DTS temperature resolution as a function of integration time. Measurement configuration: double-ended processing, data point spacing: 1 m (interleave = 1), fiber length: 2908 m.

In order to minimize the optical attenuation, optical connector pairs with low signal attenuation (about -0.3 dB to -0.6 dB) were chosen and splices for the connection of optical fibers were carefully prepared.

The temperature resolution of the measured DTS temperature data is proportional to the square root of integration time (Figure 3.6). For a 3000 m cable the temperature resolution is 0.06 °C for an integration time of 30 minutes and 1 m spacing of data points (interleave = 1). For measurements with higher spatial resolution, the integration time required to achieve a comparable temperature resolution is multiplied by the number of interleaves.

Prior to the field experiment, individual calibrations of the deployed sensor cables were performed in a temperature controlled chamber at the GFZ Potsdam (Figure A.1). DTS temperature measurements in double-ended processing mode could hereafter be performed at Mallik with the established calibration parameters.

The differential loss correction factor required for DTS measurements in single-ended mode (Section 3.1.2) was determined after installation of the sensor cables through comparison of measured DTS temperatures at equivalent depths of:

- a partially returned sensor cable in a single well (Mallik 4L-38)
- the other sensor cables installed in adjacent wells (Mallik 5L-38)

The long-term temperature monitoring performed at Mallik (Section 3.3) required that repeated calibrations of the DTS system were carried out. After installation of the sensor cables, the calibrations were performed using 20 m reference sections from the original sensor cables and a commercial 12 liter water bath (temperature stability

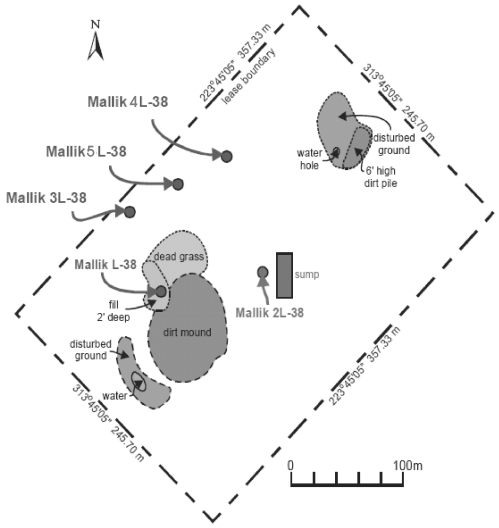

Figure 3.7.: Map of the Mallik site and well locations (modified from *Dallimore et al.*, 2002).

0.02 °C). The stability of the measurements using this procedure was similar to the results of the calibration in the temperature controlled chamber, and resulted in a significant simplification and acceleration of the calibration procedure. The calibration of the reference sections was verified by on-site measurements for the Mallik 4L-38 sensor cable during the September 2003 field trip using the simplified calibration set-up described above.

3.3. Temperature Logging at Mallik

Within the framework of the Mallik 2002 Program, three 1200 m deep wells, spaced at 40 m (Figure 3.7), were equipped with permanent fiber-optic sensor cables (Figure 3.8). In the two lateral observation wells, the sensor cables were installed to a depth of 1158 m in order to determine the formation temperatures. In the central Mallik 5L-38 temperatures were measured to about 940 m depth, and on-line temperature monitoring during a thermal stimulation experiment was performed (*Hancock et al.*, 2005a).

3.3.1. Installation of DTS Sensor Cables

A special feature of the experimental design is the permanent installation of the sensor cables behind the borehole casing. After completion of the well, the sensor cables are located in the cement annulus between casing and borehole wall (Figure 3.8). The fiber-optic cables were attached to the outer side of the casing at every connector, within intervals of approximately 12 m, using custom-built cable clamps (Figure 3.9 and Figure A.3).

The statistics of the DTS installations are listed in Table 3.2. Figures 3.14, 3.15, and 3.16 contain schematic diagrams of the well completion. In order to operate the DTS

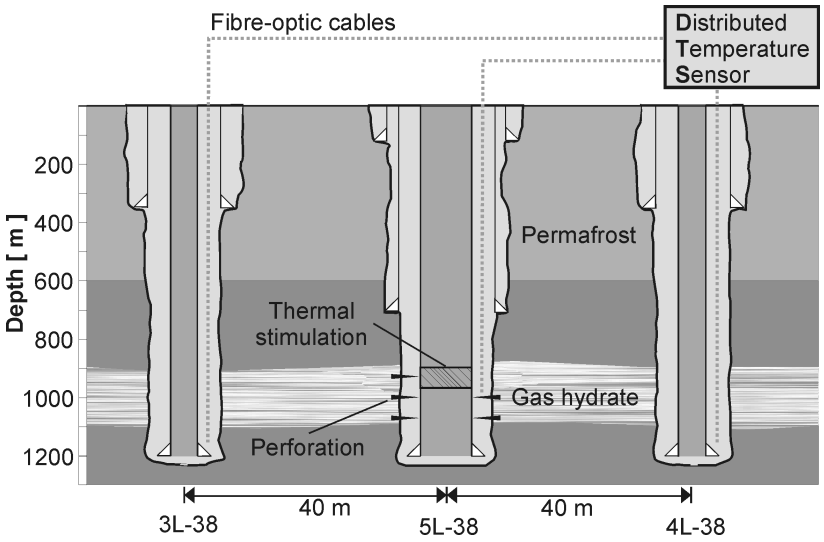

Figure 3.8.: Schematic cross section of the field experiment. After completion of the well the fiber-optic Distributed Temperature Sensing cable is embedded in the cement annulus between the casing and the borehole wall (modified from *Henninges et al.*, 2003).

Table 3.2.: Well completion and DTS installation statistics at Mallik.

	3L-38	4L-38	5L-38
Borehole depth (m KB)	1188	1188	1166
Borehole diameter (in/mm)	7-7/8 / 200.0	7-7/8 / 200.0	8-3/4 / 222.3
Casing depth (m KB)	1179	1184	1165
Casing diameter (in/mm)	5-1/2 / 139.7	5-1/2 / 139.7	7 / 177.8
Max. depth DTS (m KB)	1157.84	1158.32	938.61
DTS processing mode	double ended	single ended	single ended

instrument in double-ended mode, the sensor cables in all wells were installed in a closed-loop configuration with a turn-around at the bottom. The measurements in the Mallik 4L-38 and 5L-38 wells were performed in single-ended mode due to interruptions of the loop configuration by fiber breaks. Further details about the installation procedure can be found in *Henninges et al.* (2005a).

3.3.2. Temperature Logging Schedule

The DTS logging was started one to two days after completion of the respective well (Table 3.3), and continuous monitoring of the well temperatures was performed over a period of up to 61 days. A total of 18935 temperature profiles comprised of 1.33×10^8 single temperature measurements was collected.

Government regulations for the abandonment procedure required that the wells be plugged and the casing cut below ground level. In order to enable future temperature

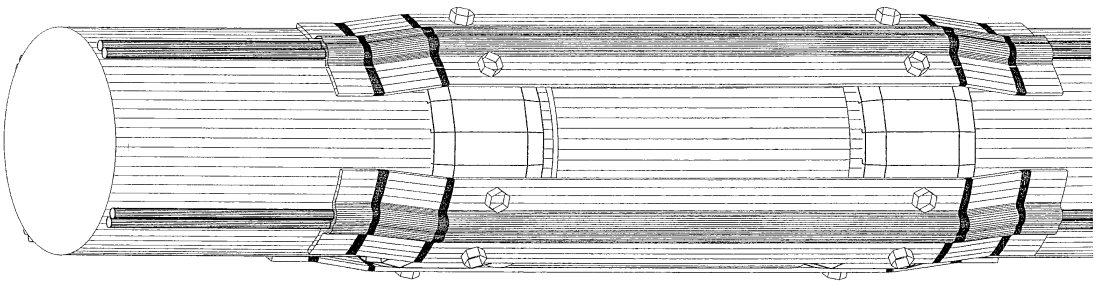

Figure 3.9.: Cable clamp used for the permanent installation of the DTS cables behind the borehole casing.

Table 3.3.: Summary of drilling operations and DTS logging schedule at Mallik.

	3L-38	4L-38	5L-38
Begin drilling	Dec. 25, 2001	Jan. 11, 2002	Jan. 25, 2002
End drilling	Jan. 6, 2002	Jan. 21, 2002	Feb. 22, 2002
End cementation	Jan. 7, 2002	Jan. 22, 2002	Feb. 23, 2002
Start DTS-logging	Jan. 10, 2002	Jan. 25, 2002	Feb. 24, 2002
End DTS-logging	Mar. 12, 2002	Mar. 12, 2002	Mar. 12, 2002
Oct. 2002 DTS survey	Oct. 6-7, 2002	Oct. 6-7, 2002	-
Sept. 2003 DTS survey	Sept. 19-21, 2003	Sept. 19-21, 2003	Sept. 19-21, 2003
Number of profiles	9231	5150	4554
Data points (d_z=0.25 m)	10514	7387	4386
Measurements (total)	7.5×10^7	3.8×10^7	2.0×10^7

measurements, the DTS cables were secured and left accessible during the abandonment of the wells. The surface ends of the sensor cables were stored in custom-designed steel boxes on site (Figure A.5). Two subsequent DTS surveys were carried out for long-term temperature monitoring in October 2002 and September 2003 with a temporary set-up of the DTS equipment (Figure A.6).

3.4. Post-processing of DTS Temperature Data

3.4.1. Depth Correlation

The position of a measured data point along the fiber-optic cable can be determined with high accuracy using DTS technology through measurement of the signal travel time and the known velocity of the light signal propagating through the optic fiber. Nevertheless for well logging practice it is important to correlate the positions of the DTS data points to the borehole depth and a common depth datum.

The length of the installed sensor cable determined from the DTS measurements exceeds the actual length of the casing string by about 7 m to 8 m. This was interpreted as a result of the addition of small excess cable lengths between the cable clamps, which

were used to attach the cable to the borehole casing (Section 3.3.1). It was assumed that this over-length of the sensor cable, which corresponds to 0.8 % of the length of the equipped casing string, is evenly distributed along the depth of the borehole; the measured depth values were corrected accordingly by adjusting the distance of the DTS data points D_{corr} (Eqn. 3.2).

In order to generate temperature profiles which can be compared to the other available borehole data, the raw DTS temperature data was correlated to the elevation of the rotary kelly bushing (KB) on the drill floor [1] as a common depth datum. The depth values were calculated with reference to the known positions of the uppermost connector at the wellhead (H_{top}) and the lowest connector to which the DTS cable is attached (H_{bot}) using the following formulas:

$$z_{DTS}(i) = H_{ref} + (i \cdot D_{corr}) \qquad (i = 0, n-1) \tag{3.1}$$

and

$$D_{corr} = \frac{H_{bot} - H_{top}}{n-1} \tag{3.2}$$

where

z_{DTS} :	Depth of DTS data point (m, relative to common depth datum)
i :	Index number of DTS data point (-)
n :	Total number of DTS data points (-)
H_{ref} :	Elevation of uppermost DTS data point, relative to common depth datum (m)
H_{bot} :	Depth of lowermost DTS data point (m)
H_{top} :	Depth of uppermost DTS data point (m)
D_{corr} :	Corrected distance of DTS data points (m)

The position of the uppermost connector along the measured temperature trace were identified by placing a temperature signal at the corresponding point of the sensor cable or measurement of the length of the sensor cable between the DTS instrument and the wellhead. The depths of the casing connectors extracted from the borehole casing tallies are listed in Table 3.4. In order to enable the best possible fit to the other logging data, the depths of the casing connectors were also picked from the casing-collar-locator logs (CCL). In the Mallik 5L-38 well the distinct temperature signal of the perforating gun was used for the depth correlation (see *Hancock et al.*, 2005a), because the position of the end of the sensor cable was not exactly known due to a fiber break.

3.4.2. Averaging and Filtering of Temperature Data

To increase the temperature resolution, the measured temperatures can be averaged over time (Section 3.2). Depending on the dynamics of the change of temperatures over time and the purpose of evaluation, a reasonable compromise on data quality (temperature resolution) and temporal resolution has to be made. After completion of the measurements the original temperature data recorded with 0.25 m resolution

[1] kelly bushing = 4.6 m above ground level, ground level = 1.0 m above sea level

Table 3.4.: Reference depths for correlation of DTS data in meters below kelly bushing (mKB). * depth correlated to middle of perforating interval at 913,5 mKB.

Depth datum	3L-38	4L-38	5L-38
H_{top} (casing tally)	3.80	3.80	4.39
H_{top} (CCL-log)	3.83	4.45	4.57
H_{bot} (casing tally)	1157.84	1158.32	-*
H_{bot} (CCL-log)	1156.86	1156.84	-*

(interleave = 4) was averaged over approximately two hour data acquisition intervals. According to the determined relationship between integration time and temperature resolution (Figure 3.6), the 2-hour averaging is resulting in a temperature resolution of about 0.06 K. Because up to three sensor cables were scanned successively from the DTS instrument at a time, the two hour data acquisition intervals correspond to 2 - 6 hour intervals in practice.

The frequency spectrum of the DTS data recorded with 0.25 m distance of data points (interleave = 4) clearly displays a coherent noise for multiples of 0.125 Hz, which corresponds to a wavelength of 8 data points or 2 m (Figure 3.10). The existence of coherent noise with a certain frequency spectrum is a well-known effect characteristic to the Sensa (formerly York) DTS instruments, which has also previously been observed by other authors (e.g. *Hurtig et al.*, 1993).

In order to eliminate the coherent noise, the data was transformed into the frequency domain using the Fast Fourier Transformation (FFT). The intensity peaks with multiples of 0.125 Hz were eliminated from the frequency spectrum. Subsequently the data was again transformed backward. The resulting FFT-filtered temperature profile data was additionally smoothed using a 3-point running average filter in order to reduce the remaining random noise prior to evaluation (Figure 3.11).

3.4.3. Experimental Temperature Resolution

The experimental temperature resolution of the borehole data was estimated from the difference of two successively recorded temperature profiles . For this purpose, two different temperature profiles with 2-hr integration time were extracted from the October 2002 DTS survey data (T_a, T_b). During the October 2002 temperature measurements no detectable change of the borehole temperatures should have occurred, and the difference of the measured temperatures ($\Delta T = T_a - T_b$) is only resulting from the random noise of the DTS data. The calculated temperature differences show a normal distribution with an average value of about zero (Figure 3.12). The standard error of the temperature differences ($\sigma_{\Delta T}$) is therefore equal to the standard deviation, and the standard error of the temperature data (σ_T) can be calculated from the law of error propagation:

$$\sigma^2_{\Delta T} = \sigma^2_{T_a} + \sigma^2_{T_b} \tag{3.3}$$

where

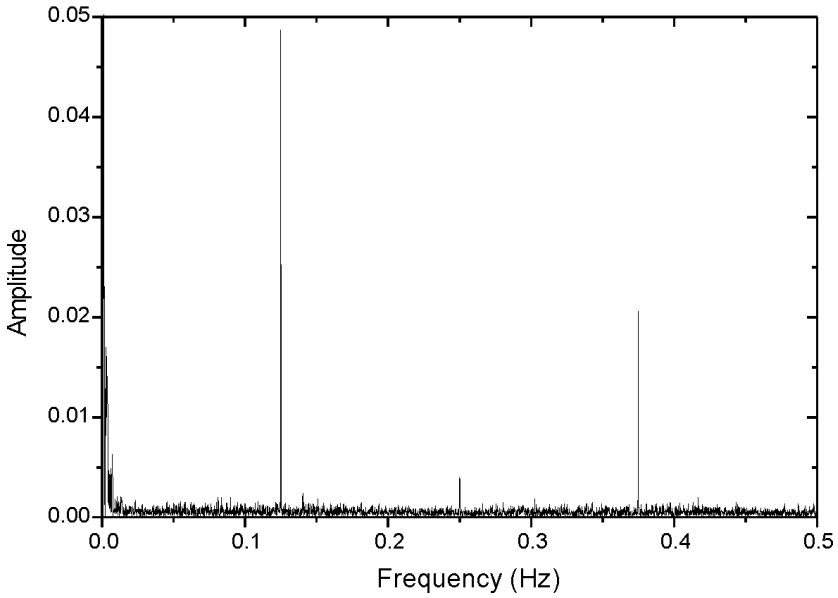

Figure 3.10.: Frequency spectrum of measured DTS temperature data.

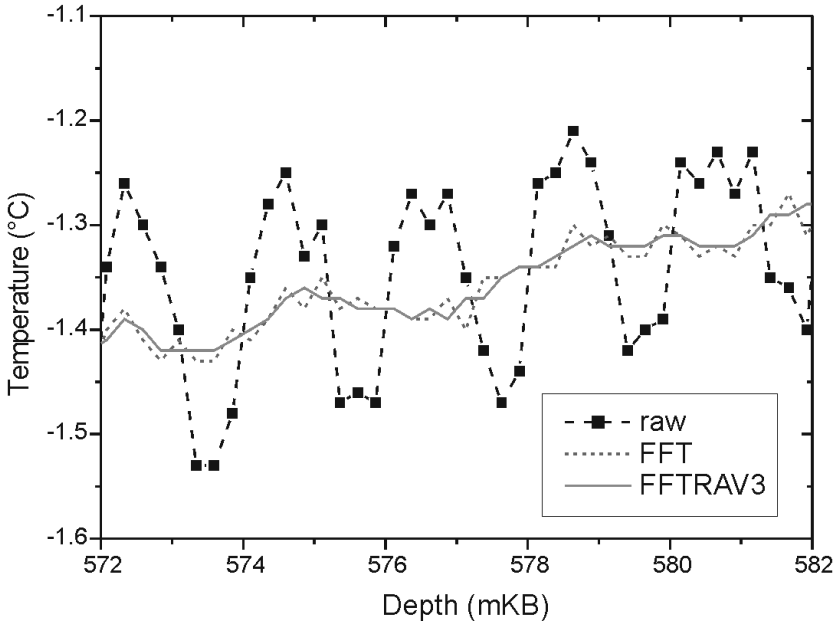

Figure 3.11.: Comparison of raw and filtered DTS temperature data. raw: DTS temperature profile, 2 hr integration time; FFT: FFT-filtered temperature profile with multiples of 0.125 Hz eliminated; FFTRAV3: FFT-filtered temperature profile smoothed with 3-point running average filter.

$$\sigma_{T_a} = \sigma_{T_b} = \sigma_T \tag{3.4}$$

and

$$\sigma_T = \frac{\sigma_{\Delta T}}{\sqrt{2}} \tag{3.5}$$

The estimated temperature resolution (standard error, σ_T) calculated from Equation 3.5 is equal to $3.09 \cdot 10^{-2}$ K and $3.92 \cdot 10^{-2}$ K for of the 2-hour average DTS temperature data of the Mallik 3L-38 and 4L-38 wells respectively (interleave = 4). As a result of the double-ended processing mode, the resolution of the 3L-38 data is generally higher than for the 4L-38 well (Section 3.1.2). The data of the Mallik 5L-38 well was acquired using single-ended processing mode, and the temperature resolution is similar to the 4L-38 well. Nevertheless, because of the applied method of calculation described above, the estimated temperature resolution of the raw DTS data does not contain the influence of the coherent noise. Only the influence of random noise is accounted for, and the estimated values are therefore below the values determined from the laboratory data (Section 3.2), which additionally include the effect of the coherent noise. The temperature resolution determined from laboratory measurements for an equivalent integration time is about 0.06 K (Figure 3.6). The estimated temperature resolution of the FFT-filtered DTS data smoothed with a 3-point running average filter is equal to $1.70 \cdot 10^{-2}$ K and $2.60 \cdot 10^{-2}$ K for the Mallik 3L-38 and 4L-38 wells respectively.

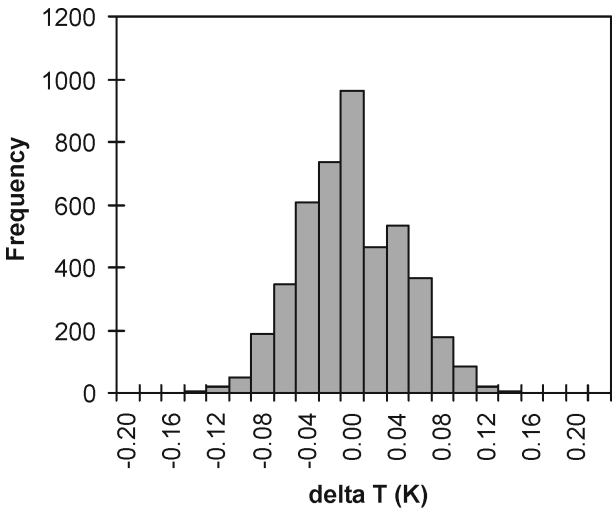

Figure 3.12.: Distribution of temperature differences of successive DTS temperature profiles, Mallik 3L-38 well, October 2002 DTS survey. DTS data recorded with 0.25 m resolution (interleave = 4) and averaged over 2-hour data acquisition interval.

3.5. Geothermal Conditions and Influences by Drilling

3.5.1. Formation Temperatures and Drilling-Induced Disturbances

Excerpts from the recorded temperature data are displayed in Figures 3.14, 3.15 and 3.16 as temperature profiles for successive points in time after the cementing of the wells (shut-in time t_s). For the 3L- and 4L-38 observation wells, cased-hole gamma-ray logs are displayed, which were recorded by the cement-bond-tool (CBT). The gamma-ray logs for the 5L-well were recorded during the open-hole logging program of the permafrost and sub-permafrost sections.

As a result of the thermal disturbance due to the drilling process, a continuous process of equilibration of the borehole temperature to the temperature of the surrounding formation can be observed during the 21-month logging period between January 2002 and September 2003 (Figs. 3.14, 3.15, 3.16). The determination of the formation temperature through temperature measurements in boreholes is generally hampered by the disturbance of the temperature field, which is caused by the drilling process. It is therefore necessary to distinguish between the *borehole temperature* which is actually measured and the undisturbed *formation temperature* which is usually required for geothermal studies. Within this study, the formation temperature is primarily used to derive information about the thermal properties of the formation (Chapter 4) and to determine the stability conditions for methane hydrate at Mallik (Chapter 5.3).

The influence of the drilling process on the borehole temperature has long been recognized, and there is an extensive amount of literature devoted to this subject. Most methods are based on a formulation introduced by *Bullard* (1947), who simplified the problem by using analytical solutions for the conduction of heat around a constant line source. A comprehensive discussion of formulations of this kind can be found in *Lachenbruch and Brewer* (1959), who additionally treated the effect of melting of permafrost. For the evaluation of the temperature data from the Mallik 2002 wells special attention has to be given to latent heat effects resulting from the melting of permafrost and the decomposition of methane hydrate.

Horner-plot analysis of measured temperature changes with time

The variation of temperature over time exhibits patterns of superimposed cooling and warming processes, which are related to different phases of the drilling of the well. The drilling operations lasted over a total period of 13 days for the 3L-38 well, and 11 days for the 4L-38 well from spud-in to cementing of the wells (Table 3.3). In the 5L-38 well, which was drilled with a larger diameter and cored in the interval between 886 m and 1151 m, drilling operations lasted a total of 29 days, which is more than twice as long as in the two observation wells. The drilling of the permafrost and gas hydrate layers required that the borehole was not excessively heated during the drilling procedure, and the drilling mud was cooled to temperatures between about -2 °C and +4 °C (*Takahashi et al.*, 2005).

As a consequence of the temperature difference between the formation and the drilling mud, the formation was warmed in the upper section and cooled in the lower section of the borehole during the drilling period. This pattern of thermal disturbance is typically observed in rotary-drilled wells (*Bullard*, 1947). After the drilling, the cementing of the

casing caused an increase of temperature along the entire depth of the wells due to the release of the heat of hydration. Despite the complex processes, it has been shown that under certain conditions the process of heat transfer during drilling can be approximated by an idealized line-source model (e.g. *Bullard*, 1947; *Lachenbruch and Brewer*, 1959).

For shut-in times after the end of drilling t_s which are large relative to the time of circulation t_c the temperature along the borehole can be approximated by

$$T(t_s) = A \cdot \ln\left(1 + \frac{t_c}{t_s}\right) + T_\infty \tag{3.6}$$

where T_∞ is the undisturbed formation temperature and A is a constant, which in the ideal case would be given by

$$A = \frac{Q}{4\pi\lambda} \tag{3.7}$$

where Q is the rate of heat exchange during drilling per unit length of the borehole, and λ is the thermal conductivity of the surrounding formation.

The minimum time required for the validity of Equation 3.6 is determined from the departure of the real drilling process from the constant-source model. After this time a plot of the observed temperature after shut-in of the well $T(t_s)$ against $\ln(1 + t_c/t_s)$ should yield a straight line of slope A and a value of T_∞ at $\ln(1+t_c/t_s)=0$ (i.e. $t_s \to \infty$). The mobilization of latent heat in the permafrost and gas hydrate intervals during and after drilling is further limiting the applicability of this method. But it has been shown that even for cases involving substantial degradation of permafrost during drilling the straight-line slope is again recovered after sufficient time (*Lachenbruch et al.*, 1982).

Horner-plots of the type described above for various depths are presented in Figure 3.13. For this analysis it was assumed, that the heat source at a particular depth had lasted from the time when the drill bit had first reached this depth until the end of the cementing of the wells (Table 3.3). The resulting circulation times t_c for the chosen depths are ranging from about 12 days in the upper part of the borehole to about 2 days in the lower part (Tables 3.5 and 3.6). Because of this variation of the circulation times, simultaneous measurements at different depths plot at different positions of the abscissa.

The observed temperature changes after the cementing of the wells depict the sequence of events and the amount of heat exchanged between the borehole and the surrounding formation during drilling in reverse order: In the initial period, the temperature along the entire well decreases as a result of the dissipation of the heat of hydration released during the setting of the cement. In the following time, the temperature recovery in the upper and lower part of the borehole shows different trends: At depths greater about 800 m, the part of the borehole which was subject to cooling during the drilling of the well, temperature is again increasing. In contrast to this, the interval above about 700 m was warmed during drilling, and the cooling after the initial period continues.

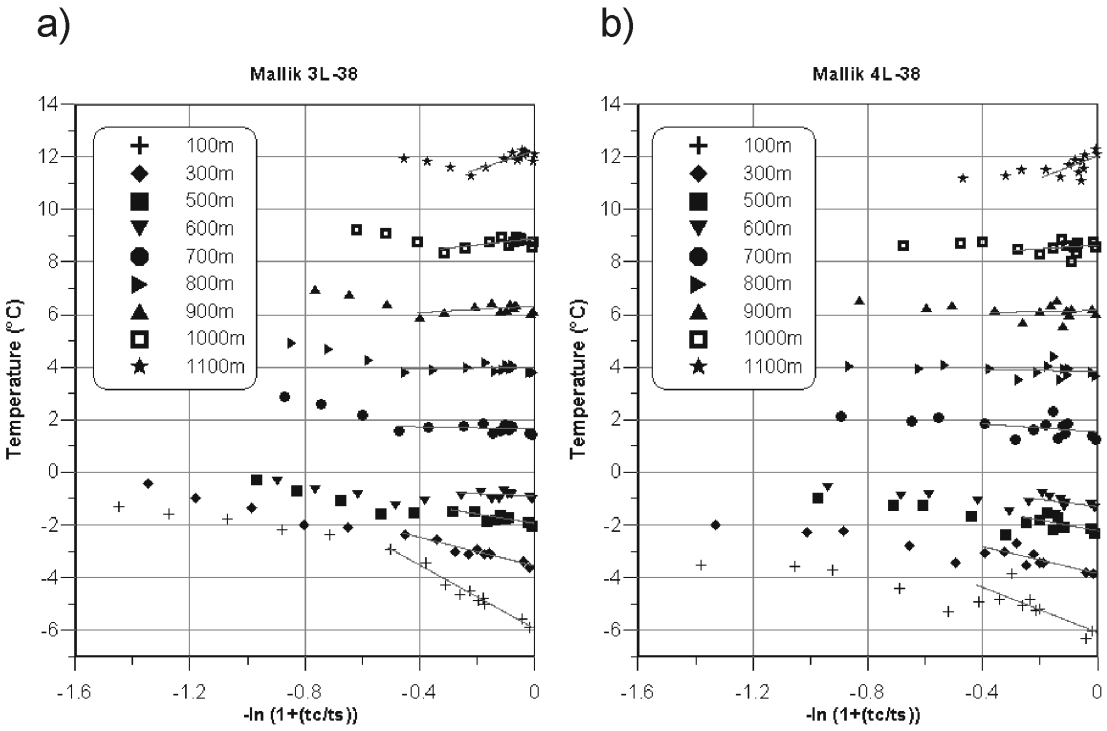

Figure 3.13.: Horner-plot of measured temperature variation over time for various depths, a) Mallik 3L-38, b) Mallik 4L-38 well. Linear fits displayed with solid lines. tc: circulation time, ts: shut-in time. Modified from *Henninges et al.* (2005a).

The linear fits were applied to the Horner-plot data after sufficient shut-in times when a straight-line slope could again be recognized. Because of the lingering influence due to the refreezing of permafrost, data from the permafrost interval generally could only be matched to a straight-line fit after longer shut-in times than for the interval below. Further discussion of the Horner-plot analysis and the temperature effects of the drilling operations can be found in *Henninges et al.* (2005a).

The analysis of the temperature data from the 3L-38 and 4L-48 wells using the Horner-plot method shows that the well temperatures measured during the September 2003 DTS survey have returned close to equilibrium with the formation temperatures. The deviation from thermal equilibrium is about ±0.1 °C (Tables 3.5 and 3.6). Within measurement accuracy, the temperatures of the September 2003 measurement have reached thermal equilibrium, except for the upper part of the permafrost section of the 5L-38 well, where a remaining disturbance due to the testing operations can be observed around 130 m depth (Figure 3.16).

Other studies from deep oil and gas wells have shown, that rather long times, which can take up to several years to decades, are required for the borehole temperatures to return close to thermal equilibrium (e.g. *Lachenbruch and Brewer*, 1959). Compared to these studies, at Mallik a situation close to thermal equilibrium was already attained after a period of approximately 21 months. This can be attributed to the short overall drilling and circulation time of about two to four weeks (Table 3.3). Additionally, the

Table 3.5.: Horner-plot data, Mallik 3L-38. t_c: circulation time; $t_{s,min}$: minimum shut-in time for Horner-plot analysis; A: slope of linear fit; T_∞: estimated undisturbed formation temperature; $T_{Sept.03}$: measured DTS temperature, September 2003; dT: deviation of measured temperature from estimated equilibrium temperature, T_∞ - $T_{Sept.03}$.

Depth (mKB)	t_c (d)	$t_{s,min}$ (d)	A (-)	T_∞ (°C)	$T_{Sept.03}$ (°C)	dT (°C)
100.13	12.37	18.86	6.02	-5.97	-5.88	-0.09
200.12	11.87	18.86	2.87	-4.41	-4.50	0.09
300.11	10.81	18.86	2.72	-3.59	-3.64	0.05
400.10	6.47	18.86	2.69	-2.74	-2.81	0.07
500.09	6.21	18.86	1.81	-1.97	-2.06	0.09
600.08	5.52	18.86	0.40	-0.92	-1.04	0.12
700.07	5.29	8.79	0.21	1.62	1.43	0.19
800.06	5.03	8.79	-0.14	3.96	3.82	0.14
900.05	4.36	8.79	-0.64	6.29	6.10	0.19
1000.04	3.27	8.79	-1.20	8.85	8.74	0.11
1100.03	2.19	8.79	-3.46	12.19	12.09	0.10

Table 3.6.: Horner-plot data, Mallik 4L-38. For explanation of symbols see Table 3.5.

Depth (mKB)	t_c (d)	$t_{s,min}$ (d)	A (-)	T_∞ (°C)	$T_{Sept.03}$ (°C)	dT (°C)
100.05	10.84	21.14	4.31	-6.11	-6.02	-0.09
200.09	10.45	21.14	3.71	-4.71	-4.66	-0.05
300.13	10.14	21.14	2.57	-3.87	-3.85	-0.02
400.18	6.17	21.14	3.81	-3.02	-3.04	0.02
500.22	6.00	21.14	2.02	-2.25	-2.31	0.06
600.01	5.69	21.14	1.33	-1.32	-1.34	0.02
700.05	5.28	10.91	0.76	1.51	1.24	0.27
800.09	5.00	10.91	0.18	3.81	3.65	0.16
900.13	4.71	10.91	-0.20	6.12	6.01	0.11
1000.17	3.52	10.91	-0.71	8.61	8.59	0.01
1100.21	2.19	10.91	-4.19	11.98	12.10	-0.12

temperature of drilling mud was held close to the formation temperature. These factors resulted in a rather small amount of thermal disturbance and a relatively quick return to a state close to thermal equilibrium.

Within Chapter 6 the transient temperature field during and after the drilling and construction of the wells is simulated with the aid of a numerical model; The drilling-induced temperature changes and the effects of phase transitions on the temperature recovery are analyzed in further detail.

3.5.2. Geothermal Gradient

Depth profiles of the temperature gradients calculated from the measured borehole temperature data are displayed in Figures 3.14, 3.15 and 3.16 for selected points in time after the cementing of the wells (shut-in time t_s). The temperature gradient at every data point was calculated from the slope of the temperature profiles over 2 m to 20 m intervals, which is indicated in the respective figure caption. This smoothing of the temperature gradients reduces the influence of the scatter of the raw temperature data due to instrumental noise. The size of the averaging interval was further adjusted to the scale of the diagrams for clarity.

The geothermal gradient is defined as the change of the formation temperature with depth in vertical direction, normal to the earth's surface:

$$\Gamma = \frac{dT}{dz} \tag{3.8}$$

where Γ: Geothermal gradient (K m^{-1})
dT: Change of temperature (K)
dz: Vertical distance (m)

As a result of the thermal disturbance due to the drilling process, the early-time temperature gradient profiles exhibit a high variability which gradually diminishes with time. The specific features of the disturbed temperature gradient profiles are discussed in Section 3.5.3 below. The analysis of the observed variations of temperature with time has shown, that the September 2003 temperature profiles have returned close to equilibrium with the formation temperature (Section 3.5.1). The measured changes of temperature with depth are therefore approximately equal to the geothermal gradient.

According to Fourier's equation of heat conduction, the heat-flow density is equal to the product of thermal conductivity and the temperature gradient. In its three-dimensional form for anisotropic media, both heat-flow density and temperature gradient are vectors in three-dimensional space and thermal conductivity is a three-dimensional tensor. In geothermics, Fourier's first equation is often reduced to its one dimensional form:

$$q = -\lambda_{zz}\Gamma \tag{3.9}$$

where q: Rate of heat flow per unit area (heat-flow density) (W m^{-2})
λ_{zz}: Thermal conductivity in vertical direction (W m^{-1} K^{-1})
Γ: Geothermal gradient (K m^{-1})

Therefore, assuming constant heat flow by conduction, the temperature gradient is inversely proportional to thermal conductivity, and local changes of the geothermal gradient are correlated with changes of the bulk rock thermal conductivity of the formation. Because of this interrelation of thermal conductivity and the geothermal gradient, only the September 2003 "near equilibrium"temperature profiles (i.e. after 622, 605, and 575 days respectively) are considered in the following discussion.

The September 2003 temperature profiles of the three wells all show very similar characteristics. Near the surface to a depth of about 80 m the temperature profiles

exhibit curvature attributable to the annual and recent (several decades) changes of surface temperature (e.g. *Lachenbruch and Marshall*, 1986). The temperature field in the deeper subsurface is characterized by a pronounced increase of the geothermal gradient at the base of the ice-bearing permafrost below about 600 m depth (Figs. 3.14, 3.15, 3.16). The mean temperature gradient within the Mackenzie Bay Sequence rises from 7.4 - 7.9 K km^{-1} above the permafrost base to 23.5 - 24.1 K km^{-1} in the ice-free sediment layers below (Table 3.7). Since there is no apparent change in lithology at this depth, the sharp increase in gradient can mainly be attributed to a change of the bulk rock thermal conductivity resulting from the contrast of the thermal conductivity of the pore fluid in frozen (ice: 2.2 W m^{-1} K^{-1}) and unfrozen (water: 0.6 W m^{-1} K^{-1}) state.

Below about 920 m, the geothermal gradient shows distinct variations and locally increases over 40 K km^{-1} (Figures 3.14, 3.15 and 3.16). The onset of this interval with zones of increased geothermal gradients appears in all three wells and correlates with the boundary between the Mackenzie Bay and Kugmallit sequences, which at the Mallik 5L-38 well appears at a depth of 932.6 mKB (Table 2.1). Individual peaks of the geothermal gradient are again showing good correlation between the Mallik 3L-38 and 4L-38 wells, and local differences can be attributed to lateral changes in lithology which can be derived by comparison of the gamma-ray logs.

Figure 3.17 shows a detail of the 10 m average temperature gradients and the gamma-ray logs of the Mallik 3L-38, 4L-38, and 5L-38 wells, as well as an estimate of the hydrate saturation, based on the difference of the density-porosity and NMR-porosity logs of the 5L-38 well (*Kleinberg et al.*, 2005, Section 4.2.2). As commonly observed, the geothermal gradient correlates with the gamma-ray log. Sand-dominated units, marked by low gamma-ray intensities, characteristically have a higher thermal conductivity than silt- or clay-dominated units with high gamma-ray intensities. In contrast to this, there is no apparent correlation of the temperature gradient and the estimated hydrate saturation, indicating that even high hydrate saturations of up to about 90 % of the pore space only have a minor effect on the bulk rock thermal conductivity.

It should be noted, that the gas hydrate preferentially occurs within the sand-dominated units at Mallik 5L-38 (see also Section 4.2.2, Figures B.4 and B.5). High values of hydrate saturation mostly occur together with low gamma-ray intensities. This is in accordance with the results of the earlier Mallik 2L-38 program, where gas hydrate was also found to occur predominantly within the coarse-grained sandy sediments (*Dallimore et al.*, 1999). The interrelation of geothermal data, lithology, and gas hydrate saturation is further analyzed in Chapter 4, where the in-situ thermal conductivity is estimated from the geothermal gradient.

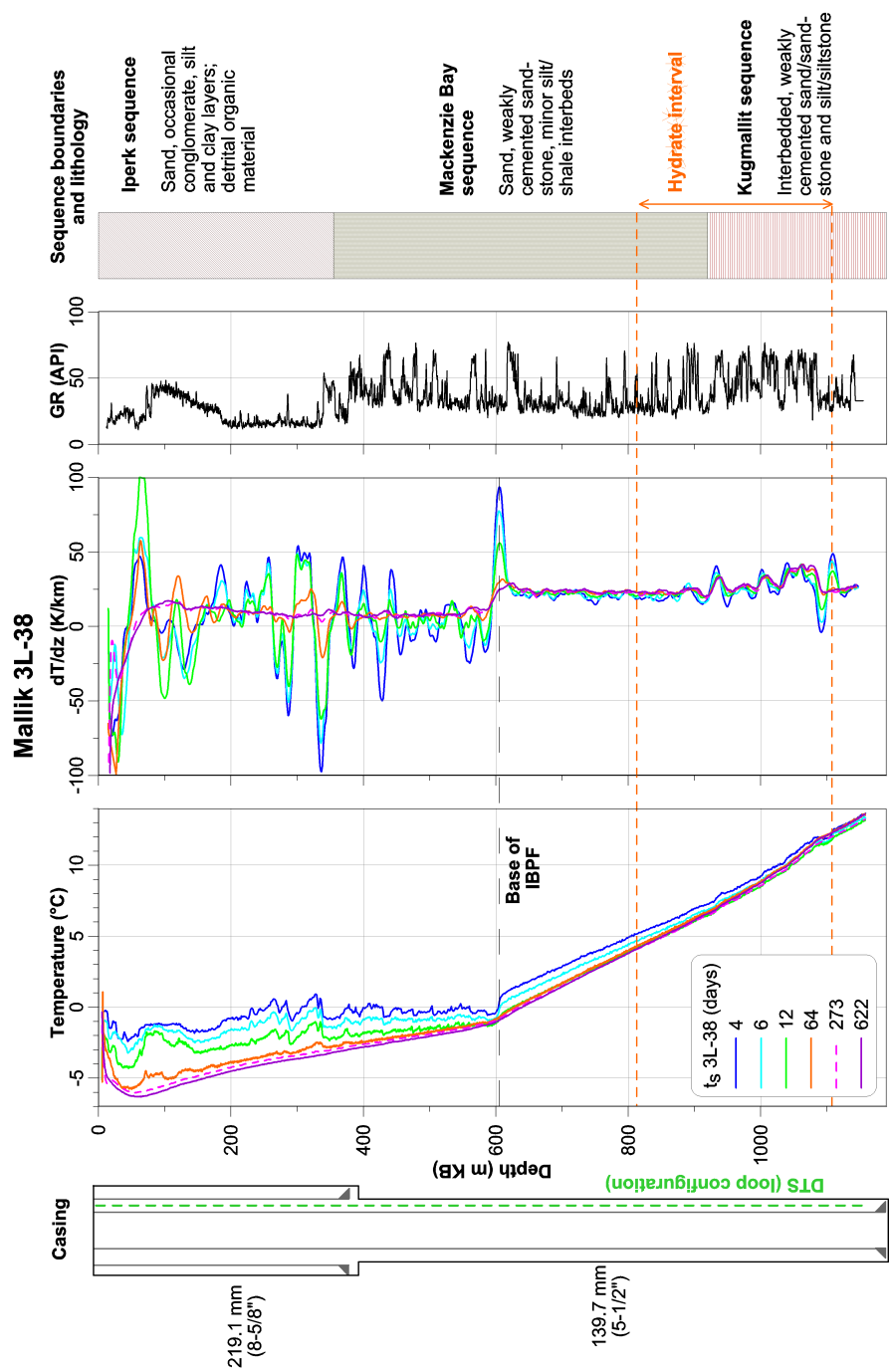

Figure 3.14.: Temperature profiles (T) and 20 m average temperature gradient (dT/dz) of the Mallik 3L-38 observation well for successive times after completion of the well (t_s). IBPF: base of ice-bearing permafrost; GR: gamma-ray intensity (cased-hole log). 273-d temperature profile: uncertain calibration. Sequence boundaries and lithological description modified from *Dallimore et al.* (1999). Modified from *Henninges et al.* (2005a).

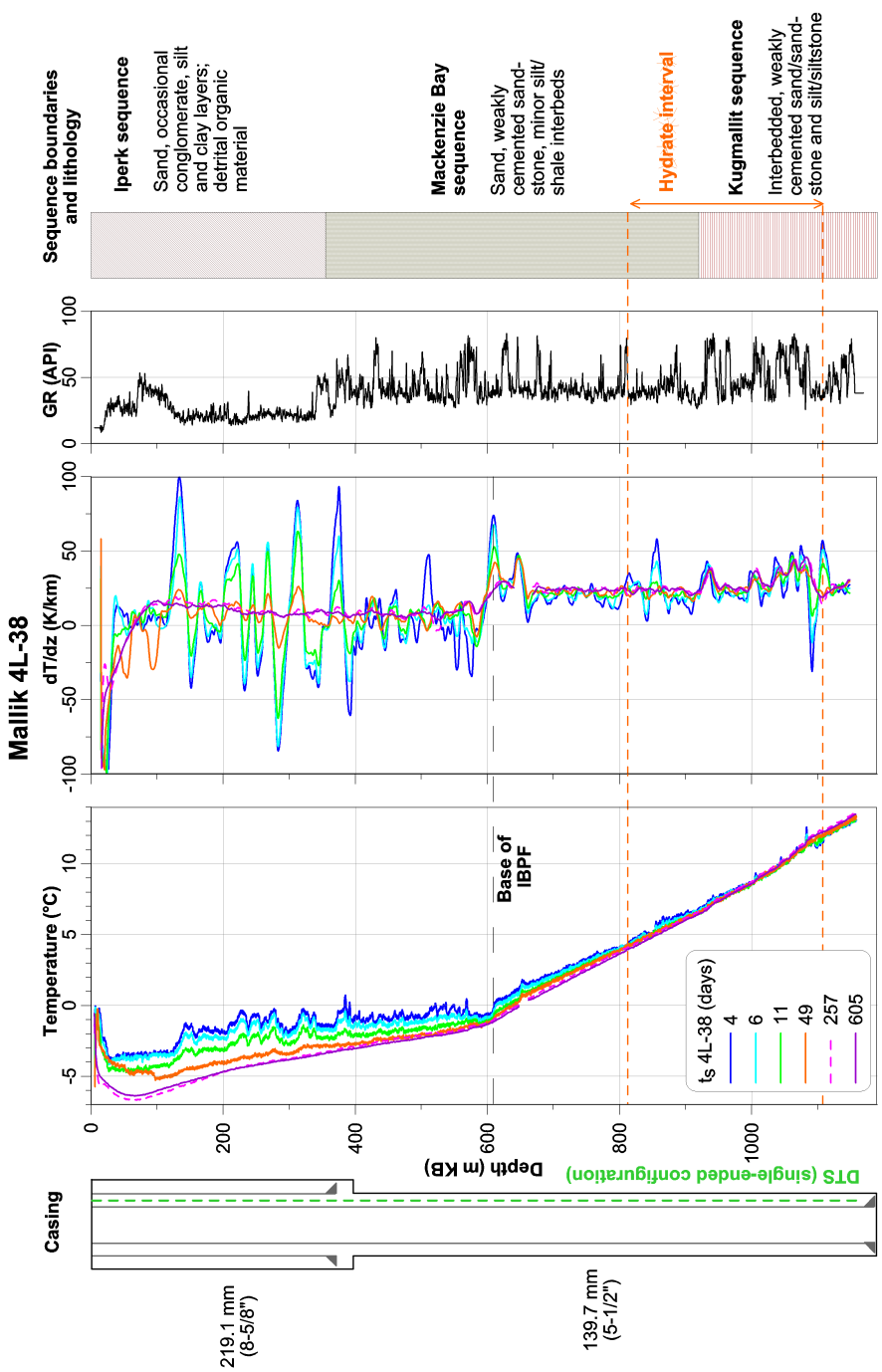

Figure 3.15.: Temperature profiles (T) and 20 m average temperature gradient (dT/dz) of the Mallik 4L-38 observation well for successive times after completion of the well (t_s). IBPF: base of ice-bearing permafrost; GR: gamma-ray intensity (cased-hole log). 257-d temperature profile: uncertain calibration. Sequence boundaries and lithological description modified from *Dallimore et al.* (1999). Modified from *Henninges et al.* (2005a).

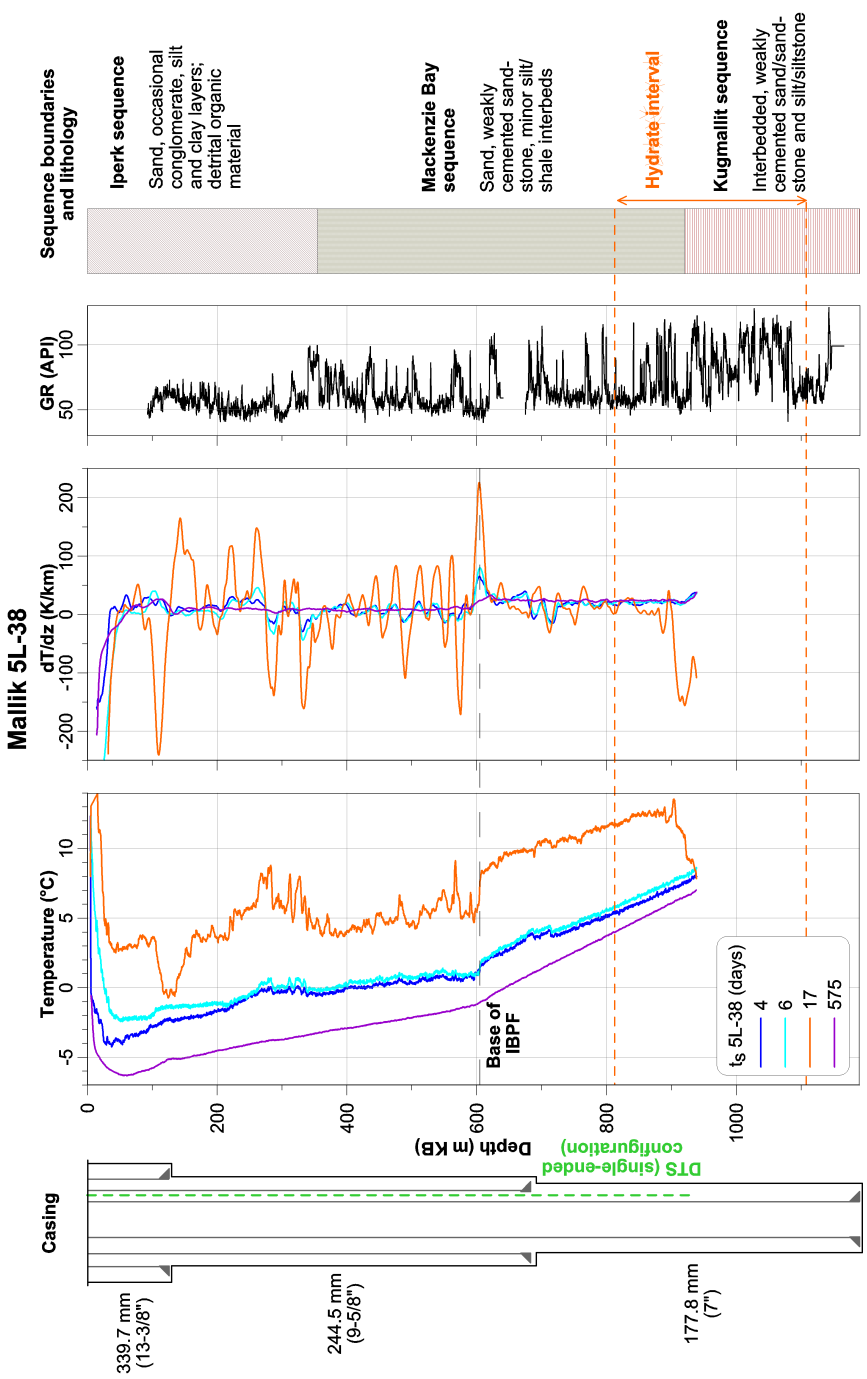

Figure 3.16.: Temperature profiles (T) and 20 m average temperature gradient (dT/dz) of the Mallik 5L-38 production well for successive times after completion of the well (t_s). 17-d temperature profile shows remaining influence from preceded testing operations. IBPF: base of ice-bearing permafrost; GR: gamma-ray intensity (open-hole log, permafrost interval affected by strong washouts). Sequence boundaries and lithological description modified from *Dallimore et al.* (1999). Modified from *Henninges et al.* (2005a).

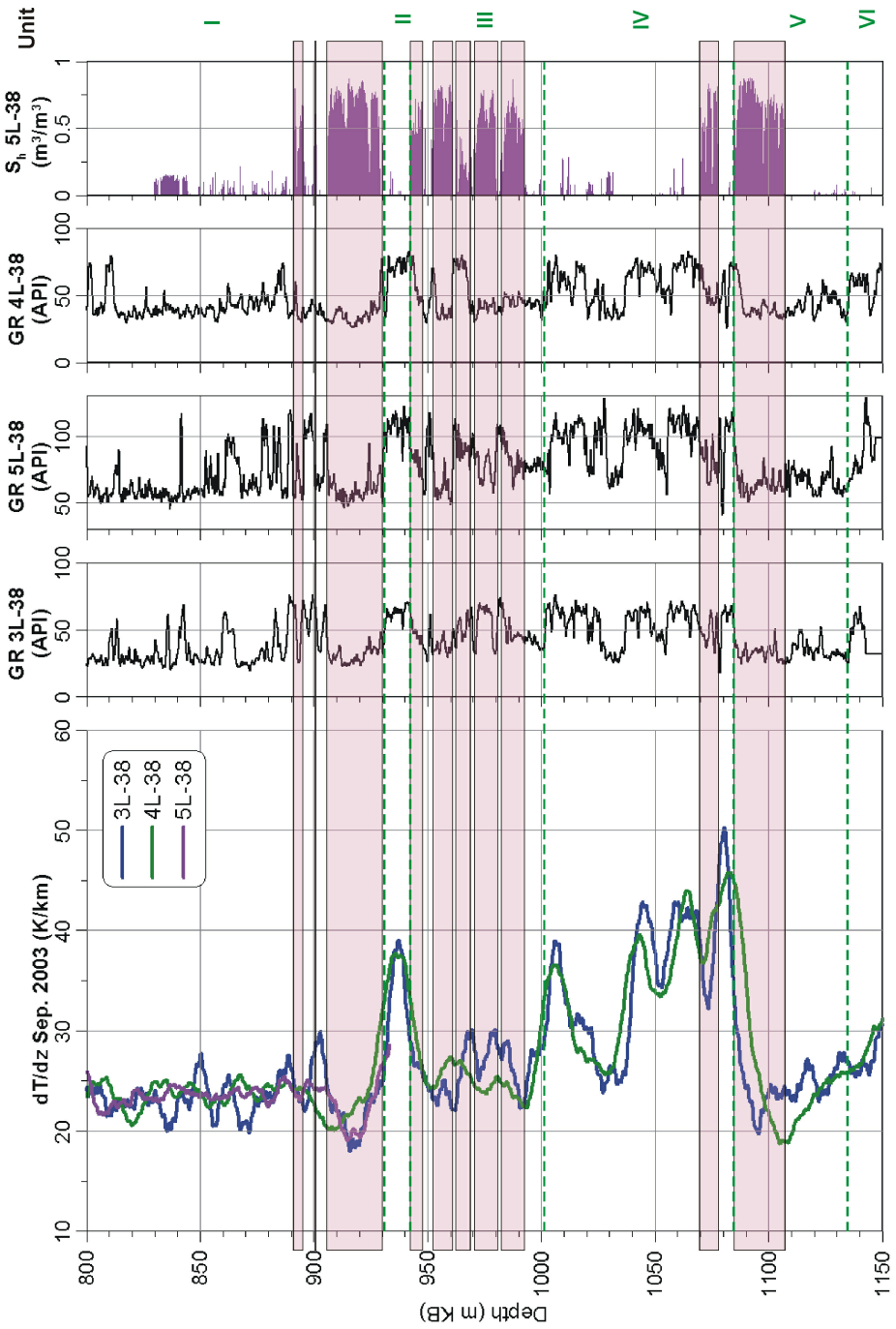

Figure 3.17.: Geothermal gradients (10 m averages, dT/dz), lithological units (after *Medioli et al.*, 2005), and hydrate saturation (S_h) estimated form Mallik 5L-38 well logs (DMR-method, after *Kleinberg et al.*, 2005).

3.5.3. Temperature Gradient Anomalies Resulting from Phase Transitions

The disturbed temperature profiles exhibit specific patterns, which are related to the mobilization of latent heat during the melting and refreezing of permafrost and the decomposition of gas hydrate as a result of the thermal effect from drilling and completion of the wells. In this study, these patterns were used as indicators of the location of the base of the ice-bearing permafrost and gas hydrate occurrences (see also *Henninges et al.*, 2005a).

Especially during early times after the end of drilling, the disturbed temperature profiles are characterized by almost isothermal sections within the permafrost interval, followed by a gradual increase in temperature in the deeper subsurface below (Figures 3.14, 3.15 and 3.16). The transition between these zones is marked by a sharp rise in temperature over a depth interval of a few meters at about 600 m, which is gradually diminishing over time (Figure 3.18).

During drilling, the rise of temperature within permafrost is impeded by the latent heat used to melt the frozen pore fluid, whereas the rise of temperature beneath permafrost is not limited in this way (*Lachenbruch and Brewer*, 1959; *Lachenbruch et al.*, 1982). The resulting transient temperature step marks the base of the ice-bearing permafrost layer and is an effect typical of many wells drilled in permafrost (*Taylor*, 1979). A similar effect can be observed in the depth interval below 1100 m (Figure 3.19). By analogy to the permafrost feature, this indicates that decomposition of hydrate had occurred at the base of the hydrate-bearing zone, probably as a result of a release of heat of hydration after cementing the wells.

Being close to thermodynamic equilibrium, the intervals immediately above the base of the ice-bearing permafrost and gas hydrate occurrences are mostly prone to melting or decomposition respectively. Even small changes of the pressure and temperature conditions can result in phase changes. During the supply of heat, the consumption of latent heat at the phase change or decomposition temperature is leading to the development of isothermal sections of the temperature profiles in the permafrost and hydrate intervals, which are subject to phase changes. In contrast to this, the temperatures in the zones immediately below the melting permafrost or decomposing hydrate interval are increasing according to the thermal diffusivity of the rock.

In comparison to the temperature profiles, the plots of the disturbed temperature gradients (Figures 3.18 and 3.19) accentuate this effect: Within the zones subject to phase changes, the temperature gradients decrease and reach a local minimum, after which the gradients strongly increase with depth (temperature step), before they return to a value close to the geothermal gradient underneath the transition zones. The transition zones between the ice-bearing and non-ice-bearing (Figure 3.18), and between the hydrate-bearing and non-hydrate bearing strata (Figure 3.19) are therefore marked by a sinusoidal signature in the temperature-depth gradient. This anomaly of the temperature gradient and the related temperature step are both gradually decreasing over time as the thermal disturbance dissipates. Chapter 6 contains a more detailed study of the observed temperature gradient anomaly, where the transient temperature field during and after the drilling and construction of the wells was simulated with the aid of a numerical model.

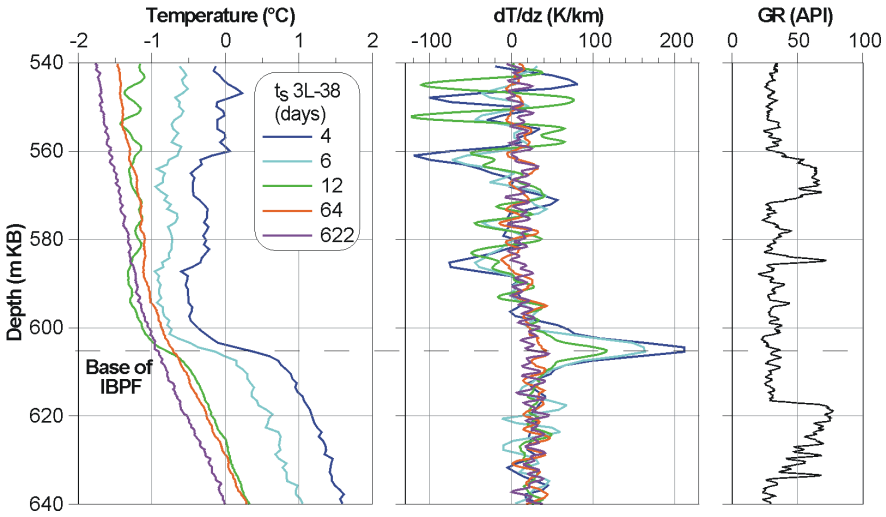

Figure 3.18.: Detail of temperature profiles and 2 m average temperature gradients (dT/dz) at the base of the ice-bearing permafrost (IBPF), Mallik 3L-38. t_s: shut-in time after completion of the well; GR: gamma-ray intensity.

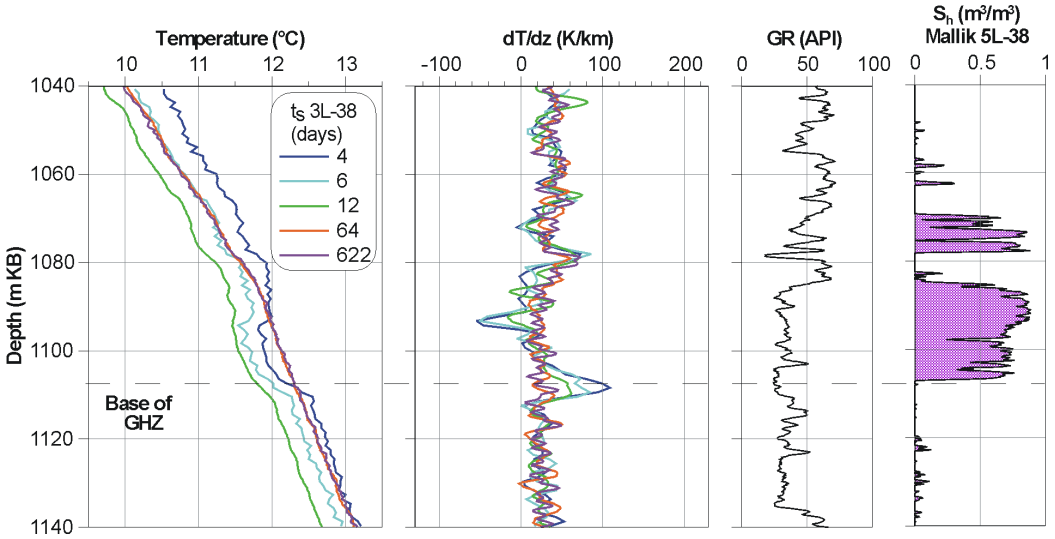

Figure 3.19.: Detail of temperature profiles and 2 m average temperature gradients (dT/dz) at the base of the gas-hydrate zone (GHZ), Mallik 3L-38. t_s: shut-in time after completion of the well; GR: gamma-ray intensity; S_h: hydrate saturation estimated form Mallik 5L-38 well logs (DMR-method, after *Kleinberg et al.*, 2005).

Table 3.7.: Temperature profile data and depths of permafrost and hydrate occurrences at Mallik. $\Gamma_{360-580}$: Mean Sept. '03 temperature gradient, 360-580 mKB depth interval; $\Gamma_{620-900}$: Mean Sept. '03 temperature gradient, 620-900 mKB depth interval; IBPF: ice-bearing permafrost; GHZ: gas hydrate zone (modified from *Henninges et al.*, 2005a).

		3L-38	4L-38	5L-38
$\Gamma_{360-580}$	(K km^{-1})	7.9	7.4	7.8
$\Gamma_{620-900}$	(K km^{-1})	23.5	24.1	23.6
Base of IBPF	(m KB)	604±3.5	609±3.5	605±3.5
Temperature	(°C)	-0.9±0.3	-1.2±0.3	-1.1±0.3
Base of GHZ	(m KB)	1108±3.5	1109±3.5	no data
Temperature	(°C)	12.3±0.3	12.3±0.3	no data

The temperature steps occur within depth intervals of about 7 m. Within these transition zones, the locations of the local maxima of the temperature gradients were used to determine the position of the base of the ice-bearing permafrost and the gas hydrate occurrences (Table 3.7). With respect to the thickness of the transition zones, an uncertainty of ±3.5 m should be assumed for the given depth values for the positions of the respective interfaces. Moreover, at least around the base of the ice-bearing permafrost, a gradual transition zone of variable thickness with coexisting ice and water within the pore space will probably exist.

The depth to the base of the ice-bearing permafrost increases from 604±3.5 m at 3L-38 to 609±3.5 m at 4L-38. These values generally agree with previous determinations of the depth to the base of the ice-bearing permafrost for the Mallik region (Table 2.3), but they are about 30 m less than the depths determined for the approximately 100 m distant Mallik L-38 and 2L-38 wells (*Dallimore and Collett*, 1999; *Dallimore et al.*, 1999), which were estimated from geophysical well logs since precision well temperatures were not available.

The depth to the base of the gas hydrate occurrence increases from 1108±3.5 m at the 3L-38 well to 1109±3.5 m at the 4L-38 well, and shows the same trend as the depth to the ice-bearing permafrost. A similar determination of the base of the gas hydrate occurrence at the 5L-38 well was not possible because temperatures could only be measured to a depth of about 940 m, but the temperature-derived depths to the base of the gas hydrate occurrences for the 3L- and 4L-38 wells correlate well with the log-derived depth for the 5L-38 well at about 1107 m (Table 2.4).

4. Estimation of the In-situ Thermal Conductivity

4.1. Methods for the Determination of Thermal Conductivity

Information about the in-situ thermal conductivity of the formation can generally be derived by three different methods:

1. Measurements on rock samples
2. In-situ temperature measurements
3. Calculation from petrophysical models

In the framework of the Mallik 2002 program only a very limited number of direct measurements of thermal conductivity on hydrate-bearing rock samples was carried out (*Wright et al.*, 2005). Therefore within this study the in-situ thermal conductivity was estimated from petrophysical models as well as from the measured geothermal gradient.

Petrophysical models can again be grouped into three different categories (e.g. *Somerton*, 1992): The thermal conductivity can be estimated from rock composition (mixing law models), geophysical logging data (empirical models) and theoretical models. Empirical or theoretical models for the thermal conductivity of hydrate bearing sediments have not been developed until now, therefore the in-situ thermal conductivity was calculated using different mixing law models.

A significant amount of literature is devoted to the physical properties of frozen soils, which could represent an equivalent to hydrate-bearing sediments, apart from the contrast of thermal conductivity between ice and hydrate. Frozen soils are of great significance for surface processes and practical applications like the construction of buildings, roads, or pipelines in permafrost regions. A compilation of methods for calculating the thermal conductivity of soils with special consideration of freezing effects can be found in *Farouki* (1981). The method proposed by *Johansen* (1975) was found to be among the best methods for frozen saturated soils. For this type of soils the thermal conductivity is calculated from the content of ice, unfrozen water, quartz, and a fraction of other minerals which summarize the remaining part of the sediment matrix using the geometric mean model described below (Section 4.3). *Farouki* (1981) reported an accuracy of ±35 % for the results produced by the method of *Johansen* (1975).

4.2. A Petrophysical Rock Model from Logging Data

In a simplified model, gas-hydrate-bearing sediment can be thought of as being composed of four components: The sediment matrix is mainly composed of quartz grains

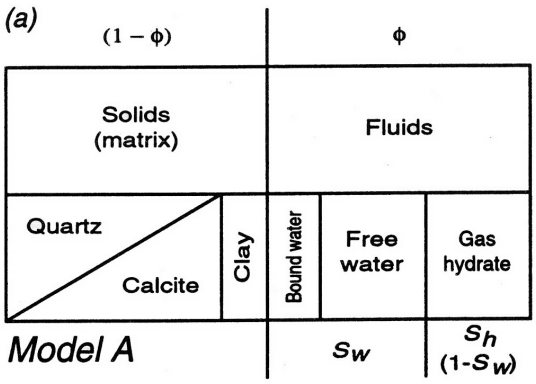

Figure 4.1.: Model for hydrate-bearing sediment. ϕ: porosity, S_w: water saturation, S_h: gas hydrate saturation. Modified from *Collett* (2001).

and shale, and the pore space is filled by water and/or gas hydrate (Figure 4.1). According to the petrophysical measurements which were performed on core samples from Mallik there is strong evidence, that gas hydrate is forming a discontinuous phase within the pore fluid (*Kulenkampff and Spangenberg*, 2005).

The volumetric proportions of each of these components are subject to changes resulting from variations in lithology and hydrate saturation. The volumetric composition, i.e. mineral content of the sediment matrix, porosity, and saturation of the pore filling phases, were estimated from the available geophysical logging data. Some physical data of common rock forming minerals which are important for the detection by geophysical logging methods are listed in Table 4.1.

4.2.1. Shale Content

Shale can be described as a fine-grained detrital sedimentary rock composed of silt and clay minerals. The silt fraction of the sediment grains (<0.063 mm diameter) is composed of variable amounts of quartz, feldspar and organic matter. Both the clay minerals and the feldspar and organic matter of the silt grain fraction can act as a source of radioactivity, because of their content of naturally occurring isotopes of ^{40}K, ^{232}Th, and ^{238}U (see also Table 4.1). The shale content of a succession of sedimentary rocks is therefore often determined from the gamma-ray log reading.

The local gamma-ray intensity GR is linearly scaled between the minimum and maximum gamma-ray intensities, which are equal to the gamma-ray readings in a pure sand and a pure shale within the rock type under investigation:

$$GRI = \frac{GR - GR_{min}}{GR_{max} - GR_{min}} \tag{4.1}$$

Depending on the type of sediment, the age and the degree of consolidation, the shale content V_{sh} is then calculated as a function of the gamma-ray index GRI. For

Table 4.1.: Physical properties of selected minerals. λ = thermal conductivity data measured at room temperature, References: 1 = *Diment and Pratt* (1988), in: *Clauser and Huenges* (1995), 2 = *Brigaud and Vasseur* (1989), 3 = *Sass* (1965), in: *Clauser and Huenges* (1995), 4 = *Horai* (1971), in: *Clauser and Huenges* (1995), 5 = *Timareva et al.* (1970), in: *Cermak and Rybach* (1982), ρ = density data from *Olhoeft and Johnson* (1989), in: *Schön* (1996), GR = typical gamma-ray intensities from *Schlumberger* (1985), in: *Ellis* (1987), CEC = cation exchange capacity.

Mineral	Group	λ (W m^{-1} K^{-1})	Ref.	ρ (kg m^{-3})	GR (API)	Gamma source
Muscovite	Mica	0.62 - 3.89	1	2831	$\sim$ 270	K-bearing
Illite	Clay	1.85	2	2660	250-300	K-bearing
Chlorite		3.06	1	2800	180-250	CEC
Smectite		1.88	2	2608	150-200	CEC
Kaolinite		2.64	2	2594	80-130	CEC
Orthoclase	Feldspar	2.34-2.68	3	2570	220	K-bearing
Albite		2.34	3	2620	-	-
Anorthite		2.72	3	2760	-	-
Quartz	Silicate	7.69	4	2648	-	-
Dolomite	Carbonate	5.51	4	2866	-	-
Lignite	Coal	0.3	5	1190	-	-

the Mallik sediments, the following relation was used, which was derived empirically for weakly consolidated sediments of tertiary and younger age (e.g. *Rider*, 1996):

$$V_{sh} = 0.083 \left(2^{3.7\ GRI} - 1\right) \tag{4.2}$$

The uranium, thorium, and potassium concentrations from the Schlumberger HNGS-logs (Hostile Natural Gamma Ray Sonde) were analyzed for indications on the source of the natural gamma radiation. For the most part the gamma-ray curve compensated for uranium content runs parallel to the standard gamma ray curve (Figure B.2). Therefore there is no indication of zones with anomalously high uranium concentrations, e.g. resulting from enrichment of U-bearing heavy minerals.

The thorium-potassium ratio was used as an indicator for the type of clay minerals present. The cross-plot displayed in Figure B.3 shows that the predominant clay minerals are Montmorillonite and Illite. Unit 6 is characterized by a significant occurrence of other micas (e.g. Muscovite).

The shale content V_{sh} was calculated from the standard gamma-ray curve HSGR (Figure B.2). The HSGR curve was selected as the best indicator for the shale content because of the observed variations in clay mineralogy and the fact that no uranium anomalies were observed. The calculated V_{sh}-values were calibrated using the available grain-size analysis data from 213 core samples from the Mallik 5L-38 well (*Medioli et al.*, 2005). The GR_{min} and GR_{max} values in Equation 4.1 were successively adjusted until a good fit with the measured silt grain fractions was achieved (Figure B.2). The

Table 4.2.: Average mineral composition (weight fraction) calculated from the results of 18 X-ray diffraction analyses of the clay mineral fraction of shale samples from the Mallik 5L-38 well (data from *Medioli et al.*, 2005). M.L.C. = mixed layer clays.

Mineral	Minimum	Maximum	Average
Smectite and/or expandable M.L.C.	0.03	0.21	0.10
Mica (Illite/Muscovite)	0.09	0.35	0.20
Kaolinite	0.06	0.23	0.16
Chlorite (Clinochlore)	0.06	0.20	0.15
Quartz	0.13	0.69	0.38
Feldspars (K-, Na-)	0.00	0.08	0.02

plausibility of the resulting GR_{max}-value was checked by estimating the theoretical gamma-ray intensity of a pure shale with the mineral composition of the Mallik core samples.

The total gamma-ray intensity GR of a sediment can be estimated from the weight fraction n_i and the gamma-ray activities GR_i of the contained minerals:

$$GR = \sum n_i \, GR_i \tag{4.3}$$

The average mineral composition of the clay fraction was determined from the available X-ray diffraction analyses (Table 4.2). The adjusted GR_{max}-value of 95 API units lies about 23 % below the average of the scale of values predicted by Equation 4.3, which fall between 107 API and 140 API. The matching of the order of magnitude can nevertheless be regarded as a confirmation of the adjusted GR_{max}-value used for the calculation of V_{sh}, taking into account the obvious uncertainties which are tied to the application of Equation 4.3.

4.2.2. Porosity and Gas Hydrate Saturation

Kleinberg et al. (2005) have proposed the Density-Magnetic Resonance (DMR) Method in order to determine the gas hydrate saturation from geophysical well logs. Comparison with measurements on core samples from the Mallik 5L-38 well (*Kulenkampff and Spangenberg*, 2005) have shown, that gas hydrate saturation can quantitatively be estimated using the DMR method.

One of the routinely applied methods for the determination of porosity is the calculation of the gamma-gamma density log apparent porosity, $DPHI$, from the gamma-gamma density log:

$$DPHI = \frac{\rho_{ma} - \rho}{\rho_{ma} - \rho_w} \tag{4.4}$$

where

ρ : Gamma-gamma bulk density (kg m^{-3})
ρ_{ma} : Matrix density (kg m^{-3})
ρ_w : Density of pore content (kg m^{-3})

In a water saturated sandstone environment ρ_{ma} is relatively constant around 2650 kg m^{-3} and the density of the pore content is equal to the density of water (1000 kg m^{-3}). However, if an additional phase is present inside the pore space, the density and saturation of this phase has to be taken into account as well.

Nuclear magnetic resonance (NMR) logging tools respond quantitatively to pore space liquid water but not to gas hydrate (*Kleinberg et al.*, 2003). With the DMR method, the gas hydrate saturation S_h is computed from the difference between $DPHI$ and the magnetic resonance apparent porosity ($TCMR$) (*Kleinberg et al.*, 2005):

$$S_h = \frac{DPHI - TCMR}{DPHI + \alpha\, TCMR} \tag{4.5}$$

where

$$\alpha = \frac{\rho_w - \rho_h}{\rho_{ma} - \rho_w} \tag{4.6}$$

and

ρ_h : Density of methane hydrate (=910 kg m^{-3})

The effect of the density contrast between gas hydrate and water on the density porosity can be taken into account with the following equation for the true porosity ϕ:

$$\phi = \frac{DPHI + \alpha\, TCMR}{1 + \alpha} \tag{4.7}$$

However, because of the relatively small density contrast between gas hydrate and water, strong effects will only occur at high porosities (i.e. >40 %) and high gas hydrate saturations (i.e. >50 %).

The computed gas hydrate saturations are displayed in Figure B.4 and Figure B.5. Exceptions to the application of the DMR method described above are individual intervals containing layers of low-rank coal and dolomite-cemented sandstones (Table B.1, see Section 2.2). Because of the strong density contrast compared to other rock-forming materials (see Table 4.1), the DMR method is not applicable and the computed gas hydrate saturation was set to zero within the affected intervals.

Ten individual hydrate-bearing zones with thicknesses between 1 m and 23 m, and average gas hydrate saturations between 25 % and 68 % were identified using the DMR method (Table 4.3). Significant accumulations of gas hydrate predominantly occur inside the sandstone units, with maximum saturations of up to 89 %.

4.3. Thermal Conductivity Profiles from Mixing Law Models

4.3.1. Method

Mixing law models are based on the concept that the effective properties of a multi-component system can be calculated as the average value of the properties of the components and their volumetric fraction of the bulk rock composition. Different averaging methods can be applied depending on the arrangement of the components relative to

Table 4.3.: Major log-derived gas hydrate intervals at Mallik 5L-38 and maximum as well as average gas hydrate saturation (S_h) determined from Density-Magnetic-Resonance method.

Layer ID	Top (mKB)	Bottom (mKB)	Thickness (m)	S_h DMR Max. (m^3/m^3)	S_h DMR Avg. (m^3/m^3)
H1-1	890.63	895.50	4.88	0.83	0.45
H1-2	900.23	901.29	1.07	0.59	0.40
H1-3	906.02	929.34	23.32	0.87	0.68
H3-1	942.44	947.78	5.33	0.72	0.54
H3-2	951.59	961.03	9.45	0.84	0.66
H3-3	962.56	969.42	6.86	0.60	0.25
H3-4	970.33	980.39	10.06	0.86	0.59
H3-5	982.07	992.73	10.67	0.88	0.52
H4-1	1069.54	1077.77	8.23	0.89	0.56
H5-1	1085.24	1106.88	21.64	0.89	0.66

each other (e.g. *Beck*, 1988). The *weighted arithmetic mean model* and the *harmonic mean model* are physically based models which can be derived for heat flowing parallel and perpendicular to the structure in a layered medium. Their results are forming the upper and lower limits of the possible scale of values. The *geometric mean model* was derived empirically (*Woodside and Messmer*, 1961). It was successfully applied for drill cuttings (*Sass et al.*, 1971) and isotropic sedimentary rocks (*Brigaud and Vasseur*, 1989).

The thermal conductivity was calculated using the following formulas for the arithmetic, harmonic, and geometric mean models (e.g. *Beck*, 1988):

$$\lambda_{ari} = \sum v_n \lambda_n \tag{4.8}$$

$$\lambda_{har} = \frac{1}{\sum v_n / \lambda_n} \tag{4.9}$$

$$\lambda_{geo} = \Pi \lambda_n^{v_n} \tag{4.10}$$

where $\lambda_{ari}, \lambda_{har}, \lambda_{geo}$: Effective thermal conductivities (W m^{-1} K^{-1})
λ_n: Thermal conductivity of n-th component (W m^{-1} K^{-1})
v_n: Ratio of volume of n-th component to total volume (-)

If v_n is expressed as the fractional volume, then $\sum v_n = 1$.

The volumetric composition of the formation was determined from the available logging data using different methods of formation evaluation (Section 4.2). The individual volume fractions relative to the total rock volume were be computed using the following set of equations, where the subscripts sd, sh, w, and h respectively refer to sand, shale, water, and hydrate:

$$v_{sd} = (1 - \phi) \cdot (1 - V_{sh}) \tag{4.11}$$

$$v_{sh} = (1 - \phi) \cdot V_{sh} \tag{4.12}$$

$$v_w = \phi \cdot (1 - S_h) \tag{4.13}$$

$$v_h = \phi \cdot S_h \tag{4.14}$$

Although only of limited extent (Figure 4.2), special attention had to be devoted to the intervals containing low-rank coal and dolomite-cemented sandstone beds. Within the concerned intervals (see Section 2.2), the following procedure was applied: The true porosity (ϕ) was set equal to the magnetic resonance apparent porosity ($TCMR$, see Section 4.2.2). The shale volume (v_{sh}) was calculated as usual from Equation 4.12, and the remaining volume of the rock matrix was assumed to be composed of coal or dolomite respectively, resulting in a computation of v_{coal} and v_{dol} equal to v_{sd} from Equation 4.11.

Except for water and methane hydrate, where the values of the pure substances were used, effective thermal conductivities of the mineral mixtures which are represented by each component were used (Table 4.4). The effective thermal conductivity of shale was calculated from the average mineral composition determined by X-ray diffraction analysis (Table 4.2) and the thermal conductivity of the mineral components (Table 4.1) using the harmonic mean model. The harmonic mean model was chosen because of the preferentially layered structure of shale resulting from the contained sheet silicates, and the direction of heat-flow was assumed to be perpendicular to the orientation of the layering. The value for sand was chosen about 10 % lower than the value of pure quartz, accounting for a small amount of impurities from other minerals like carbonates or feldspar, which is consistent with the procedures of other authors (e.g. *Revil*, 2000).

4.3.2. Results

The calculated thermal conductivity profiles using the three different mixing laws are displayed in Figure 4.2. An attempt to quantify the uncertainty associated with the results of the mixing law models was not made because of the empirical nature of some of the underlying calculations (Section 4.2) and the absence of appropriate comparative values.

The arithmetic mean model results in the highest and the harmonic mean model in the lowest values of thermal conductivity (Figure 4.2). Intermediate values of thermal conductivity were calculated from the geometric mean model. The largest differences

Table 4.4.: Thermal conductivities of components for mixing law models.

Component	Thermal conductivity ($W\ m^{-1}\ K^{-1}$)
Sand	7.0
Shale	1.9
Water	0.6
Hydrate	0.45
Coal	0.3
Dolomite	7.0

of the results occur in the sand-dominated sections of the profile, whereas similar values were calculated for the sections containing a high amount of shale. This is consistent with the results of other authors: *Beck* (1988) states, that at low contrasts of thermal conductivity (i.e. below a factor of 5) all three of the above models show similar results, and the values calculated using the geometric mean model approximately fall into the middle of the scale of values. It should be noted, that *Clauser and Huenges* (1995) have reported a failure of the geometric mean model for higher conductivity contrasts above a factor of 10.

Table 4.5 contains a compilation of the average thermal conductivity values of the different lithological units which were further subdivided according to the hydrate saturation of individual intervals. The average thermal conductivity values calculated using the geometric mean model range between about 1.5-2.0 W m^{-1} K^{-1} within the shale-rich units and about 2.0-2.8 W m^{-1} K^{-1} within the sand-dominated units. The lowest values were calculated for the sporadic coal-bearing sections, ranging between about 0.4 W m^{-1} K^{-1} and 1.0 W m^{-1} K^{-1}. Maximum values between about 4.0 W m^{-1} K^{-1} and 5.9 W m^{-1} K^{-1} were calculated for the isolated layers of dolomite-cemented sandstones.

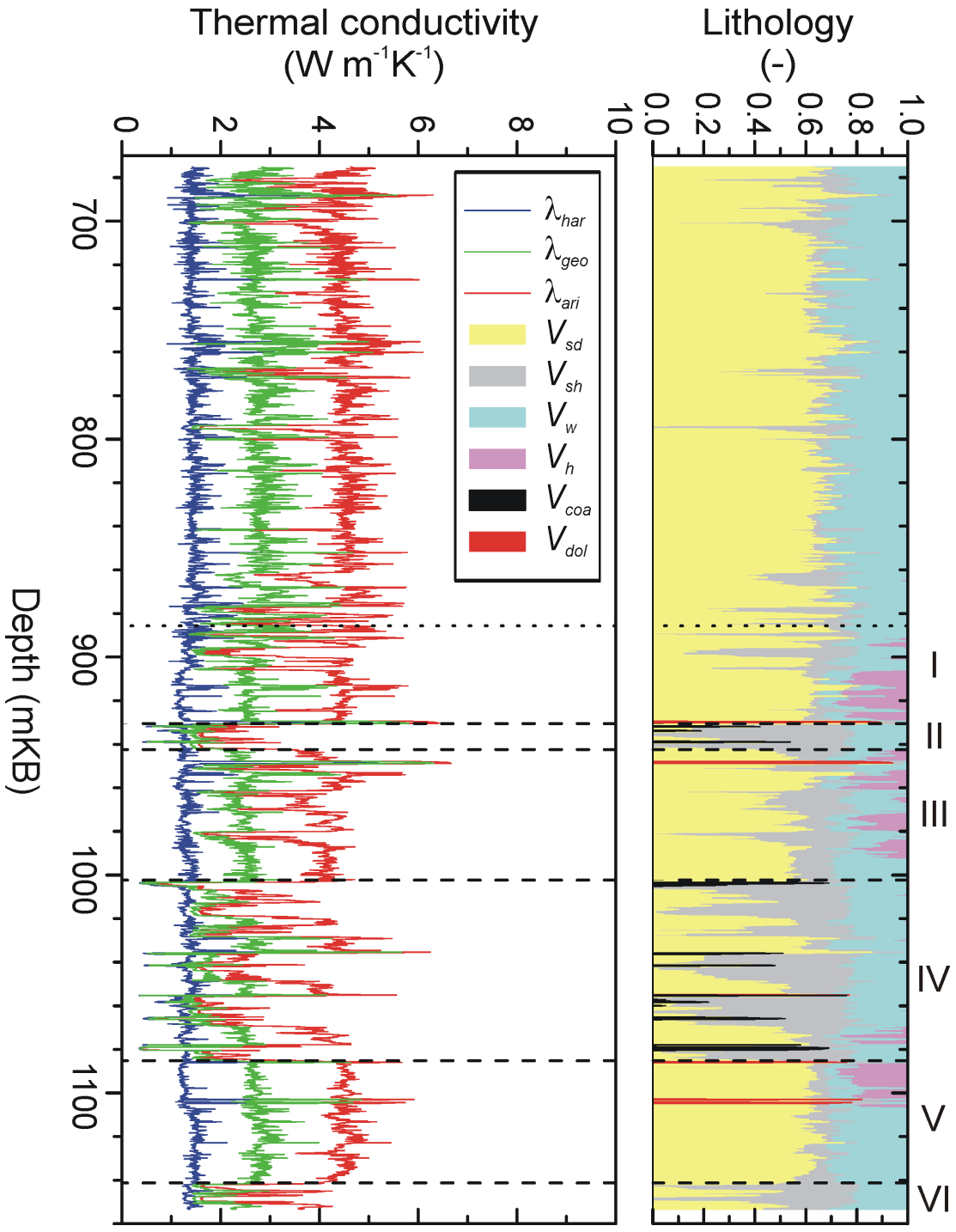

Figure 4.2.: Comparison of thermal conductivity profiles for Mallik 5L-38 well calculated from arithmetic, geometric, and harmonic mean mixing law models. Lithological composition derived from logging data. Roman numerals: lithological units adopted from *Medioli et al.* (2005).

Table 4.5.: Average calculated thermal conductivity values (W m^{-1} K^{-1}) and lithological data of sub-sections of lithological units derived from well-logs of the Mallik 5L-38 well.

Unit	Top (mKB)	Bottom (mKB)	Thickness (m)	V_{sh} (-)	ϕ (-)	S_h (-)	λ_{ari}	λ_{geo}	λ_{harm}	λ_{zz} 3L-38	λ_{zz} 4L-38	λ_{zz} 5L-38
1-1	876.50	906.02	29.52	0.41	0.28	0.16	3.63	2.41	1.42	2.17±0.32	2.16±0.32	2.26±0.33
1-2	906.02	930.50	24.48	0.10	0.33	0.66	4.53	2.74	1.35	2.66±0.39	2.33±0.34	2.88±0.42
2	930.50	942.40	11.90	0.84	0.26	0.02	1.87	1.49	1.19	1.48±0.22	1.32±0.19	1.60±0.25
3-1	942.40	961.03	18.63	0.24	0.30	0.52	4.19	2.67	1.48	2.30±0.33	2.36±0.34	n/a
3-2	961.03	970.33	9.30	0.50	0.27	0.21	3.37	2.19	1.37	1.95±0.28	2.18±0.32	n/a
3-3	970.33	992.73	22.40	0.33	0.31	0.52	3.83	2.35	1.28	2.00±0.29	2.32±0.34	n/a
3-4	992.73	1002.30	9.57	0.23	0.32	0.02	4.13	2.58	1.43	2.02±0.29	2.57±0.37	n/a
4-1	1002.30	1035.90	33.60	0.56	0.28	0.04	2.96	2.05	1.35	1.86±0.27	2.09±0.30	n/a
4-2	1035.90	1069.54	33.64	0.72	0.27	0.02	2.34	1.72	1.26	1.38±0.20	1.54±0.22	n/a
4-3	1069.54	1077.77	8.23	0.27	0.30	0.57	4.05	2.46	1.30	1.70±0.25	2.72±0.40	n/a
4-4	1077.77	1085.20	7.43	0.66	0.25	0.05	1.87	1.44	1.12	1.12±0.16	1.03±0.15	n/a
5-1	1085.20	1106.88	21.68	0.10	0.32	0.67	4.57	2.77	1.34	2.40±0.35	2.68±0.39	n/a
5-2	1106.88	1141.30	34.42	0.13	0.32	0.02	4.48	2.83	1.50	2.19±0.32	2.42±0.35	n/a
6	1141.30	1153.36	12.06	0.69	0.26	0.01	2.69	1.94	1.37	1.96±0.29	1.92±0.28	n/a

4.4. Thermal Conductivity Profiles from Geothermal Gradient

4.4.1. Method

Assuming constant heat flow by conduction, the bulk rock thermal conductivity in vertical direction can be calculated from the measured geothermal gradient and an estimate of the local heat flow by a simple rearrangement of the one dimensional form of Fourier's equation (Equation 3.9):

$$\lambda_{zz} = \frac{-q}{\Gamma} \tag{4.15}$$

where λ_{zz}: Thermal conductivity in vertical direction (W m^{-1} K^{-1})
q: Rate of heat flow per unit area, heat-flow density (W m^{-2})
Γ: Geothermal gradient (K m^{-1})

It should be pointed out, that the success of this procedure is strongly dependent on the validity of the above stated assumption, as well as the quality of the heat-flow density estimate. The applicability of this method can only be proved by evidence from independent data, which in the current study was supplied in the form of petrophysical data derived from well log interpretation (Section 4.5).

The temperature profiles measured at Mallik in September 2003 have returned close to equilibrium with the formation temperature and the changes of temperature with depth are approximately equal to the geothermal gradient (Section 3.5). For the calculation of thermal conductivities average temperature gradient profiles were constructed from the September 2003 temperature profiles. The gradients were calculated from the slopes of linear fits for the temperature profiles over 5 m intervals. The standard error (standard deviation) of the 5 m temperature gradients is calculated as:

$$\sigma_G = \sqrt{\sigma_T^2 \cdot \frac{1}{\sum \xi_i^2}} \tag{4.16}$$

where

$$\xi_i = x_i - \overline{x} \tag{4.17}$$

and

σ_G : Standard error of temperature gradient (K km^{-1})
σ_T : Standard error of DTS temperature data (K)
x_i : Depth of DTS measurement point (m)

For σ_T the estimated experimental temperature resolution (Section 3.4.3) was used. From Equation 4.16, a standard error of 2.6 K km^{-1} for the Mallik 3L-38, and 4.0 K km^{-1} for the Mallik 4L-38 and 5L-38 5 m temperature gradients was calculated.

The 5 m average temperature gradient profiles and a heat-flow density of 55±8 mW m^{-2}, which was derived by *Majorowicz and Smith* (1999) for the nearby Mallik L-38 well (Section 2.3), were used for the calculation of the bulk rock thermal conductivities. The standard error of the resulting thermal conductivity values can be calculated

from the sum of the relative errors of the temperature gradient and heat-flow density data:

$$\left(\frac{\sigma_\lambda}{\lambda}\right)^2 = \left(\frac{\sigma_q}{q}\right)^2 + \left(\frac{\sigma_G}{\Gamma}\right)^2 \tag{4.18}$$

where

σ_λ : Standard error of thermal conductivity (W m^{-1} K^{-1})
σ_q : Standard error of heat-flow density (mW m^{-2})

The average values of the resulting relative errors for the 5 m average thermal conductivity values are 18 %, 23 %, and 25 % for the Mallik 3L-38, 4L-38, and 5L-38 wells respectively.

4.4.2. Results

The calculated 5 m thermal conductivity profiles are displayed in Figure 4.3, together with the 95 % confidence limits, which are equal to $2\sigma_\lambda$. Table 4.5 contains a compilation of the average thermal conductivity values of the different lithological units which were further subdivided according to the hydrate saturation of individual intervals.

Generally the scatter of values is much greater for the Mallik 4L-38 and 5L-38 wells compared to the Mallik 3L-38 well. This is interpreted as a result of the different level of noise associated with the data acquired using single-ended and double-ended measurement processing during the DTS temperature measurements (Section 3.1). Above the base of the ice-bearing permafrost, the calculated conductivity values exhibit a much greater variability than within the underlying sequence of rocks. This is partially interpreted as a result of variations within the ice content of the permafrost, which can lead to a significant increase of thermal conductivity (e.g. Figure 1.3). To some extent the variability could result from a remaining disturbance of the well temperatures from the drilling and construction of the wells within the permafrost interval.

Despite the different scatter of values the thermal conductivity profiles of the three Mallik wells show similar trends below the permafrost base (Figure 4.3). The variation of thermal conductivity with depth shows characteristic patterns, which are correlated with the lithological units described in Section 2.2.

The geothermal values of corresponding sections of the three Mallik 2002 wells are in close agreement (Table 4.5). Individual exceptions can be related to lithological variations between the wells (Figure B.1). The average thermal conductivity values calculated from geothermal data range between 1.03±0.15 W m^{-1} K^{-1} within the shale-rich lower part of Unit 4 of Mallik 4L-38 and 2.88±0.42 W m^{-1} K^{-1} within the sand-rich and hydrate-bearing lower part of Unit 1 of the Mallik 5L-38 well.

Some prominent peaks of the calculated conductivities are clearly related to specific lithological features: The high conductivity interval at the base of Unit 1 within the profile of the 5L-38 well correlates well with the occurrence of a dolomite-cemented sandstone interval (Figure B.4). The low conductivity value near the base of Unit 4 of the Mallik 4L-38 well corresponds to a 1.4 m thick coal layer at the adjacent Mallik 5L-38 well (Figure B.5 and Table B.1).

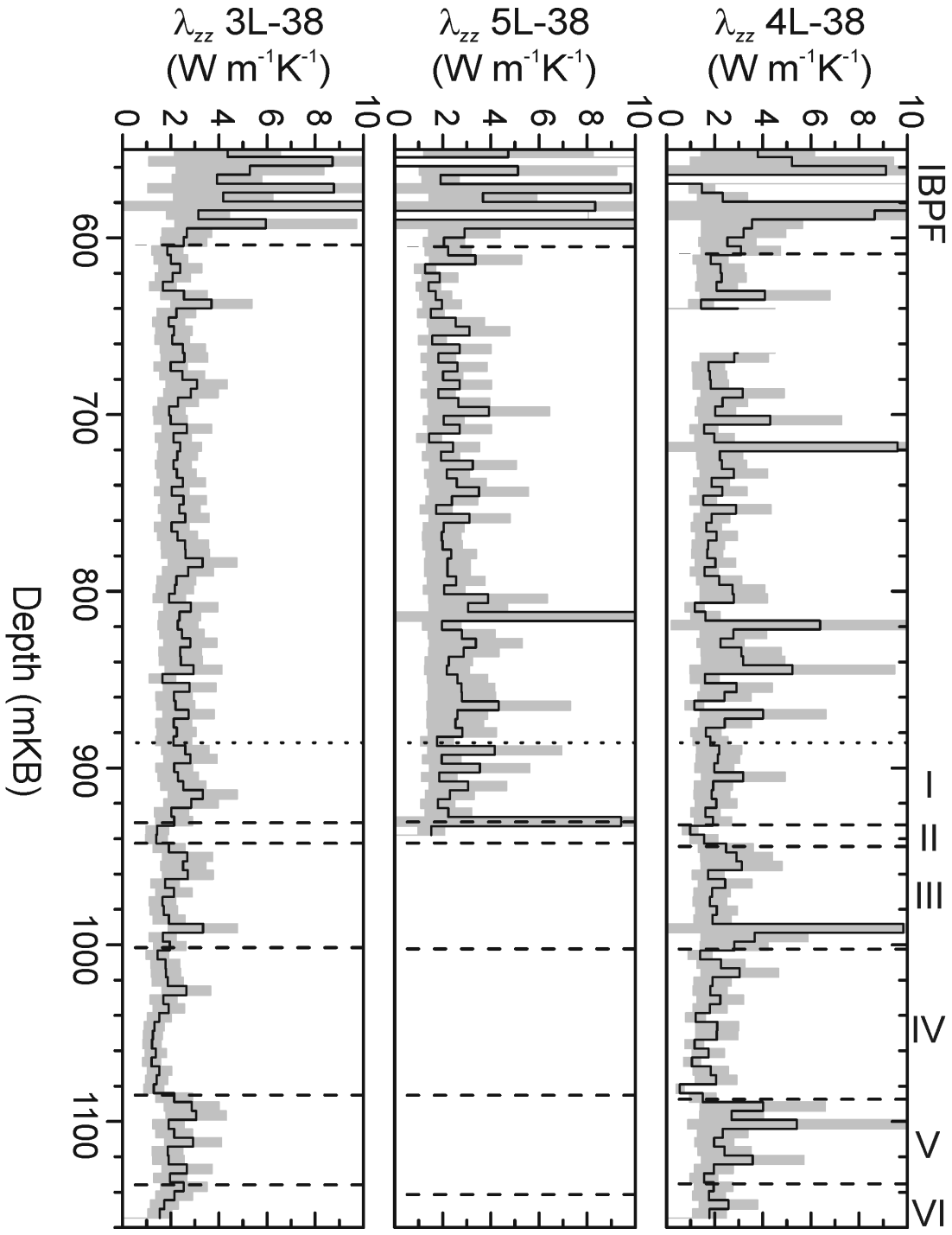

Figure 4.3.: Thermal conductivity profiles calculated from the measured geothermal gradients (September 2003) and the local heat-flow density. Shaded areas: 95 % confidence limits. Roman numerals: lithological units adopted from *Medioli et al.* (2005). IBPF: base of ice-bearing permafrost.

4.5. Comparison of Calculated Thermal Conductivity Profiles

A comparison of the thermal conductivity profiles from the mixing law models and the geothermal data of the the Mallik 5L-38 well is displayed in Figure 4.4. The data is only displayed for the depth interval between 670 m and 970 m depth, in which both temperature and other logging data were available.

The thermal conductivities calculated using the geometric mean model show the best agreement with the conductivities calculated from the geothermal gradient, both in terms of the magnitude of the absolute values as well as the amplitudes of variation. Except for a few isolated values, the geometric mean model values lie within the bandwidth of the 95 % confidence limit of the conductivities calculated from the geothermal gradient. The arithmetic mean model predicts values which are almost constantly above the confidence range. The results of the harmonic mean model lie at or below the lower boundary of the confidence range. This agrees with the results of *Troschke and Burkhardt* (1998), who have observed a good agreement of measured and calculated thermal conductivities using the geometric mean model for sedimentary rocks with small differences of thermal conductivity between the rock matrix and the pore content.

The good agreement of the geometric mean model values and the geothermal data also holds for the 23 m thick interval with high hydrate saturations of up to 87 % at the base of Unit 1 (Table 4.5). This is in accordance with the results of *Wright et al.* (2005), who showed that reasonable estimates of the thermal conductivity of the hydrate-bearing sediments at Mallik were generated using the method proposed by *Johansen* (1975), which for saturated soils is equivalent to the geometric mean model applied in this work.

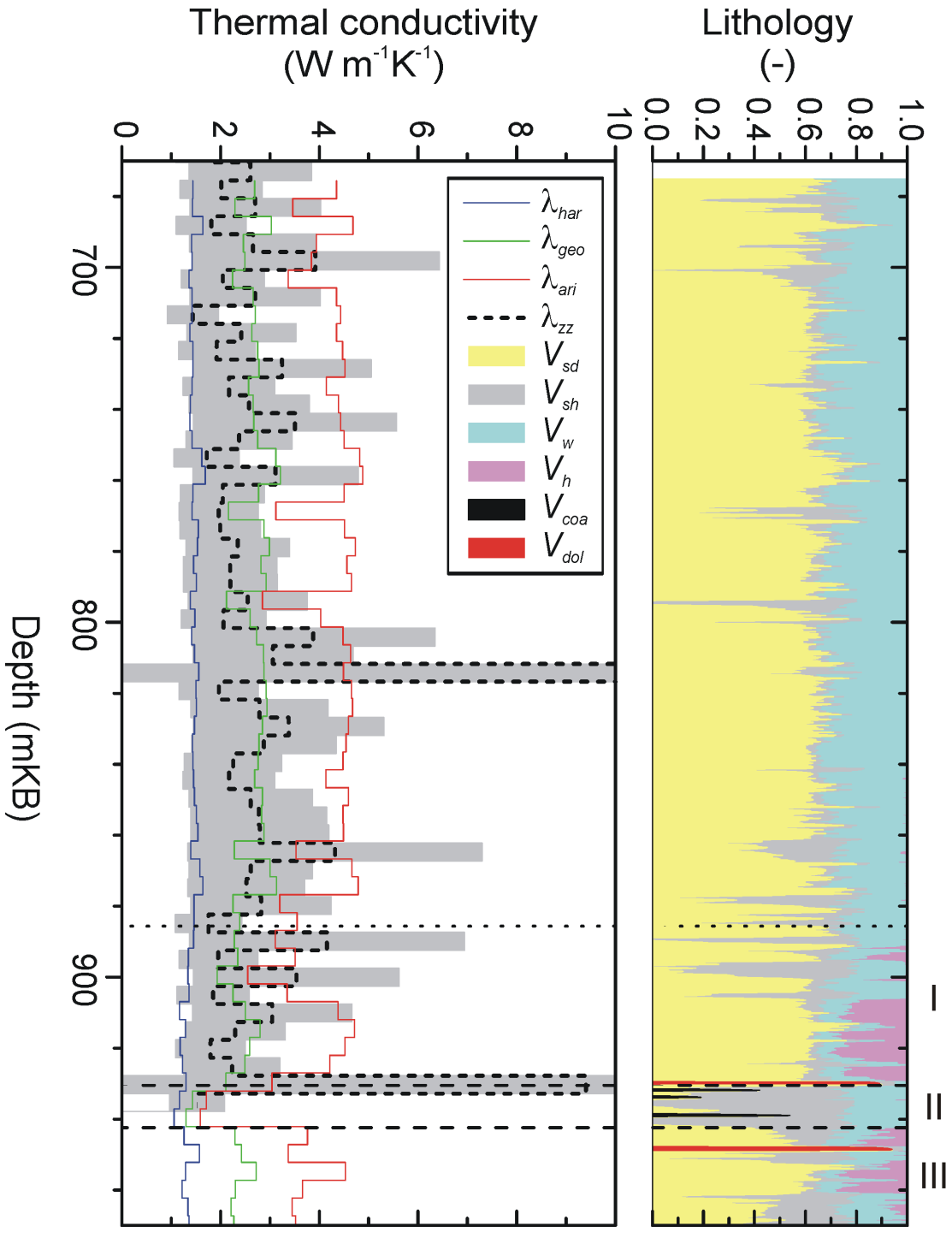

Figure 4.4.: Comparison of thermal conductivity profiles calculated from mixing law models (arithmetic, geometric, harmonic) and the 5-m average temperature gradients (Mallik 5L-38 well, September 2003). For better comparability, the mixing law conductivities are correspondingly displayed as 5-m arithmetic average values. Roman numerals: lithological units adopted from *Medioli et al.* (2005).

5. A Simplified Model for Methane Hydrate Destabilization

5.1. Physical Reaction and Properties

Gas hydrates are ice-like solids known as clathrates or cage compounds. The crystal lattice is made up of water molecules tied together by hydrogen bonds. The cavities in the crystal lattice are occupied by other molecules referred to as *guests*.

The underlying physical reaction leading to the formation or decomposition of hydrate can generally be expressed as:

$$M + N(H_2O) \Leftrightarrow M \cdot (H_2O)_N \tag{5.1}$$

where M : Guest molecule
N : Hydration number

and $M \cdot (H_2O)_N$ denotes the hydrate phase.

Apart from methane (CH_4), other guest molecules can be included in the clathrate structure, which under conditions encountered in nature could be other hydrocarbons like ethane (C_2H_6), propane (C_3H_8) or butane (C_4H_{10}), or other gases like carbon dioxide (CO_2), or nitrogen (N_2). The size of the guest molecules determines the crystal structure of the hydrate, which can be either cubic (structure I and II) or hexagonal (structure H). Both the physical properties and the equilibrium thresholds depend on the crystal structure.

At Mallik, the methane content of the gas from the recovered hydrate samples is greater than 99.5 % (Section 5.3.3). Thermodynamic calculations predict that structure I gas hydrate is present under the in-situ P/T-conditions within the zone of the observed gas hydrate occurrences at Mallik (Section 5.4). For a structure I methane hydrate, the ideal guest/water ratio is 1 : 5-3/4 (e.g. *Sloan*, 1998). Because in nature not all of the cavities are occupied by a guest molecule, hydrates always contain more water molecules than the ideal structure.

Because of the negligible effect of the relatively small amount of other gases present than CH_4, a pure structure I methane hydrate with an average hydration number of 6 is assumed for the purpose of this study. Literature values of the physical properties of methane hydrate are listed in Table 5.1.

5.2. Volumetric Balance

The volume of water and methane gas generated during the decomposition of methane hydrate can be calculated from the density and the molecular weight of the components involved in the reaction expressed in Equation 5.1:

Table 5.1.: Physical properties of structure I methane hydrate.

Property	Unit	Value	Reference
Density	kg m^{-3}	910	*Sloan* (1998)
Thermal conductivity	W m^{-1} K^{-1}	0.45	*Stoll and Bryan* (1979)
Specific heat capacity	J kg^{-1} K^{-1}	1650	*Rueff et al.* (1988)
Enthalpy of decomposition	kJ kg^{-1}	429.66	*Rueff et al.* (1988)

$$V_x^h = M_x^h \frac{\rho_h}{\rho_x} \tag{5.2}$$

$$M_x^h = \frac{m_x}{m_h} \tag{5.3}$$

where V_x^h : Volume of component x generated from unit volume of hydrate (-)
M_x^h : Mass fraction of component x stored in hydrate (-)
ρ_x : Density of phase x (kg m^{-3})
m_x : Molecular weight of component x per formula unit (g $mole^{-1}$)
x : Index of component or phase (m=methane, w=water)
h : Hydrate phase

Under in-situ conditions of 11.25 MPa and 12.3 °C (Section 5.3), about 1.60 m^3 of methane gas and 0.79 m^3 of water are generated per m^3 of methane hydrate, assuming an average hydration number of 6 and molecular weights of m_h=124 g $mole^{-1}$, m_w=6·18 g $mole^{-1}$, m_m=16 g $mole^{-1}$, and densities of ρ_h=910 kg m^{-3}, ρ_w=1000 kg m^{-3}, and ρ_m=73.5 kg m^{-3}. Because of the low solubility of methane in water, the effect of methane going into solution can be neglected in the volumetric balance: A solubility of 100 millimole per liter (*Davie et al.*, 2004, 10 MPa, 285 K) would reduce the volume of the generated methane gas about one percent.

It is important to note, that under in-situ conditions the volumetric proportion of methane gas generated is much smaller than for standard conditions, where about 164 m^3 of gas per m^3 of hydrate are generated (ρ_m at standard conditions: 0.656 kg m^{-3}). The above given density of methane gas was therefore adjusted for in-situ conditions, assuming an ideal gas behavior.

In extension of the rock model of a hydrate-bearing sediment introduced in Section 4.2, the volume of water (v_w^h) and methane gas (v_m^h) generated from the decomposition of hydrate can be calculated as:

$$v_w^h = v_h V_w^h \tag{5.4}$$

$$v_m^h = v_h V_m^h \tag{5.5}$$

An example of a volumetric balance for the model sediment considered in Chapter 6, with $\phi = 0.32$ and $S_h = 0.70$, is displayed in Figure 5.1. Of course the sum of the phases present inside the pore space can not exceed the sediment porosity. For the

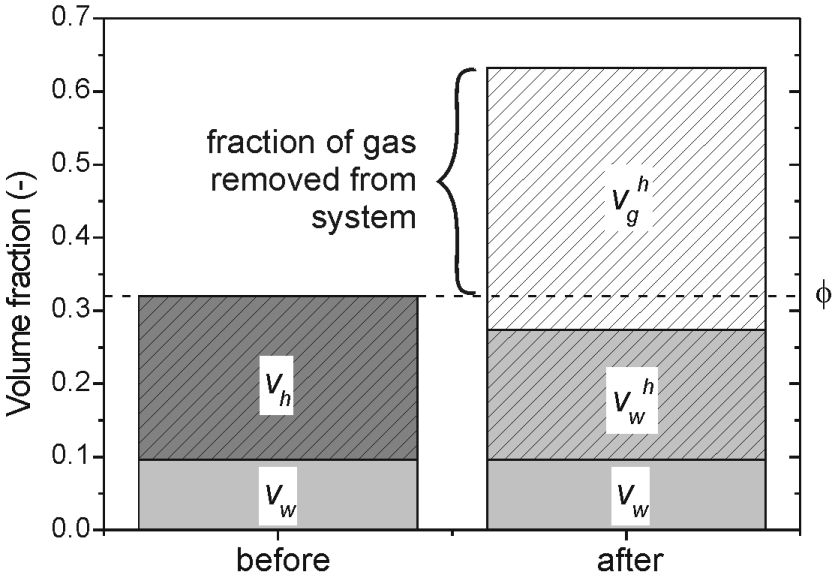

Figure 5.1.: Volumetric balance of phases within the pore space before and after gas hydrate decomposition for a model sediment with $\phi = 0.32$ and $S_h = 0.70$. v_w: volume of water; v_h: volume of hydrate; v_w^h: volume of water generated from hydrate; v_m^h: volume of methane gas generated from hydrate.

purpose of this study, a simplified model was taken as a basis, where constant pressure and volume are maintained during the destabilization of gas hydrate (Section 6.2). It was assumed, that one part of the generated methane gas would balance the volumetric difference between the hydrate and the generated water, and that the remaining part of methane gas was removed from the system, either by injection into the surrounding formation or by leakage through cement annulus of the borehole. The relative amount of methane gas retained in the sediment amounts to about 13 % of the total volume of methane originally stored in the hydrate, which can be calculated from:

$$V_m^* = \frac{1 - V_w^h}{V_m^h} \tag{5.6}$$

As a result, after hydrate decomposition a partially gas and water saturated sediment would be generated. For the model sediment considered above, a partial water saturation of 0.85 can be calculated from:

$$S_w^* = \frac{v_w + v_w^h}{\phi} \tag{5.7}$$

5.3. Stability Conditions for Methane Hydrate at Mallik

The most important factors influencing natural gas hydrate stability are:

- pressure
- temperature
- composition of fluid phase
- composition of gas phase
- porous medium structure (grain size etc.)

For the set-up of the numerical model in the current study, a detailed consideration of the effects of the composition of the fluid and gaseous phases was required. A review of the available data and methods used to calculate stability conditions, ranging from curve fitting techniques with experimental data to the use of theoretical computer models, can be found in *Peltzer and Brewer* (2000). Within the current study, the computer code CSMHYD (*Sloan*, 1998) was used to predict hydrate equilibria for various pressure and temperature conditions, as well as variations of the fluid and gas phase composition.

5.3.1. Formation Pressure

In order to determine the prevailing gas hydrate stability conditions within a certain depth below ground surface, it is necessary to determine the subsurface pressure conditions. Within the shallow sedimentary environments in which natural gas hydrate occurrences are most frequently known to occur, commonly a hydrostatic pressure gradient is assumed (e.g. *Collett*, 1993). In the Mackenzie Delta area, overpressured zones are commonly observed only at depths greater than 3000 m (*Majorowicz and Osadetz*, 2001).

The absolute hydrostatic pressure within a water column at a certain depth can generally be calculated from:

$$P = P_0 + \rho_w g h \tag{5.8}$$

where

$$\rho_w g = \frac{dP}{dz} \tag{5.9}$$

and
P : Pressure (Pa)
P_0 : Atmospheric pressure (Pa)
ρ_w : Fluid density (kg m^{-3})
g : Acceleration of gravity (m s^{-2})
h : Height of water column (m)
$\frac{dP}{dz}$: Pressure gradient (Pa m^{-1})

Many studies of the gas hydrate stability zone in the Mackenzie Delta area (*Dallimore and Collett*, 1999) and the adjacent North Slope of Alaska area (*Collett*, 1993) assume a constant hydrostatic pressure gradient of 9.795 kPa m^{-1}. A precise calculation has to

take into account the effect of the content of dissolved solids on fluid density, as well as density changes with depth resulting from the increase of pressure and the compressibility of water. Furthermore the acceleration of gravity depends on the geographic location of the site under investigation.

Fofonoff and Millard (1982) have compiled algorithms for the calculation of fundamental properties of seawater, including precise pressure to depth conversions considering the effects mentioned above. For average sea water with a salinity of 35 ppt, a depth of 988.19 m is tabulated for a pressure of 10 MPa. This value is given for a latitude of 60 degrees, which is close to the geographic location of the Mallik site at 69° 27' 39.302" N and 134° 39' 38.898" W (Mallik 5L-38 well). For the purpose of this study, this value was converted to a pressure gradient of 10.12 kPa m^{-1} which was chosen as the representative value for the depth interval of the observed gas hydrate occurrences at Mallik. This value is close to the average reservoir pressure gradient value of 10.31 kPa m^{-1}, which can be calculated from the results of the pressure transient analysis of the MDT tests performed within selected intervals of the Mallik 5L-38 well (*Hancock et al.*, 2005b).

The pressure at the base of the gas hydrate occurrences, which at the Mallik 5L-38 well was determined at 1107 mKB (Section 2.4), was calculated according to Equations 5.8 and 5.9 as:

$$P = 101.3\ kPa + \left[10.12\ kPa\ m^{-1} \cdot (1107\ mKB - 5.6\ m)\right] = 11247\ kPa \qquad (5.10)$$

5.3.2. Salinity of Pore Water

Numerous experiments have shown the influence of salinity on gas hydrate stability. For a given pressure, the stability temperature of methane hydrate is depressed by the presence of dissolved salts. For seawater of 33.5 ppt salinity, *Dickens and Quinby-Hunt* (1994) measured a depression of the stability temperature of about -1.1 °C compared to pure water in the pressure range between 2.75 MPa to 10.0 MPa.

On the other hand, hydrates exclude all ions during formation (*Sloan*, 1998). The mixing of water generated from hydrate decomposition results in a freshening of the surrounding saline pore water. Low chlorine concentrations are therefore traditionally regarded as indicators for gas hydrate occurrences.

Analysis of the interstitial waters extracted from the Mallik 5L-38 well cores (*Matsumoto et al.*, 2005) showed, that the average salinity in the hydrate-free sand and silt layers (36.7 ppt and 32.0 ppt respectively, *Winters et al.*, 2005) was approximately equal to seawater conditions. Opposed to this, the average salinity in the hydrate-bearing pebble and sand layers was significantly lower (15.2 ppt and 14.2 ppt respectively, *Winters et al.*, 2005), which is interpreted as the effect of dilution by the fresh water generated from the decomposition of hydrate (*Matsumoto et al.*, 2005).

For the set-up of the model it was assumed, that the in-situ salinity of the pore water prior to hydrate decomposition was equal to an average seawater salinity of 35 ppt. During hydrate decomposition the stability threshold was assumed to shift towards higher temperatures due to the freshening effect of the water generated from hydrate decomposition. Assuming that a complete mixing of the original pore water and the

Table 5.2.: Average composition of gas generated from decomposition of six hydrate-bearing sediment samples from the Mallik 5L-38 well (data from *Wiersberg et al.*, 2005).

Compound	CH_4 (vol %)	C_2H_6 (ppmv)	C_3H_8 (ppmv)	C_4H_{10} (ppmv)	CO_2 (vol %)
Concentration	99.69	1225	85.5	440	0.19

water generated by hydrate decomposition is achieved, the change of pore water salinity can be calculated from:

$$S^* = S\frac{v_w}{(V_w^h v_h) + v_w} \tag{5.11}$$

where S^* : Salinity after hydrate decomposition (ppt)
S : Initial in-situ salinity (ppt)
v_w: Ratio of water volume to total volume of rock (-)
v_h: Ratio of hydrate volume to total volume of rock (-)
V_w^h : Volume of water generated from unit volume of hydrate (-)

For the hydrate-bearing layer considered in the model ($\phi = 0.32$, $S_h = 0.70$), a reduction of the initial salinity of 35 ppt to 13 ppt after complete decomposition of the contained hydrate was calculated, with $V_w^h = 0.79$ (Section 5.2). The reduced salinity of 13 ppt correlates well with the average measured salinity of the previously hydrate-bearing core samples from the Mallik 5L-38 well (see above).

5.3.3. Gas Phase Composition

The gas phase composition can have a severe influence on crystallographic structure and the stability threshold of gas hydrates. The gas hydrates occurring at Mallik, like at many other known gas hydrate sites worldwide, are predominantly composed of methane. *Bily and Dick* (1974) reported methane concentrations of 99.19 % to 99.53 % in the gas recovered during drill-stem tests of hydrate-bearing intervals of the Mallik L-38 well. The presence of other gases than methane results in an increase of the stability temperature (*Holder and Hand*, 1982).

Wiersberg et al. (2005) measured the composition of the gas generated from decomposition of six hydrate-bearing sediment samples from the Mallik 5L-38 well. The average methane content was greater than 99.5 % (Table 5.2). As will be shown later (Section 5.4), the relatively small concentration of other gases than methane has only a negligible effect on the gas hydrate stability threshold (Section 5.4).

5.4. Stability Zone for Methane Hydrate at Mallik

Stability curves for different pore water salinities are displayed in Figure 5.2. Table 5.3 lists the stability temperatures for different pore water salinities and gas compositions at the base of the gas hydrate occurrences at 1107 mKB calculated by CSMHYD,

Table 5.3.: Equilibrium temperatures for methane hydrate calculated with CSMHYD (*Sloan*, 1998) for a pressure of 11.25 MPa. [a]: average Mallik gas composition (99.69 vol% CH_4, 0.08 vol% C_2H_6, 0.01 vol% C_3H_8, 0.03 vol% C_4H_{10}, 0.19 vol% CO_2), [b]: drilling mud salinity (20 ppt NaCl, 76 ppt KCl).

Salinity (ppt)	Equilibrium temperature (°C)
0	14.53
13	13.96
35	12.97
35	13.01[a]
96[b]	10.78

assuming a hydrostatic pressure of 11.25 MPa (Section 5.3.1). For all conditions listed, a structure I hydrate was predicted by the calculations.

At the base of the gas hydrate occurrences an equilibrium temperature of 12.3 °C was measured (Chapter 3, Table 3.7). This temperature is about 0.7 K below the calculated stability threshold for a pure methane hydrate and a salinity of 35 ppt (Table 5.3). Under the considered conditions the boundary of the stability zone for methane hydrate would occur some tens of meters below the observed base of the gas hydrate occurrences at Mallik. The boundary of the stability zone is marked by the intersection of the respective stability curve with the ground temperature profile (Figure 5.2), which for the Mallik 3L-38 well occurs at 1144.3 mKB.

The calculations furthermore predict the following influence of the pore water salinity on the stability temperatures: Compared to a salinity of 35 ppt the stability temperature in equilibrium with fresh water is increased by 1.5 K. A change of salinity from 35 ppt to an intermediate value of 13 ppt, which was calculated on the basis of volumetric considerations (Section 5.3.2), would increase the equilibrium temperature about 1 K. The highly saline KCl drilling mud (96 ppt) would reduce the equilibrium temperature at the base of the hydrate occurrences to 10.78 °C. As a result, the in-situ pressure-temperature conditions within the lower 60 m of the gas hydrate occurrences would fall outside the thermodynamic stability region (Figure 5.2). This effect was nevertheless not considered because during the drilling and circulation period, the stability of hydrate in direct contact with the drilling mud would have been still maintained because of the low temperature of the drilling mud of about 5 °C (Section 6.4.2). Moreover invasion of the saline drilling mud into the formation is considered to be negligible, because of the low permeability of the hydrate-saturated sediments (*Hancock et al.*, 2005b).

While the expected changes in salinity exert a significant effect on the stability threshold, the predicted effect of the presence of small amounts of other gases than CH_4 is negligible (Table 5.3).

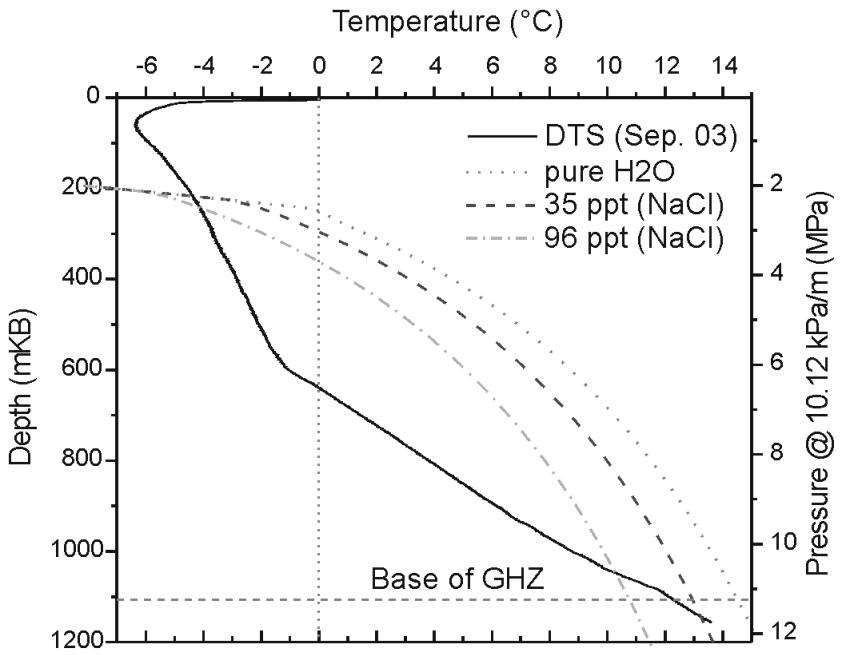

Figure 5.2.: Stability diagram for methane hydrate at Mallik for different pore water salinities. DTS (Sep.03): Near-equilibrium DTS temperature profile of the Mallik 3L-38 well measured in September 2003. Methane hydrate equilibria were calculated with CSMHYD (*Sloan*, 1998) for the given NaCl concentrations. GHZ: observed gas hydrate zone.

6. Numerical Simulation of the Temperature Effect of Phase Transitions

6.1. Simulation Scenarios

The transient calculations were set up to reproduce the thermal effects of the drilling and construction of the Mallik 3L-38 well on the natural geothermal field at the base of the gas hydrate occurrences and the subsequent temperature recovery until the September 2003 DTS temperature survey. A number of different simulations was performed in order to quantify the influence of particular model parameters and loads on the transient temperature field (Table 6.1).

Scenario A is the base case of the performed simulations. It includes the model parameters described in Section 6.3.3 and boundary conditions listed in Table 6.4. In contrast to the other scenarios, Scenario A includes a reversible phase transition, i.e. gas hydrate can both be decomposed and formed within equivalent stability thresholds. The scenarios B1, B2, and B3 consider inhibited regeneration of gas hydrate during the temperature recovery period, with further changes in respect to the assumed stability range (B2) and temperature of the cement during pumping (B3).

6.2. The Stefan Problem and the Enthalpy Method

The classical mathematical model for heat flow calculations involving a phase transition is known as the *Stefan Problem* (*Stefan*, 1891). It was formulated under certain simplifying assumptions considering melting and solidification processes.

The thermodynamic quantity enthalpy is the thermal energy absorbed by a material during a change of temperature under constant pressure. Assuming constant pressure and volume, the change of enthalpy accompanying a certain temperature change is equal to the change of the internal energy (e.g. *Alexiades and Solomon*, 1993):

Table 6.1.: Description of simulation scenarios.

Scenario	Description
A	Base case with reversible phase transition
B1	Similar to Scenario A, inhibited hydrate regeneration
B2	Similar to Scenario B1, stability interval 13-13.5 °C
B3	Similar to Scenario B2, cement temperature 20 °C

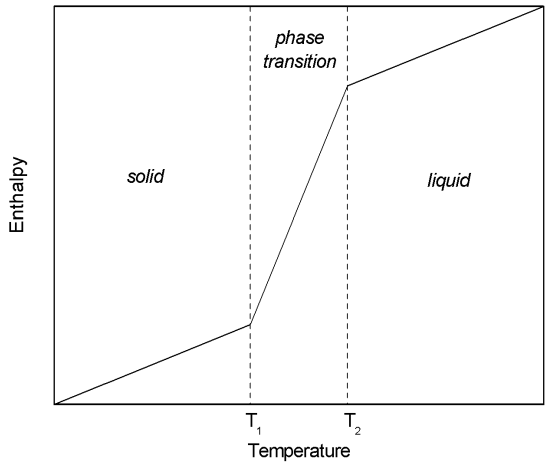

Figure 6.1.: Schematic enthalpy-temperature curve for the enthalpy model. T_1, T_2: lower and upper temperature limit of phase transition interval.

$$\Delta H = L + V \int \rho c_{(T)} dT \tag{6.1}$$

where ΔH : Enthalpy change (J m^{-3})
L : Latent heat of phase transition (J m^{-3})
V : Volume (m^3)
ρ : Density (kg m^{-3})
$c_{(T)}$: Specific heat capacity (J kg^{-1} K^{-1})

Figure 6.1 shows a schematic plot of such an enthalpy-temperature relationship. Above and below the phase transition temperature (or temperature range), the slope of the enthalpy curve is equal to the respective volumetric heat capacity of the material, in either solid or liquid state. Within the temperature range where the phase transition is occurring (denoted as T_1 and T_2), the mobilization of latent heat results in a step of the enthalpy curve.

Within numerical modelling, the thermal effects resulting from phase transitions can be included by defining material parameters as non-linear functions of temperature. Formulations can be based on the use of an apparent specific heat or the use of enthalpy. Within this study, the multi-purpose finite element code ANSYS 8.1 was used, in which both of these formulations are implemented. The enthalpy method was chosen, because it is less prone to difficulties resulting from 'lost' latent heat during the phase change process and is therefore less sensitive to time step size and mesh density (*Dantzig*, 1989).

In the strict sense, the basic assumptions for the classical solution of the Stefan Problem, constancy of pressure and volume, are violated, considering the volumetric balance of the methane hydrate decomposition process discussed in Section 5.1. Therefore for the purpose of this study a simplified model for the destabilization of gas hydrate was

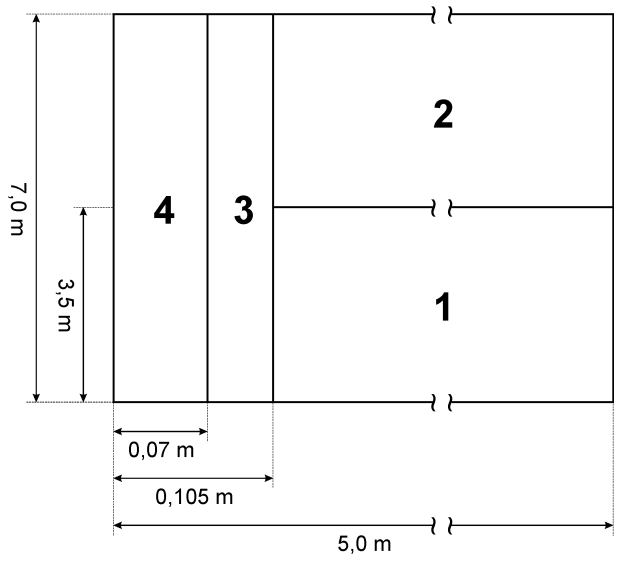

Figure 6.2.: Schematic diagram of the 2D-axisymmetric model domain (not to scale). The cartesian x-axis corresponds to the radial direction (r), with the axis of symmetry at $r = 0$. The cartesian y-axis corresponds to the axial direction (z). 1: non-hydrate-bearing layer, 2: hydrate-bearing layer, 3: cement annulus, 4: fluid-filled borehole casing.

set up, assuming that constant volume and pressure were maintained by the removal of excess methane gas from the system (Section 5.1). The error introduced by this assumption with reference to the energy balance is relatively small, considering the low specific heat capacity of methane gas, which is several orders of magnitude lower than that of the other involved materials.

6.3. Set-up of the Numerical Model

6.3.1. Model Geometry

For the simulation of the temperature field in the vicinity of the borehole a simplified 2D vertical cross section model with axial symmetry was set up. Figure 6.2 shows the geometry of the model domain. The model domain primarily contains two horizontal layers at the contact between the hydrate-free unit below the base of the observed gas hydrate occurrences and the overlying lowermost hydrate-bearing unit, respectively referred to as layer 1 and layer 2 further in the text.

The vertical extent of the model domain of 7 m was chosen according to the extent of the observed temperature anomaly at the base of the hydrate occurrences (see Section 3.5.1 and Section 3.5). The radial extent of the model domain was set to 5 m, such that a constant temperature boundary condition corresponding to undisturbed conditions could be placed here without introducing a significant error in the calculated temperature field near the borehole.

The interior of the borehole with a nominal diameter of 200 mm (7-7/8 in) was

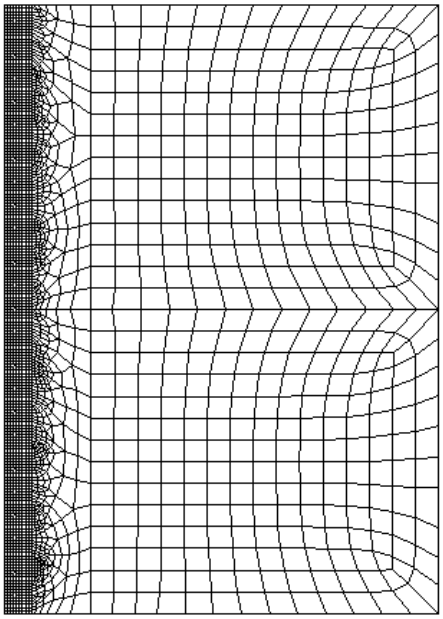

Figure 6.3.: Finite element model mesh. The mesh size increases from 0.035 m at $r = 0$ in the near vicinity of the borehole to about 0.35 m at the outer model boundary at $r = 5\ m$.

explicitly included in the numerical model (Figure 6.2). Because the caliper logs of the adjacent Mallik 5L-38 well had indicated a near-gauge hole in the hydrate-bearing units below the permafrost base, only a small enlargement of the borehole diameter of 5 % corresponding to a total radius of 0.105 m was assumed. The borehole domain is subdivided into an area representing the fluid-filled well casing with a diameter of 0.07 m (5-1/2 in) and a second area representing the cement annulus between the well casing and the borehole wall.

6.3.2. Finite Element Mesh

The influence of the drilling and cementing operations was simulated by specifying corresponding temperatures and heat generation rates inside the borehole (Section 6.4). Because of the temperature difference to the surrounding formation, high temperature gradients occur in the near vicinity of the borehole, requiring small element sizes of the model mesh within this area (Figure 6.3). The mesh was refined with equally sized quadratic elements of 0.035 m edge length within the borehole domain and extending to a radial distance of 0.315 m. With increasing distance from the borehole axis a coarser mesh was used in order to minimize the computational effort required to run the model. Therefore the remaining part of the model domain was meshed using the built-in mesh tool of ANSYS and constraining the element edge sizes at $r = 1\ m$ to 0.25 m.

Table 6.2.: Thermal input parameters for the materials defined in the numerical model. λ: thermal conductivity, c: specific heat capacity, ρ: density, S_h: hydrate saturation.

Material	λ (W m^{-1} K^{-1})	c (J kg^{-1} K^{-1})	ρ (kg m^{-3})
Formation, $S_h = 0.0$	2.88	1834	2127
Formation, $S_h = 0.7$	2.71	1274	2107
Formation, after decomp.	2.75	1640	2084
Cement	0.48	840	1800
Borehole fluid	0.60	4192	1000

Table 6.3.: Non-linear material model for hydrate-bearing sediment. H: enthalpy, λ: thermal conductivity.

Temperature (°C)	H (J m^{-3})	λ (W m^{-1} K^{-1})
0	0.00E+00	2.71
13	3.49E+07	2.71
14.5	6.76E+07	2.75
30	1.205E+08	2.75

6.3.3. Thermal Parameters

The thermal parameters of the materials defined in the numerical model are listed in Table 6.2. They were calculated from the average lithological composition in the depth interval between 1085 mKB and 1130 mKB, which was derived from the evaluation of the well logs of the Mallik 5L-38 well (Chapter 4). From the well-log data, an average shale content of 12 %, and an average porosity of 32 % was derived for the corresponding interval. The effective thermal conductivity was calculated using the geometric mean model (Section 4.3), effective values for specific heat capacity and density were calculated as the weighted arithmetic mean of the particular components.

The cement properties were deduced from specifications of the service company (BJ Services) provided by the well operator (JAPEX), the properties of the borehole fluid were chosen as for pure water at 10 °C.

The properties of the hydrate-bearing unit were calculated for 70 % hydrate saturation, which was chosen as a representative value for the base of the gas hydrate occurrences (Figure B.5). In order to include the thermal effect of phase changes in the hydrate-bearing layer, a non-linear material model was used (Table 6.3).

The data for the non-linear material model listed in Table 6.3 was calculated for a phase transition occurring between 13 °C and 14.5 °C using Equation 6.1. The phase transition interval corresponds to a shift of the stability conditions for a salinity change from 35 ppt to fresh water (Section 5.3). The latent heat of phase transition makes up the main part of the enthalpy change within the phase transition interval. It amounts to $2.81 \cdot 10^7$ J m^{-3}, assuming $\phi = 0.32$, $S_h = 0.70$, and the calorimetric properties of methane hydrate listed in Table 5.1:

$$L = L_h \rho_h \phi S_h \tag{6.2}$$

where L : Latent heat of phase transition per volume of porous medium (J m^{-3})
L_h : Latent heat of phase transition of methane hydrate (J kg^{-1})
ρ_h : Density of pure methane hydrate (kg m^{-3})
ϕ : Porosity (-)
S_h : Methane hydrate saturation (-)

Apart from the enthalpy, a change of thermal conductivity was also included in the non-linear material model. This enables to take into account the change of the bulk rock thermal conductivity caused by the phase transitions. After hydrate decomposition, the formation properties were calculated for a partial water / methane gas saturation of 0.85 (Section 5.1) using the following set of equations from the method developed by *Johansen* (1975):

$$\lambda = (\lambda_{sat} - \lambda_{dry}) K_e + \lambda_{dry} \tag{6.3}$$

$$\lambda_{dry} = \frac{0.135 \rho_{dry} + 64.7}{2650 - 0.947 \rho_{dry}} \tag{6.4}$$

$$K_e = 0.7 \log S_w + 1.0 \tag{6.5}$$

where λ_{sat} : Thermal conductivity at 100 % saturation (W m^{-1} K^{-1})
λ_{dry} : Dry thermal conductivity (W m^{-1} K^{-1})
K_e : Kersten's number (-)
ρ_{dry} : Dry density (kg m^{-3})
S_w : Water saturation (-)

The partial water saturation of 0.85 after hydrate decomposition was calculated using Equation 5.7, assuming that the generated methane gas would balance the volumetric difference between the hydrate and the water produced, and that the excess methane gas was removed from the system (Section 5.1). In contrast to the change in enthalpy caused by the phase transition, the change of the sediment from hydrate-bearing to partial gas/water saturation has only a very limited effect on the static thermal parameters under the above stated assumptions (Table 6.2).

6.4. Boundary Conditions and Discretization of Time

6.4.1. Loadsteps and time stepping

The simulation period was divided into 10 loadsteps (LS), for each of which different exterior forces or loads were applied to the model (Table 6.4). Loadsteps 1 to 6 reproduce the effects of circulation during the drilling of the well, loadsteps 7 and 8 the pumping and setting of the cement, and loadsteps 9 and 10 include the temperature recovery after cessation of the drilling and cementing operations up to the time of the September 2003 DTS temperature survey.

The total simulation period covers a time span of approximately 21 months. In order to include the effects of short-lived operations with stepped boundary conditions during the drilling and cementing of the well, the length of time steps for loadsteps 1 to 8 was chosen between 300 s and 3600 s. For the subsequent long-term recovery, the maximum time step length was increased to $3 \cdot 10^6$ s. The length of individual time steps was determined through the simulation program under consideration of the calculated heat budget (automatic time stepping).

The initial conditions were calculated performing a steady-state calculation (LS 0) with a constant heat flow of 55 mW m^2 specified at the upper and lower boundary of model domain, representing the natural heat flow (an imaginary time step size of $1 \cdot 10^{-6}$ s was assigned to LS 0 because of requirements specific to the simulation program). The specified flux boundary conditions were kept constant for the entire simulation period, and a constant temperature equal to the undisturbed initial conditions was assigned to the lateral model boundary.

6.4.2. Thermal Effects of Drilling and Cementing

Based on the available drilling reports (Appendix C), appropriate boundary conditions for the drilling, mud-circulation and cementing operations were specified. During the circulation periods (LS 1, 3, and 5), a constant temperature of 5 °C was specified for the elements representing the interior of the well (Section 6.3.1). The temperature of 5 °C was determined as the average of the injection and return temperatures at the wellhead recorded by the service company during the time when the base of the hydrate occurrences was penetrated (Figure C.1).

The cementing of the well is divided in two periods: During the first period (LS 7), which represents the pumping of the cement, a constant temperature of 15 °C was specified in the base case scenario for the elements representing the interior of the well (Scenario B3: 20 °C). According to personal communication with the cementing service company (BJ Services), the cement was mixed and pumped into the well with temperatures between 10 °C and 20 °C.

During the setting of cement latent heat of hydration is released. For the Mallik wells, a special type of cement (Cold Set II) with low heat generation developed for permafrost wells was used. Based on the properties of the cement (given in brackets below), a heat generation rate of 6700 W m^{-3} was specified as a boundary condition in loadstep 8, which was calculated from:

$$HGEN = \frac{L_{cmt}\rho}{\Delta t} \tag{6.6}$$

where $HGEN$: Heat generation rate (W m^{-3})
L_{cmt}: Latent heat of hydration of cement slurry (=$67 \cdot 10^3$ J kg^{-1})
ρ_{cmt}: Density of cement slurry (=1,800 kg m^{-3})
Δt: Time required for setting of cement slurry (=18,000 s)

Table 6.4.: Loadsteps (LS) and applied boundary conditions for base case Scenario A. TIME: total simulation time at end of loadstep, TEMP: constant temperature boundary condition, HGEN: heat generation rate boundary condition.

LS	Operation	Begin	Duration (hrs)	TIME (days)	Load
0	(Steady state initial condition)	Jan. 05, 2002 01:00	0.0	0.0	-
1	Drilling and circulation	Jan. 05, 2002 01:00	6.0	0.3	TEMP = 5 °C
2	Shut-in	Jan. 05, 2002 07:00	11.0	0.7	-
3	Drilling and circulation	Jan. 05, 2002 18:00	3.5	0.9	TEMP = 5 °C
4	Shut-in	Jan. 05, 2002 21:30	2.5	1.0	-
5	Drilling and circulation	Jan. 06, 2002 00:00	2.5	1.1	TEMP = 5 °C
6	Shut-in	Jan. 06, 2002 02:30	25.0	2.1	-
7	Pumping of cement	Jan. 07, 2002 03:30	2.0	2.2	TEMP = 15 °C
8	Setting of cement	Jan. 07, 2002 05:30	5.0	2.4	HGEN = 6700 W m^{-3}
9	Recovery (first recorded DTS profile)	Jan. 07, 2002 10:30	86.1	6.0	-
10	Recovery (last recorded DTS profile)	Jan. 11, 2002 00:37	14834.9	624.1	-

6.5. Modelling Results

6.5.1. Simulations with reversible phase transition (Scenario A)

Scenario A considers a reversible phase transition for layer 2. As a result of the non-linear material model assigned to layer 2 (Section 6.3.3), latent heat of phase transition is consumed during an increase of temperature above the lower limit of the stability interval. Moreover, assuming a reversible phase transition, during a decrease of temperature within the phase transition interval latent heat is again released, which would be equivalent to the regeneration of hydrate from the previously released methane gas and water.

The thermal effect of this reversible phase transition process is displayed by the time-history plots of the calculated temperatures at different distances from the borehole (Figure 6.4). At the end of the drilling and cementing operations (LS 8, 2.4 d) the temperature increase in layer 2 is attenuated by the consumption of latent heat during the increase of temperature above the stability limit. As a result, the temperature in the near vicinity of the borehole in layer 2 is lower than the temperature in layer 1 during loadstep 8 and the subsequent beginning of the temperature recovery period (Figure E.1).

As soon as the local temperature has returned to a value within the phase transition interval, the phase transition process is reversed and the temperature recovery in layer 2 is attenuated by the release of latent heat. As a result, the temperature of layer 1 falls below the temperature in layer 2, which is marked by the cross-cutting of the temperature curves in Figure 6.4. For some time of the following temperature recovery period, the temperature in layer 1 now lies below the temperature in layer 2. After the local temperature has again dropped below the stability threshold, no further latent heat is released and the temperature recovery in layer 2 is progressing at a faster pace. This process continues until at later times during the recovery period the temperature in layer 2 again drops below the temperature in layer 1 and the original temperature field is recovered (Figure D.1).

Axial profiles of calculated temperatures and the corresponding anomalies of the temperature gradients during the temperature recovery period are displayed in Figure 6.5. The selected points in time are approximately equal to the shut-in times of the measured DTS temperature profiles which had been analyzed in Section 3.5.1 and Section 3.5. The displayed temperature profiles are characterized by the attenuated temperature recovery in layer 2, which is triggered by the release of latent heat during the regeneration of hydrate considered in Scenario A. As a result of the attenuated decay of the temperature disturbance, a *negative* temperature step, i.e. with a negative temperature gradient anomaly, has developed during intermediate shut-in times at the interface between layer 1 and layer 2. The calculated temperature gradient exhibits a relatively large negative anomaly with a maximum value of -46 K km^{-1} (Figure 6.5, b, Table 6.5).

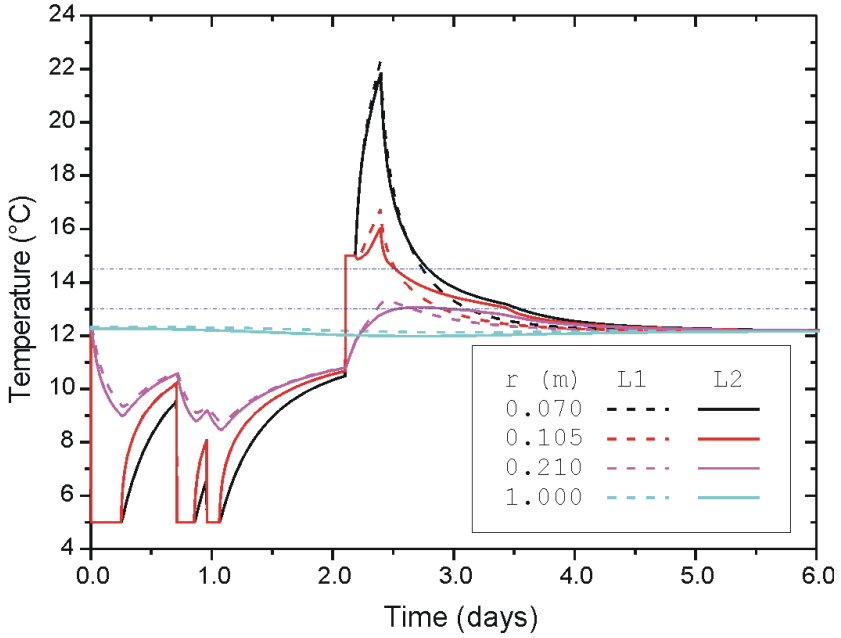

Figure 6.4.: Time-history plot of calculated temperatures, reversible phase transition (Scenario A), loadsteps 1-9. L1: $z = 1.75$ m, L2: $z = 3.25$ m. r = 0.07 m: borehole casing, r = 0.105 m: borehole wall, r = 0.21 m and 1.0 m: formation. Dash-dot lines: phase transition interval.

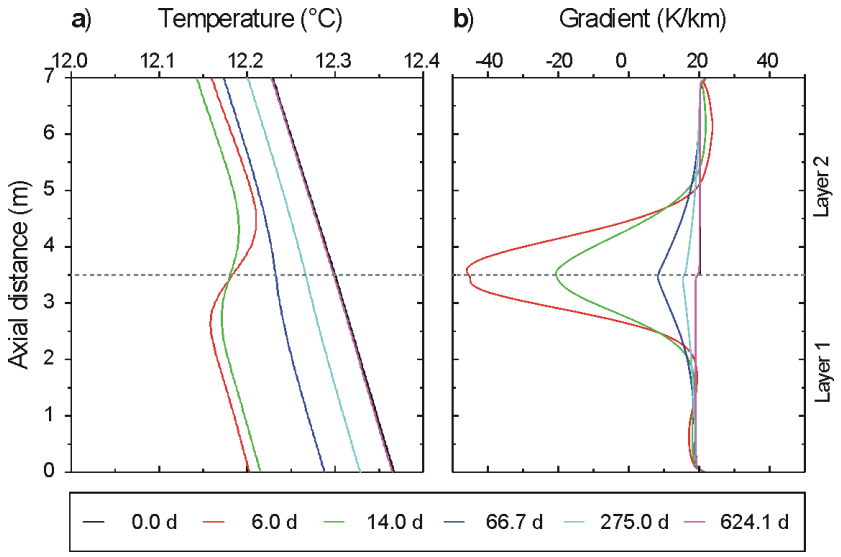

Figure 6.5.: Calculated axial temperature profiles (a) and temperature gradients (b) during temperature recovery period at r = 0.07 m, reversible phase transition (Scenario A). Time given as total simulation time (days).

Table 6.5.: Simulated temperature gradient anomalies at the end of loadstep 9 (TGY_{max} LS9) and temperatures at the borehole wall (r=0.105 m) at the end of loadstep 8 ($TEMP_{max}$). z: axial position of maximum gradient anomaly, ΔTEMP: temperature difference layer 1 (L1) and layer 2 (L2).

Scenario	TGY_{max} LS9 (K km^{-1})	z (m)	$TEMP_{max}$ L1 (°C)	$TEMP_{max}$ L2 (°C)	ΔTEMP (K)
A	-46.0	3.57	16.71	16.01	0.70
B1	34.7	3.01	16.71	16.01	0.70
B2	45.8	3.11	16.71	15.64	1.08
B3	88.6	3.53	18.33	17.27	1.06

6.5.2. Simulations with inhibited hydrate regeneration (Scenario B)

Within Scenario B only the decomposition of hydrate is considered, with no regeneration of hydrate during the temperature recovery period. Within the numerical model a linear material model was assigned to the elements of layer 2 during the temperature recovery period, with the assumed thermal parameters of the formation after hydrate decomposition described in Section 6.3.3.

The development of temperature during the drilling and cementing period of Scenario B is equal to the temperature development in Scenario A. During the increase of temperature above the stability threshold, the increase in temperature in layer 2 is attenuated by the consumption of latent heat. The maximum temperature difference between layer 1 and layer 2 amounts to 0.7 K at the end of the cementing phase (LS 8) (Table 6.5). But in contrast to Scenario A, the sign of the temperature difference between layer 1 and layer 2 which has developed during the cementing phase is maintained during the temperature recovery period (Figure 6.6, Figure E.2). Because within Scenario B no regeneration of hydrate is considered and no latent heat during the return to equilibrium is released, there is no cross-cutting of the temperature curves for layer 1 and layer 2 as in Scenario A (Figure D.2).

During the temperature recovery period, a *positive* temperature step, i.e. with a positive anomaly of the temperature gradient, is prevailing (Figure 6.7). Within Scenario B1, the magnitude of the temperature gradient anomaly amounts to 35 K km^{-1} during the time equivalent to the first DTS measurements. In Scenario B2 the magnitude of the temperature gradient anomaly is increasing to 46 K km^{-1} (Figure 6.8, b), with a further increase to 89 K km^{-1} in Scenario B3 (Figure 6.9, b). The magnitude of the temperature step at the end of the cementing phase (LS 8) increases to about 1.1 K in Scenario B2 and B3 (Table 6.5).

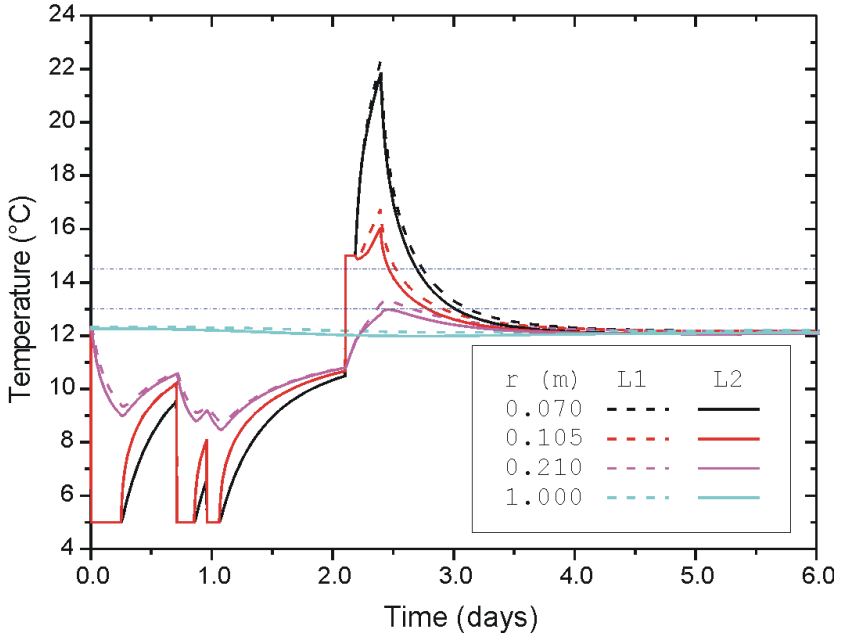

Figure 6.6.: Time-history plot of calculated temperatures, inhibited hydrate regeneration (Scenario B1), loadsteps 1-9. L1: $z = 1.75$ m, L2: $z = 3.25$ m. r = 0.07 m: borehole casing, r = 0.105 m: borehole wall, r = 0.21 m and 1.0 m: formation. Dash-dot lines: phase transition interval.

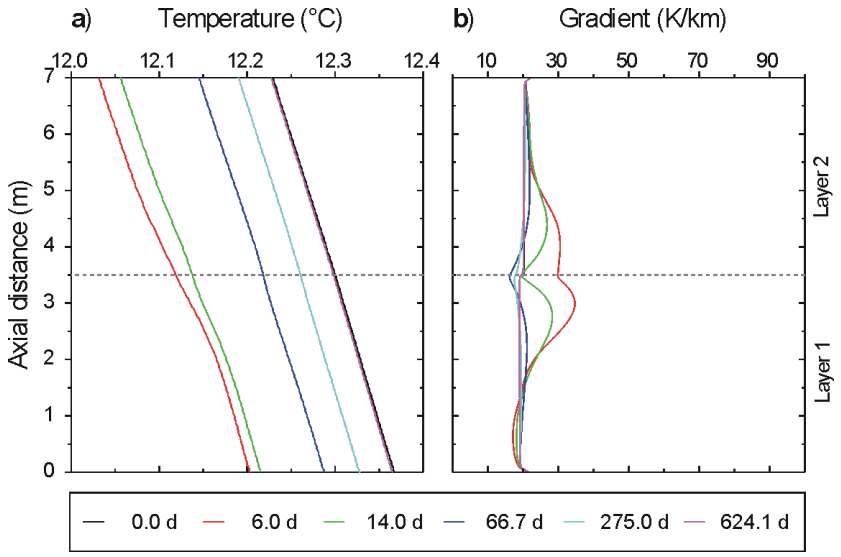

Figure 6.7.: Calculated axial temperature profiles (a) and temperature gradients (b) during temperature recovery period at r = 0.07 m, inhibited hydrate regeneration (Scenario B1). Time given as total simulation time (days).

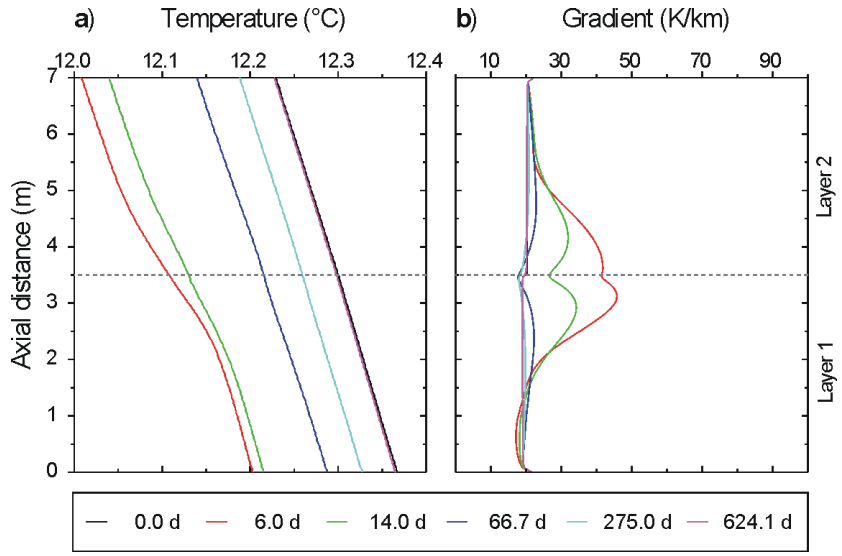

Figure 6.8.: Calculated axial temperature profiles (a) and temperature gradients (b) during temperature recovery period at r = 0.07 m, inhibited hydrate regeneration (Scenario B2). Time given as total simulation time (days).

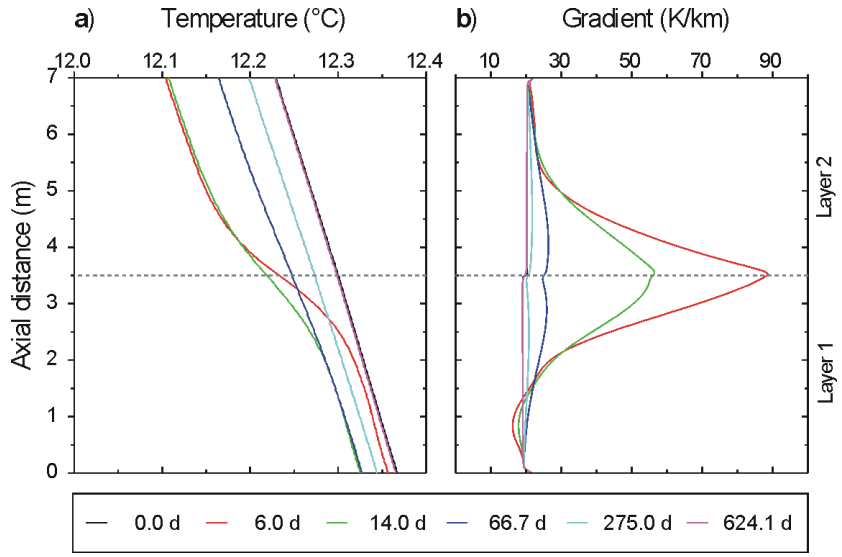

Figure 6.9.: Calculated axial temperature profiles (a) and temperature gradients (b) during temperature recovery period at r = 0.07 m, inhibited hydrate regeneration (Scenario B3). Time given as total simulation time (days).

6.6. Discussion

The change and the magnitude of the relative temperature differences between layer 1 and layer 2 is a good indicator for phase transition processes coupled with a mobilization of latent heat. Especially during the temperature recovery period significant differences between the simulation results of Scenario A and Scenario B exist, elucidating the processes which gave rise to the temperature anomalies observed at Mallik (Section 3.5, Figure 3.19).

The effect of the presence of hydrate on the static effective properties is only resulting in minor differences in the temperature development for layer 1 and layer 2, which can be observed during the drilling and circulation period in the performed simulations. If nevertheless the temperature increases above the hydrate stability threshold and a phase transition is occurring, significant differences resulting from the consumption of latent heat during hydrate decomposition can be observed.

If a reversible phase change is considered (Scenario A), the calculated 'step' of the temperature profiles at the interface between layer 1 and layer 2 is contrary to the measurement results from the Mallik DTS temperature survey. The sign of the anomaly of the calculated temperature gradient is inconsistent with the observed positive temperature gradient anomaly at the base of the gas hydrate occurrences (Figure 3.19). Only if inhibited hydrate regeneration is considered, positive temperature gradient anomalies can be generated for the concerning period of the recovery period. It is therefore concluded, that hydrate regeneration at Mallik is inhibited after the decomposition which had been triggered during the drilling and completion of the wells.

Apart from the fundamental evidence about the process of hydrate regeneration, scenarios B1, B2, and B3 serve to study the factors which influence the magnitude of the temperature anomaly. The observed temperature gradient anomaly has a maximum value of about 109 K km^{-1} (2 m running average temperature gradient, Figure 3.19). With the restriction that the calorimetric properties like the latent heat of phase transition are known from laboratory measurements, the magnitude of the temperature effect depends on the span of the hydrate stability threshold, as well as on the magnitude of the stimulation itself. With a decrease of the span of the stability temperature interval from 1.5 K (Scenario B1) to 0.5 K (Scenario B2), the magnitude of the temperature gradient anomaly is increased about 30 %. An intermediate value for the span of the stability temperature interval of about 1 K would be plausible according to volumetric balance considerations (Section 5.4). The magnitude of the observed temperature anomaly can be approximately reproduced by the model if an upper-limit temperature of the cement during pumping of 20 °C is considered (Scenario B3).

Apart from the positive temperature gradient anomaly considered within the simulations, the measured temperature profiles are characterized by another distinct negative temperature gradient anomaly, which is situated about 15 m above the maximum of the positive anomaly (Figure 3.19). The negative anomaly is interpreted as a result of a combination of different effects, including the temporal duration of the exposure to the drilling process, changes of stability conditions with depth, as well as the local hydrate saturation, which were not considered within the simulations described herein.

7. Summary and Conclusions

The successful completion of the DTS temperature surveys carried out at Mallik has proven, that the DTS technology is well suited for on-line and long-term monitoring of well temperatures, even under the extreme conditions of an arctic environment. With the used DTS system borehole temperatures were measured with an accuracy of ±0.3 °C. The temperature resolution is 0.06 °C for an integration time of 30 minutes and 1 m spacing of data points. Through application of suitable filtering techniques the temperature resolution was increased to values between 0.01 °C to 0.03 °C depending on the measurement processing mode.

The analysis of the disturbed well temperatures after drilling revealed a strong effect of phase transitions on temperature changes (Section 3.5). For the first time a temperature gradient anomaly with a maximum value of up to 109 K km^{-1} was observed at the base of the gas hydrate occurrences, which is attributed to the process of hydrate decomposition at the interface between a hydrate-bearing and a non-hydrate-bearing sediment layer. This effect is similar to the well-known temperature step often observed within wells at the base of the ice-bearing permafrost and is related to the consumption of latent heat during the decomposition of gas hydrate.

The depth to the base of the gas hydrate occurrences determined from the observed temperature gradient anomalies ranges between 1103.4±3.5 m and 1104.4±3.5 m below ground level. The DTS-derived depths of the gas hydrate base at the Mallik 3L-38 and 4L-38 wells present an independent comparative value for the log-derived depths of the other Mallik wells which altogether show a good agreement. The observed temperature gradient anomalies furthermore allowed a more precise determination of the permafrost boundary compared to earlier estimates: The depth to the base of the ice-bearing permafrost increases from 599±3.5 m to 604±3.5 m below ground level in the Mallik 3L-38 and 4L-38 wells respectively.

At the end of the 21-month observation period temperature profiles near to thermal equilibrium with the formation temperature were recorded. An analysis of the Mallik 2002 temperature data using the Horner-plot method with special consideration of latent heat effects has shown, that the September 2003 temperature profiles of the Mallik 3L-38 and 4L-38 wells are within ±0.1 °C of thermal equilibrium. The comparatively short time required to attain temperature equilibrium can be attributed to the short overall drilling and circulation time of about two to four weeks and the careful control of the drilling mud temperature close to the formation temperature.

The September 2003 temperature profiles show a temperature of 12.3 °C at the base of the gas hydrate occurrences. This value is about 0.7 K below the stability temperature predicted by thermodynamic calculations considering a pressure gradient of 10.12 kPa m^{-1} and a sea-water salinity of 35 ppt. Under the stated conditions, the base of the stability zone of methane hydrate would lie at about 1140 m below ground level.

Average geothermal gradients within the zone of the gas hydrate occurrences range between about 20 K km^{-1} and 50 K km^{-1} (Figures 3.14, 3.15 and 3.16). The analysis of the near-equilibrium temperature profiles suggests, that the geothermal gradient is mainly lithologically controlled, and that there is no significant influence of hydrate content on the static temperature field. The lithological units show characteristic thermal signatures which can be related to lithological changes determined from coring and well-log data. The temperature gradient profiles of the three adjacent Mallik 2002 wells (Figure 4.3) show similar patterns, which indicates the stratified nature of the Mallik deposit.

The bulk rock thermal conductivity of the Mallik sediments can quantitatively be estimated by determining the lithological composition from logging data and calculating effective thermal conductivities applying mixing-law models (Sections 4.2 and 4.3). The results of the geometric mean model showed the best agreement to the thermal conductivity profiles derived from geothermal data (Figure 4.4), which were calculated from the measured geothermal gradients and an estimated local heat-flow value of 55 mW m^{-2} (*Majorowicz and Smith*, 1999) based on Fourier's law of heat conduction. It is therefore concluded, that the geometric mean model is generally applicable for estimation of thermal conductivity of the weakly consolidated sediments encountered at Mallik, including strata containing high saturations of disseminated methane hydrate of up to 90 %. Average thermal conductivity values of the sand intervals with high hydrate saturations range between 2.35 W m^{-1} K^{-1} and 2.77 W m^{-1} K^{-1}.

The results of the geometric mean model are in support of the apparently low influence of hydrate saturation on the bulk rock thermal conductivity deduced from the analysis of the geothermal gradients: The geometric mean model predicts a reduction of the bulk rock thermal conductivity of about 10 % for a hydrate-saturated sand with about 35 % porosity compared to water saturated conditions. Variations within this order of magnitude could nevertheless not be determined from the available field data because of lithological heterogeneity and the error associated with the geothermal data. Therefore precision measurements of thermal conductivity on hydrate-bearing sediments under controlled laboratory conditions are recommended.

The good agreement of the thermal conductivity data generated using the two independent methods supports the local estimate of heat flow from *Majorowicz and Smith* (1999). Systematic deviations of the results produced by the different methods can not be observed. This is regarded as strong evidence that the heat flow can be regarded as constant over the investigated depth interval below the permafrost base, and that the predominant process of heat transport is conduction.

The observed temperature step and the related temperature gradient anomaly after drilling can be reproduced with a simplified thermal model of heat conduction considering mobilization of latent heat during phase change (enthalpy method) and assuming constant pressure and volume (Chapter 6). The magnitude of the temperature gradient anomaly is dependent on the latent heat of the phase transition and the stability threshold, which in the considered case mainly depends on the salinity change during hydrate decomposition.

Although after the beginning of the observation period only a small fraction of the initial temperature disturbance had remained, the computed time-histories show similarities to the measured temperature changes with superposition of cooling and warming

phases resulting from the thermal effects of different operations during the drilling and construction of the wells (Section 6.5). The observed positive temperature gradient anomaly can nevertheless only be reproduced with the numerical model assuming inhibited hydrate regeneration after hydrate decomposition (Section 6.6). The processes related to hydrate formation should be investigated within further laboratory studies.

A. Photo Documentation

Figure A.1.: Calibration of DTS system in a temperature controlled chamber at GFZ Potsdam. 20 m of sensor cable from the cable reels are placed in a 100-liter water bath. The temperature of the water bath is measured with a precision platinum resistance thermometer. This calibration procedure results in a high stability of the temperature inside the water bath and allows for long cable sections up to about 100 m inside the bath. Nevertheless a long equilibration period is required until a stable temperature is reached, and the temperature range is limited to -15 °C and 40 °C. Up to two calibration measurements with different temperatures can be performed in 24 hours.

Figure A.2.: The Mallik drilling rig during the thermal stimulation experiment, Mar. 9, 2002.

Figure A.3.: Permanent installation of the fibre-optic DTS cables: The sensor cables were attached with custom-built cable clamps during the installation of the borehole casing, Mallik 3L-38 well, Jan. 6, 2002 (modified from Henninges et al., 2003).

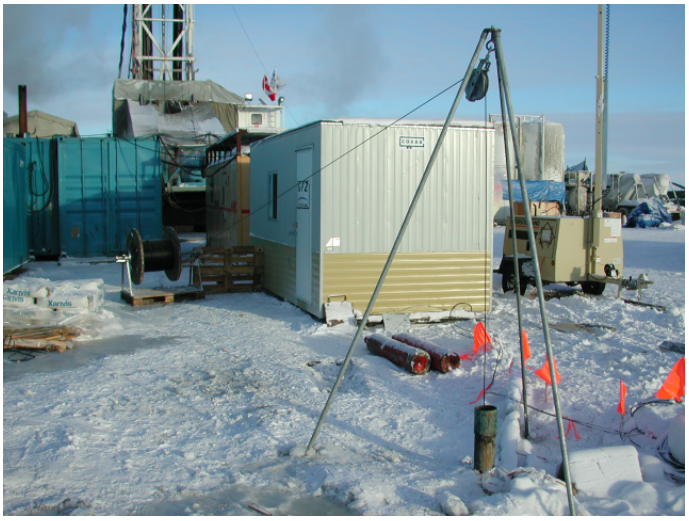

Figure A.4.: Wireline DTS log with combined P/T memory tool, Feb. 18, 2002.

Figure A.5.: Steel box for the protection of the surface ends of the DTS cables on the Mallik 3L-38 well, Mar. 12, 2002.

Figure A.6.: Temporary set-up of the DTS-logging equipment at the flooded and partially frozen Mallik site, Oct. 7, 2002. Foreground: shelter for DTS instrument, background: steel boxes accommodating surface ends of sensor cables (modified from Henninges et al., 2003).

B. Geophysical Well Logs of Mallik 3L-38, 4L-38, and 5L-38

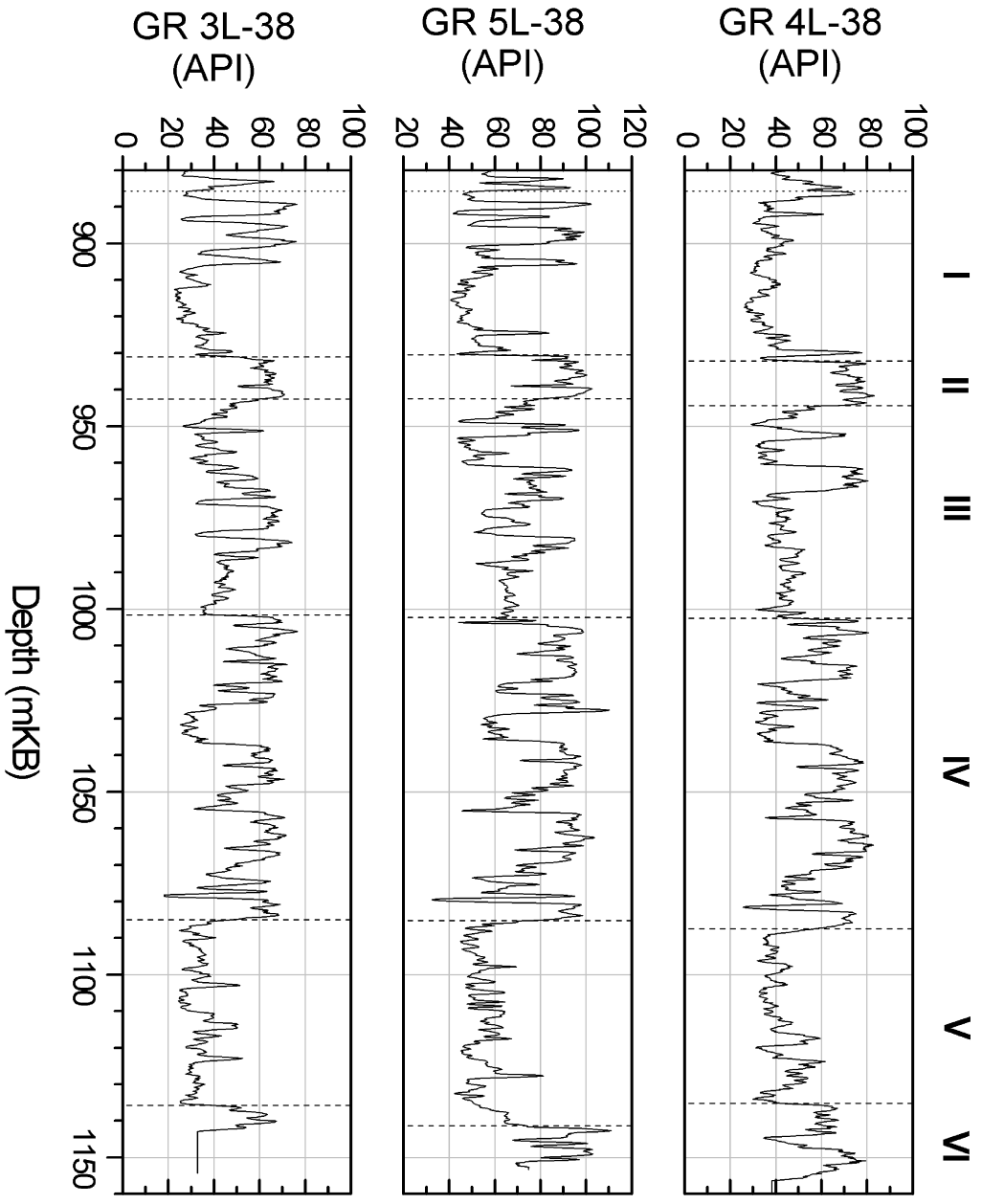

Figure B.1.: Correlation of gamma-ray logs of Mallik 3L-38, 4L-38, and 5L-38 wells. 3L-38 and 4L-38: cased-hole logs. 5L-38: open-hole log. Roman numerals: lithological units adopted from *Medioli et al.* (2005).

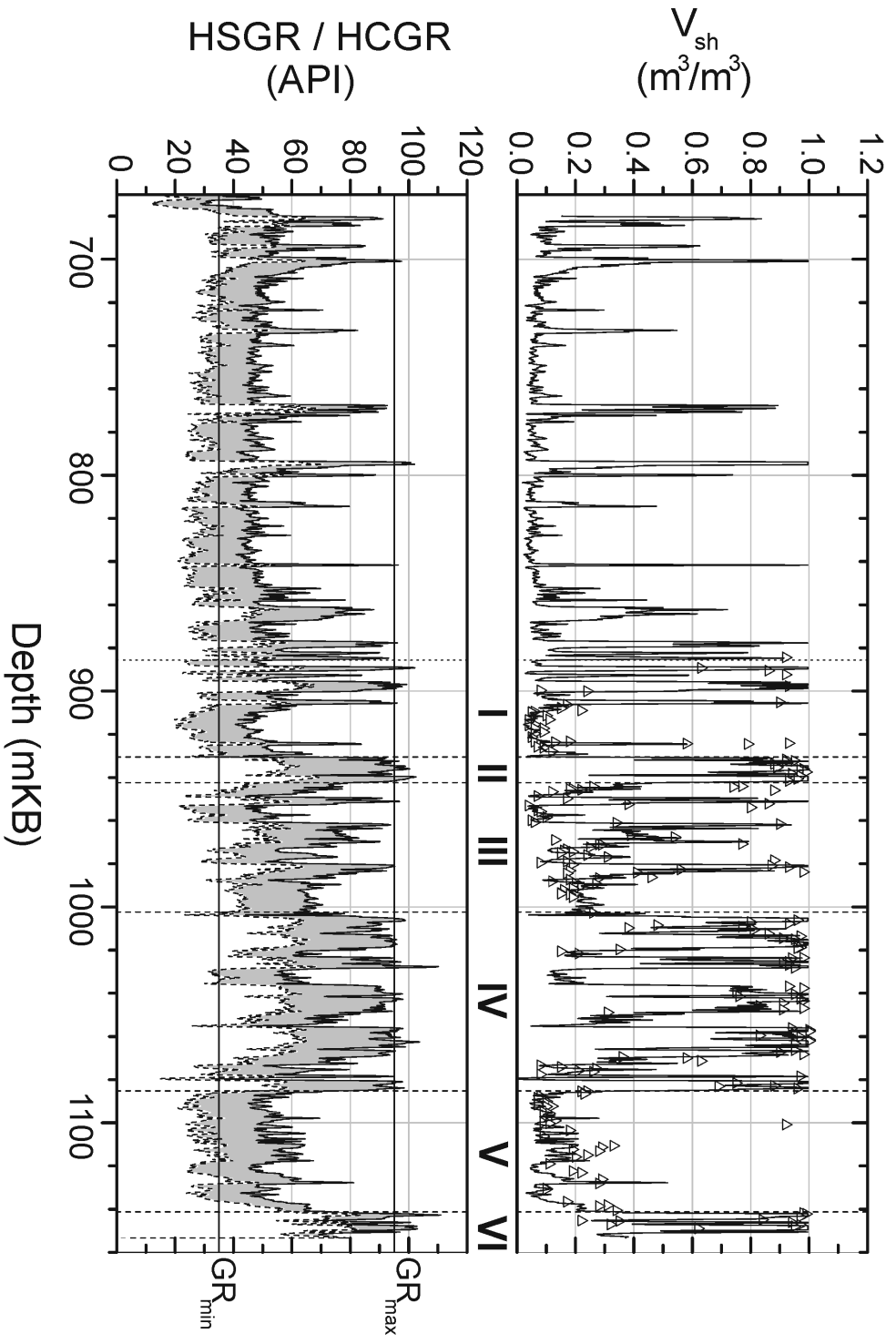

Figure B.2.: Gamma-ray logs and computed shale content. HSGR (solid line): standard gamma ray; HCGR (dashed line): computed gamma ray, corrected for uranium content; V_{sh}: shale volume, calculated from HCGR-log using equation for tertiary unconfined rocks; rectangles: silt fraction (<0.063 mm) from grain-size analyses of Mallik 5L-38 core samples (data from *Medioli et al.*, 2005). Roman numerals: lithological units adopted from *Medioli et al.* (2005).

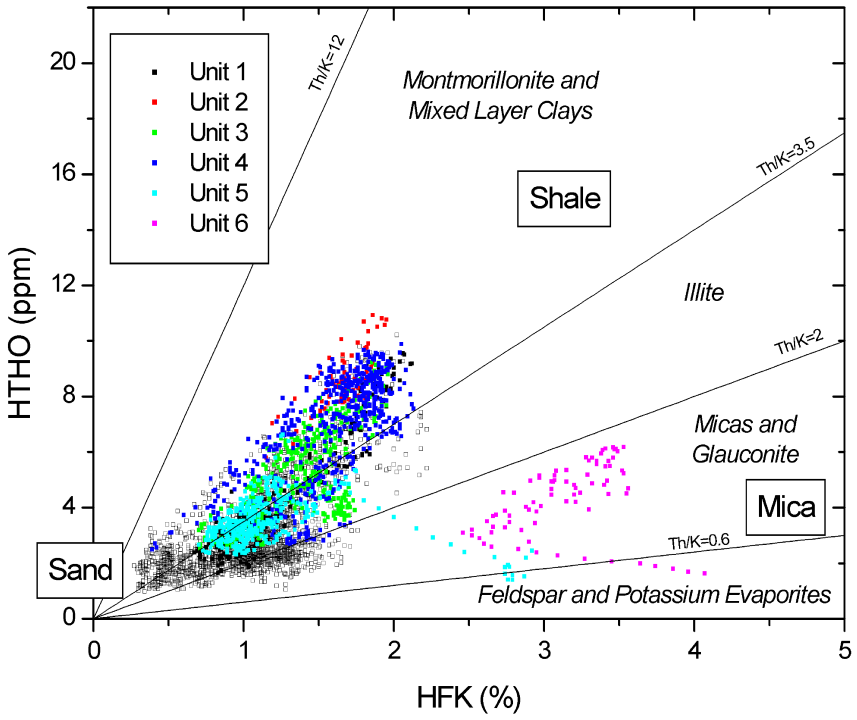

Figure B.3.: Cross plot of thorium and potassium concentrations determined from Mallik 5L-38 natural gamma-ray spectroscopy logs. Unit 1-6: lithological units adopted from *Medioli et al.* (2005). Th/K divisions after *Ellis* (1987).

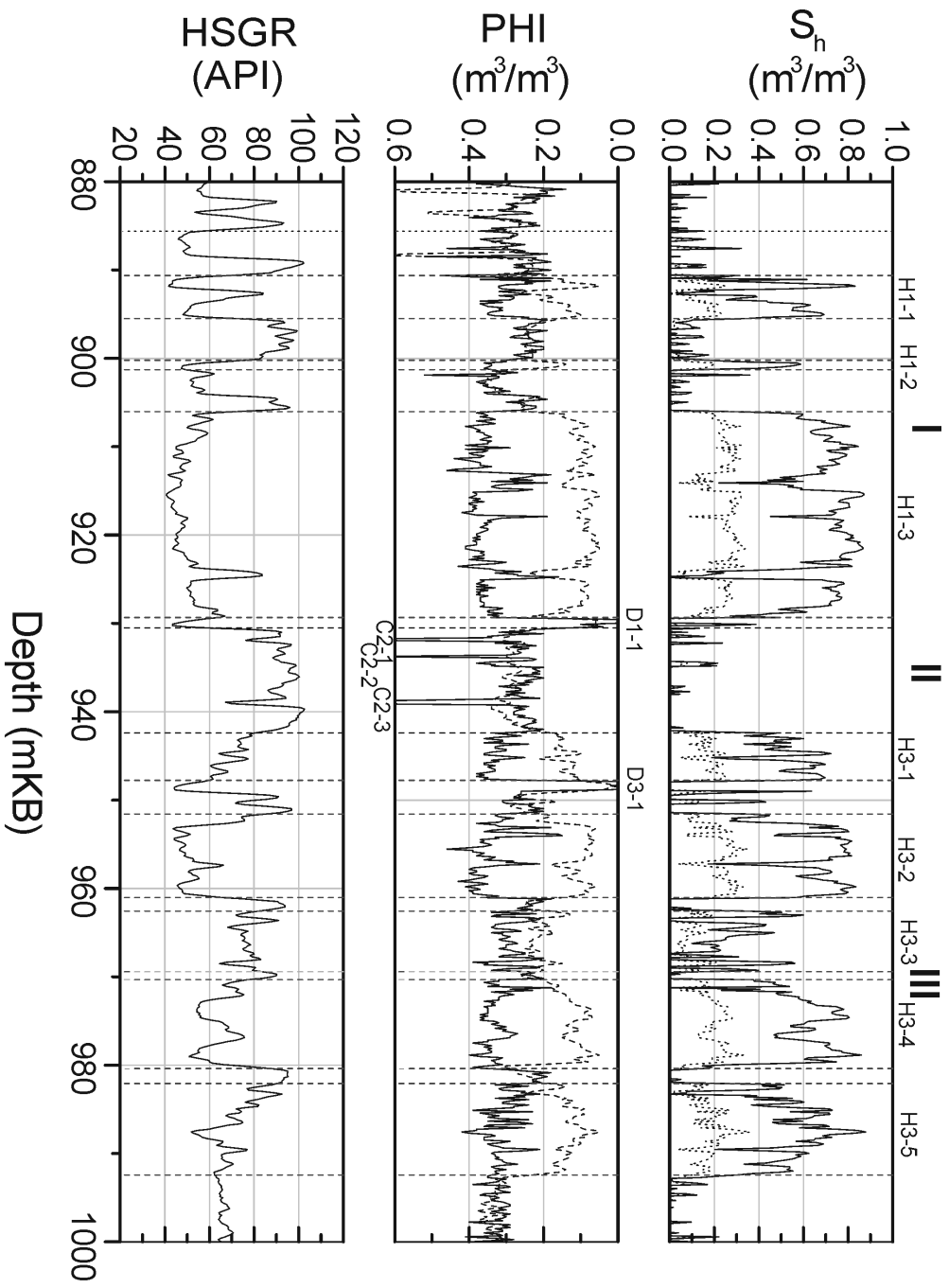

Figure B.4.: Apparent porosity and log-derived gas hydrate saturation, 880 m to 1000 m interval of Mallik 5L-38. HSGR: standard gamma-ray; PHI: apparent porosity (solid line: gamma-gamma density log apparent porosity, dashed line: magnetic resonance apparent porosity); S_h: Density-Magnetic Resonance Method gas hydrate saturation (solid line: saturation, dotted line: bulk-rock volumetric fraction). Roman numerals: lithological units adopted from *Medioli et al.* (2005).

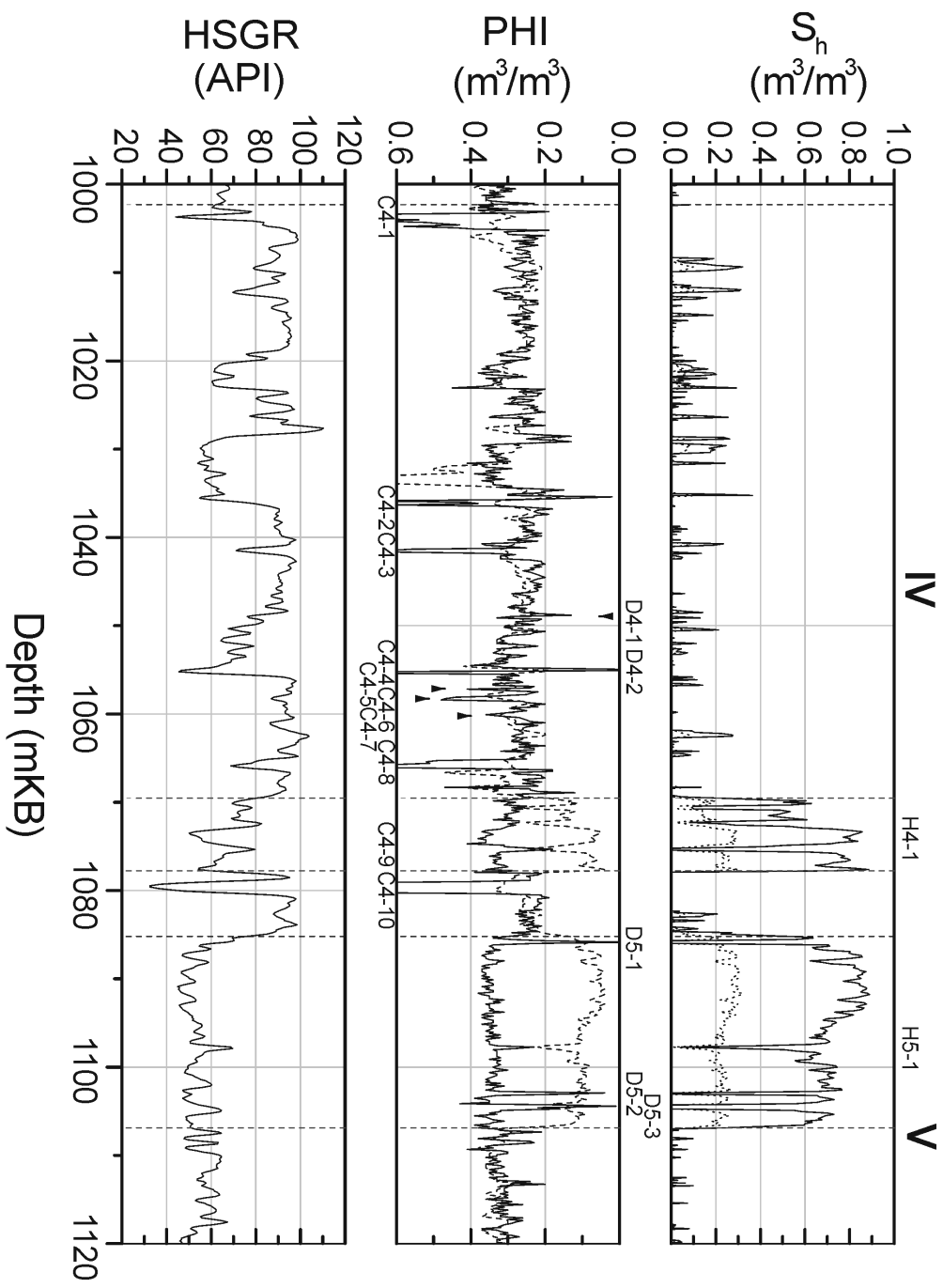

Figure B.5.: Apparent porosity and log-derived gas hydrate saturation, 1000 m to 1120 m interval of Mallik 5L-38. HSGR: standard gamma-ray; PHI: apparent porosity (solid line: gamma-gamma density log apparent porosity, dashed line: magnetic resonance apparent porosity); S_h: Density-Magnetic Resonance Method gas hydrate saturation (solid line: saturation, dotted line: bulk-rock volumetric fraction). Roman numerals: lithological units adopted from *Medioli et al.* (2005).

Table B.1.: Coal and dolomite cemented sandstone layers identified in Mallik 5L-38 core and logging data. Lithological description and core sample data adopted from *Medioli et al.* (2005). GR: gamma-ray log intensity; RHOI: gamma-gamma log density; TCMR: magnetic resonance apparent porosity.

	Core samples				Log data					
Layer ID	Sediment description	Top (m KB)	Bottom (m KB)	Offset to log (m)	Top (mKB)	Bottom (mKB)	Thickness (m)	GR (API)	RHOI (kg/m^3)	TCMR (m^3/m^3)
C2-1	black coal	934.00	934.30	2.30	931.69	932.00	0.31	76	1710	0.31
C2-2	balck and brown coal	935.60	935.75	1.93	933.67	933.82	0.15	89	1983	0.29
C2-3	black platy coal	940.50	940.95	1.84	938.63	939.15	0.52	67	1604	0.30
C4-1	platy brown and black coal, amber droplets	1004.95	1007.25	1.90	1003.32	1005.08	1.76	44	1679	0.32
C4-2	black and brown coal	1033.40	1034.00	-2.38	1035.78	1036.39	0.61	55	1784	0.33
C4-3	brown coal, silt lenses, amber	1042.30	1043.40	1.36	1041.27	1041.72	0.45	71	1652	0.31
C4-4	black and brown coal, amber	1053.50	1053.80	-1.64	1055.14	1055.44	0.30	45	1479	0.24
C4-5	black coal	1055.50	1055.70	-1.63	1057.12	1057.35	0.23	93	2060	0.31
C4-6	black coal	1056.35	1056.80	-1.65	1057.96	1058.49	0.53	86	1940	0.33
C4-7	black coal	1060.55	1060.80	0.58	1059.94	1060.25	0.31	94	2098	0.32
C4-8	chaotic mix of coal and drilling mud	1067.80	1068.10	2.26	1065.19	1066.19	1.00	68	1729	0.29
C4-9	black coal with silt laminae	1080.00	1080.30	2.23	1077.85	1078.00	0.15	70	2013	0.19
C4-10	black and brown coal with amber	1081.50	1082.20	2.17	1078.99	1080.36	1.37	32	1497	0.32
C5-1	black coal	1096.20	1096.32	n/a	not identified in logs					
C5-2	black coal	1101.40	1101.45	n/a	not identified in logs					
D1-1	indeterminate	931.50	932.64	2.09	929.41	930.55	1.14	n/a	2731	0.06
D3-1	dolomite cemented sand	949.05	949.80	1.08	947.78	948.91	1.13	n/a	2682	0.04
D4-1	sand, dolomite cemented	1049.94	1050.13	n/a	not identified in logs					
D4-2	sand, dolomite cemented	1053.14	1053.21	-1.80	1054.83	1055.13	0.30	n/a	2742	0.23
D5-1	massive fine sand with randomly oriented organic material (coal)	1087.60	1089.00	2.45	1085.70	1086.00	0.30	n/a	2428	0.10
D5-2	dolomite cemented medium sand with mud clasts & organic lenses	1104.90	1105.23	2.08	1102.84	1103.14	0.30	n/a	2492	0.12
D5-3	indeterminate	1106.35	1106.75	2.02	1104.24	1104.82	0.58	n/a	2435	0.13

C. Details of Drilling and Cementing Operations, Mallik 3L-38 Well

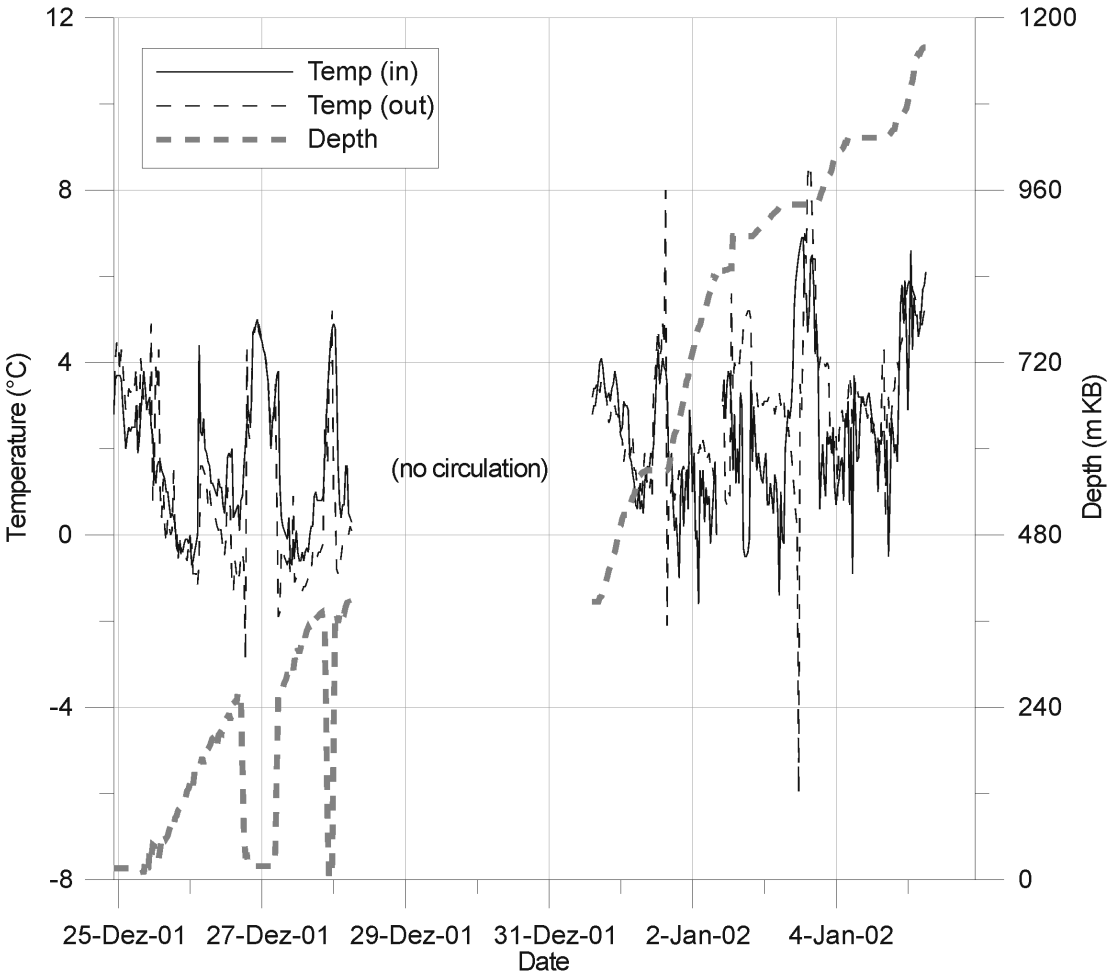

Figure C.1.: Surface injection (in) and return (out) drilling mud temperatures, Mallik 3L-38 well. Data from mud-logging service company Sperry-Sun.

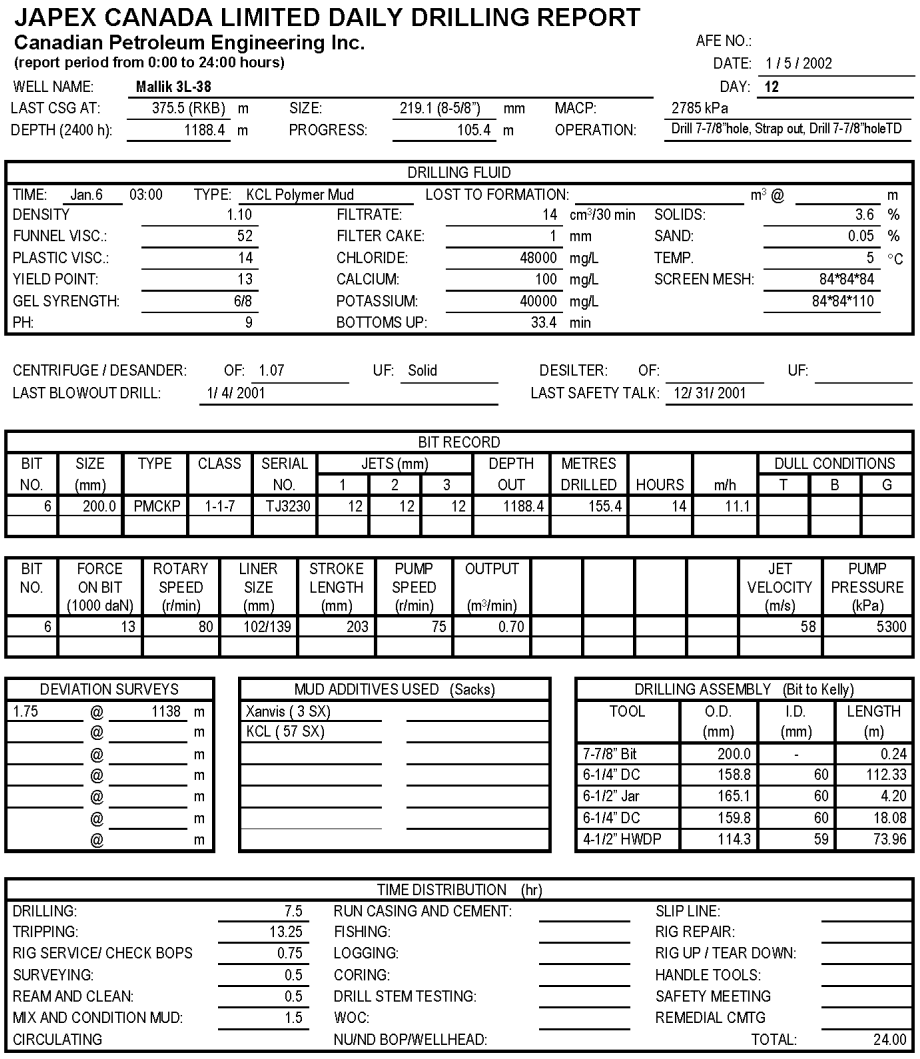

JAPEX CANADA LIMITED DAILY DRILLING REPORT

Canadian Petroleum Engineering Inc.
(report period from 0:00 to 24:00 hours)

AFE NO.:
DATE: 1 / 5 / 2002
DAY: 12

WELL NAME: **Mallik 3L-38**
LAST CSG AT: 375.5 (RKB) m SIZE: 219.1 (8-5/8") mm MACP: 2785 kPa
DEPTH (2400 h): 1188.4 m PROGRESS: 105.4 m OPERATION: Drill 7-7/8"hole, Strap out, Drill 7-7/8"holeTD

DRILLING FLUID

TIME: Jan.6 03:00 TYPE: KCL Polymer Mud LOST TO FORMATION: m³ @ m

DENSITY	1.10	FILTRATE:	14	cm³/30 min	SOLIDS:	3.6	%
FUNNEL VISC.:	52	FILTER CAKE:	1	mm	SAND:	0.05	%
PLASTIC VISC.:	14	CHLORIDE:	48000	mg/L	TEMP.	5	°C
YIELD POINT:	13	CALCIUM:	100	mg/L	SCREEN MESH:	84*84*84	
GEL SYRENGTH:	6/8	POTASSIUM:	40000	mg/L		84*84*110	
PH:	9	BOTTOMS UP:	33.4	min			

CENTRIFUGE / DESANDER: OF: 1.07 UF: Solid DESILTER: OF: UF:
LAST BLOWOUT DRILL: 1/ 4/ 2001 LAST SAFETY TALK: 12/ 31/ 2001

BIT RECORD

BIT NO.	SIZE (mm)	TYPE	CLASS	SERIAL NO.	JETS (mm) 1	2	3	DEPTH OUT	METRES DRILLED	HOURS	m/h	DULL CONDITIONS T	B	G
6	200.0	PMCKP	1-1-7	TJ3230	12	12	12	1188.4	155.4	14	11.1			

BIT NO.	FORCE ON BIT (1000 daN)	ROTARY SPEED (r/min)	LINER SIZE (mm)	STROKE LENGTH (mm)	PUMP SPEED (r/min)	OUTPUT (m³/min)					JET VELOCITY (m/s)	PUMP PRESSURE (kPa)
6	13	80	102/139	203	75	0.70					58	5300

DEVIATION SURVEYS

1.75	@	1138	m
	@		m
	@		m
	@		m
	@		m
	@		m
	@		m

MUD ADDITIVES USED (Sacks)

Xanvis (3 SX)	
KCL (57 SX)	

DRILLING ASSEMBLY (Bit to Kelly)

TOOL	O.D. (mm)	I.D. (mm)	LENGTH (m)
7-7/8" Bit	200.0	-	0.24
6-1/4" DC	158.8	60	112.33
6-1/2" Jar	165.1	60	4.20
6-1/4" DC	159.8	60	18.08
4-1/2" HWDP	114.3	59	73.96

TIME DISTRIBUTION (hr)

DRILLING:	7.5	RUN CASING AND CEMENT:		SLIP LINE:	
TRIPPING:	13.25	FISHING:		RIG REPAIR:	
RIG SERVICE/ CHECK BOPS	0.75	LOGGING:		RIG UP / TEAR DOWN:	
SURVEYING:	0.5	CORING:		HANDLE TOOLS:	
REAM AND CLEAN:	0.5	DRILL STEM TESTING:		SAFETY MEETING	
MIX AND CONDITION MUD:	1.5	WOC:		REMEDIAL CMTG	
CIRCULATING		NU/ND BOP/WELLHEAD:		TOTAL:	24.00

Figure C.2.: Drilling report, Mallik 3L-38 well, Jan. 5, 2002 (p. 1).

REMARKS – Daily Drilling Report

TIME:	
Jan.05	00:00 – 03:45 Drill 7-7/8 hole from 1083 m to 1150 m
	03:45 – 04:15 Survey1.75 deg, depth 1138 m
	04:15 – 06:15 Drill 7-7/8 hole from 1150 m to 1175 m, stopped drilling for strapping out
	06:15 – 07:00 Circ. & Condition mud
	07:00 – 07:15 Rig service, function test blind ram
	07:15 – 14:00 Strap out to surface Up drag 10 daN@998 m,979 m
	14:00 – 14:15 Rig service, function test annular BOP
	14:15 – 18:30 RIH to 1166 m Down drag 5 daN@998 m,979 m
	18:30 – 19:00 Wash down from 1166 m to 1175 m for cleaning, as a precaution. No Fill
	19:00 – 20:45 Drill 7-7/8 hole from 1175 m to 1188.4 m (7-7/8"hole TD)
	20:45 – 21:30 Circ. & Condition
	21:30 – 21:45 Rig service, function test pipe ram
	21:45 – 24:00 Short trip to 970 m (12 stands). No drag
Jan.06	00:00 – 02:30 Circ. & Condition mud
	02:30 – 02:45 Rig service
	02:45 – 03:00 Safety meeting for lay down pipe
	03:00 – 07:00 POOH & Lay down pipe for running CSG. Drop TOTCO
	07:00 POOH to 200 m
	Mud Gas : - 1188 m: 1-6%

DAILY COSTS:	76 K	OPERATION AT:	Mallik	0700 h:			
CUM COSTS:	5132 K	SPUDDED:	12 / 25 / 2001	KB ELEV:	4.6 m	GL ELEV:	1 m
AFE'D COSTS:		RIG RELEASE:		PROJ TD:	1,150 m	DRILLED:	m

CONTRACTOR:	AKITA Drilling ltd.	RIG NUMBER:	Rig #15
WEATHER CONDITIONS:	Clear, NW , 2 knots, Temp.-25 C	LEASE CONDITIONS:	Ice
WELLSITE SUPERVISOR:	Stan Podulsky/ Cal Piche	REPORT WRITTEN BY:	Tsuyoshi Nomura
		REPORT TAKEN BY:	Ed Fercho / Hideaki Takahashi

7:00 AM UPDATE

ACTIVITY:	POOH & Lay down pipe	MUD PROPERTIES:	SG:1.10, Vis:52
DEPTH	1188.4 m (RKB) (7-7/8"hole TD)	PERSONNEL COUNT:	61

Figure C.3.: Drilling report, Mallik 3L-38 well, Jan. 5, 2002 (p. 2).

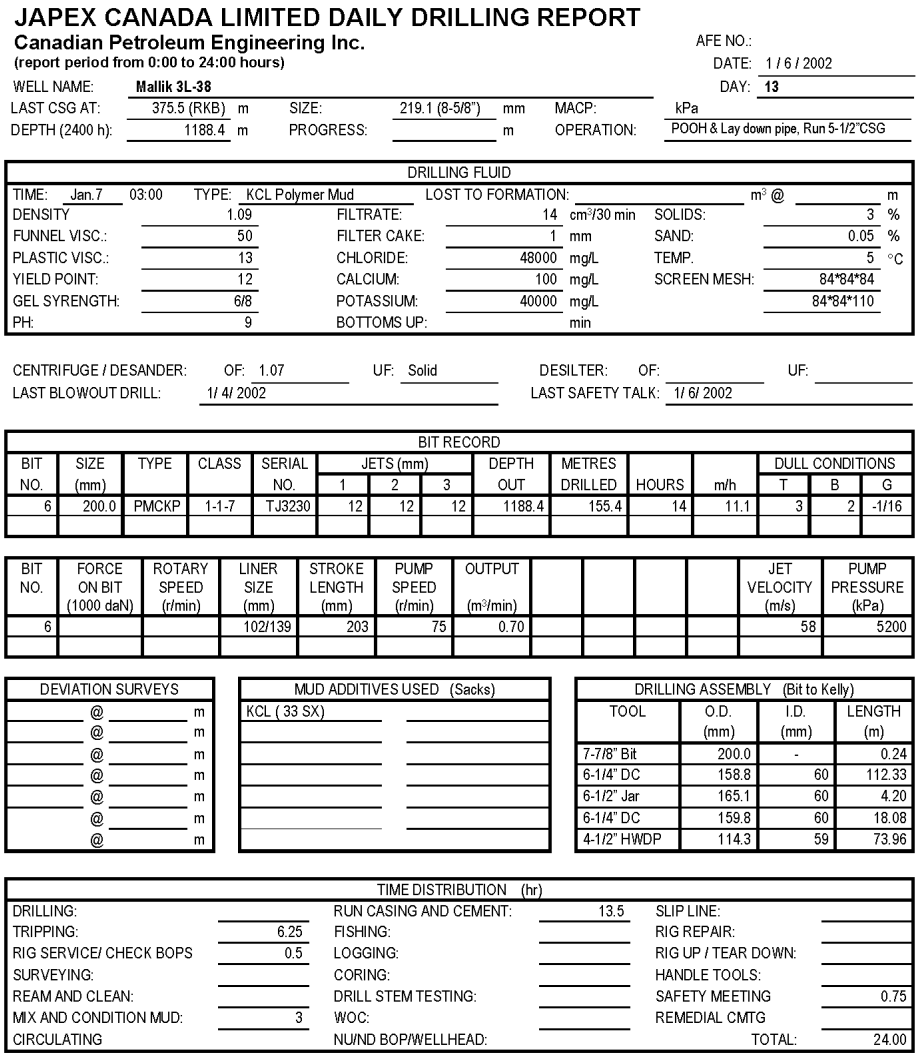

JAPEX CANADA LIMITED DAILY DRILLING REPORT

Canadian Petroleum Engineering Inc.
(report period from 0:00 to 24:00 hours)

AFE NO.:
DATE: 1 / 6 / 2002
DAY: 13

WELL NAME:	Mallik 3L-38							
LAST CSG AT:	375.5 (RKB)	m	SIZE:	219.1 (8-5/8")	mm	MACP:		kPa
DEPTH (2400 h):	1188.4	m	PROGRESS:		m	OPERATION:	POOH & Lay down pipe, Run 5-1/2"CSG	

DRILLING FLUID

TIME:	Jan.7 03:00	TYPE:	KCL Polymer Mud	LOST TO FORMATION:			m³ @	m
DENSITY	1.09	FILTRATE:	14	cm³/30 min	SOLIDS:	3	%	
FUNNEL VISC.:	50	FILTER CAKE:	1	mm	SAND:	0.05	%	
PLASTIC VISC.:	13	CHLORIDE:	48000	mg/L	TEMP.	5	°C	
YIELD POINT:	12	CALCIUM:	100	mg/L	SCREEN MESH:	84*84*84		
GEL SYRENGTH:	6/8	POTASSIUM:	40000	mg/L		84*84*110		
PH:	9	BOTTOMS UP:		min				

CENTRIFUGE / DESANDER: OF: 1.07 UF: Solid DESILTER: OF: UF:
LAST BLOWOUT DRILL: 1/ 4/ 2002 LAST SAFETY TALK: 1/ 6/ 2002

BIT RECORD

BIT NO.	SIZE (mm)	TYPE	CLASS	SERIAL NO.	JETS (mm) 1	2	3	DEPTH OUT	METRES DRILLED	HOURS	m/h	DULL CONDITIONS T	B	G
6	200.0	PMCKP	1-1-7	TJ3230	12	12	12	1188.4	155.4	14	11.1	3	2	-1/16

BIT NO.	FORCE ON BIT (1000 daN)	ROTARY SPEED (r/min)	LINER SIZE (mm)	STROKE LENGTH (mm)	PUMP SPEED (r/min)	OUTPUT (m³/min)					JET VELOCITY (m/s)	PUMP PRESSURE (kPa)
6			102/139	203	75	0.70					58	5200

DEVIATION SURVEYS

	@	m
	@	m
	@	m
	@	m
	@	m
	@	m
	@	m

MUD ADDITIVES USED (Sacks)

KCL (33 SX)	

DRILLING ASSEMBLY (Bit to Kelly)

TOOL	O.D. (mm)	I.D. (mm)	LENGTH (m)
7-7/8" Bit	200.0	-	0.24
6-1/4" DC	158.8	60	112.33
6-1/2" Jar	165.1	60	4.20
6-1/4" DC	159.8	60	18.08
4-1/2" HWDP	114.3	59	73.96

TIME DISTRIBUTION (hr)

DRILLING:		RUN CASING AND CEMENT:	13.5	SLIP LINE:	
TRIPPING:	6.25	FISHING:		RIG REPAIR:	
RIG SERVICE/ CHECK BOPS	0.5	LOGGING:		RIG UP / TEAR DOWN:	
SURVEYING:		CORING:		HANDLE TOOLS:	
REAM AND CLEAN:		DRILL STEM TESTING:		SAFETY MEETING	0.75
MIX AND CONDITION MUD:	3	WOC:		REMEDIAL CMTG	
CIRCULATING		NU/ND BOP/WELLHEAD:		TOTAL:	24.00

Figure C.4.: Drilling report, Mallik 3L-38 well, Jan. 6, 2002 (p. 1).

REMARKS – Daily Drilling Report

TIME:	
Jan.06	00:00 – 02:30 Circ. & Condition mud
	02:30 – 02:45 Rig service
	02:45 – 03:00 Safety meeting for lay down pipe
	03:00 – 09:15 POOH & Lay down pipe for running CSG. Drop TOTCO
	- TOTCO survey failed
	09:15 – 09:30 Rig service, function blind ram
	09:30 – 11:00 Prepare for running CSG & DTS cable
	11:00 – 11:30 Safety meeting for running CSG
	11:30 – 23:30 Run 5-1/2"CSG with DTS cable along the outside CSG
	Run casing: 139.7 mm*K-55*20.85 kg/m*ST&C R3 Contak casing 96 jts (including 1 landing jt)
	Shoe depth:1179 m, Float collar depth:1165.68 m, DTS cable end clamp depth:1153.24 m
	Used bow type centralizer:2 ea
	23:30 – Jan.07 03:15 Circ. & Condition mud
	Check actual hole volume by carbide twice. Equivalent washout is about 5.7 m^3
Jan.07	03:15 – 03:30 Safety meeting for 5-1/2"CSG cementing
	03:30 – 05:30 5-1/2"CSG cementing
	No loss during cementing, No flow back after plug bumped. Good cement returned to surface.
	But, top of cement dropped down after stopping pump. Invisible.
	Preflush: Water 3 m^3,
	Scavenger: 1.2 SG Polaset 1400E; Used Polarset 1400E, 3m3, 1.2 ton
	Fill cement: 1.4 SG Polarset 1400E; Used Polarset 1400E 16m3, 14.8 ton
	Tail cement: 1.88 SG Polarset regular + 0.2%R-7C; Used Polarset regular, 7 m^3, 9.5 ton, R-7C 19 kg
	Displacement Fluid; 11.8m3 x 7%KCL water (below 260m)
	+ 1.5m3 x 25%anti-freeze/75%water (130m – 260m)
	+ 1.5m3 x 100% anti-freeze (top 130m)
	05:30 – 07:00 Prepare for top out job

DAILY COSTS:	107K	OPERATION AT:	Mallik	0700 h:			
CUM COSTS:	5238K	SPUDDED:	12 / 25 / 2001	KB ELEV:	4.6 m	GL ELEV:	1 m
AFE'D COSTS:		RIG RELEASE:		PROJ TD:	1,150 m	DRILLED:	m

CONTRACTOR:	AKITA Drilling ltd.	RIG NUMBER:	Rig #15
WEATHER CONDITIONS:	Snow, NW , 5 knots, Temp.-22 C	LEASE CONDITIONS:	Ice
WELLSITE SUPERVISOR:	Stan Podulsky/ Cal Piche	REPORT WRITTEN BY:	Tsuyoshi Nomura
		REPORT TAKEN BY:	Ed Fercho / Hideaki Takahashi

7:00 AM UPDATE

ACTIVITY:	Prepare for top out job	MUD PROPERTIES:	SG:1.09, Vis:50
DEPTH	1179 m (RKB)	PERSONNEL COUNT:	60

Figure C.5.: Drilling report, Mallik 3L-38 well, Jan. 6, 2002 (p. 2).

D. Simulation Results: Horner Plots of Calculated Temperatures

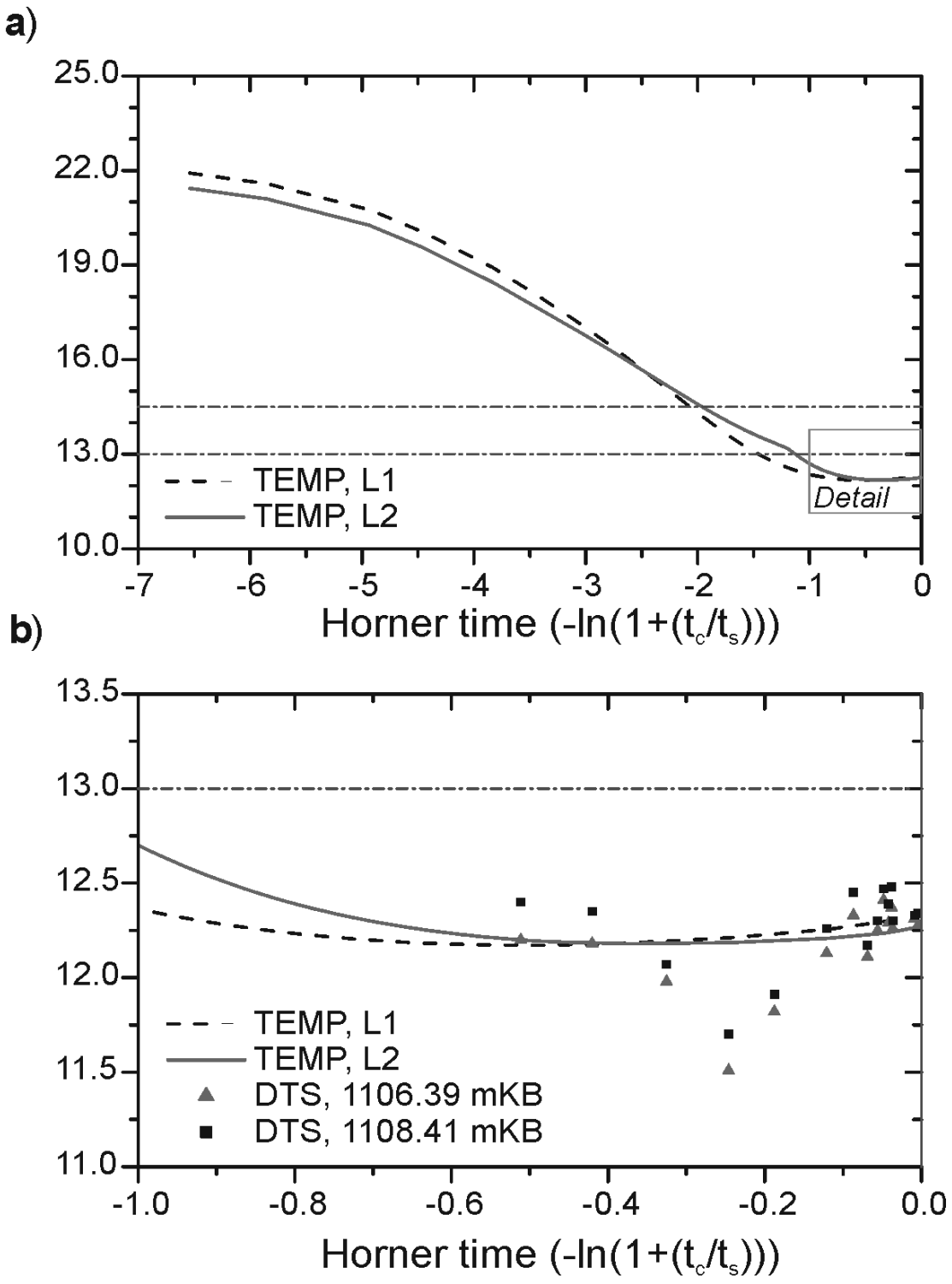

Figure D.1.: Horner plot of calculated temperatures (TEMP) during temperature recovery period (LS 9-10) at r = 0.07 m, reversible phase transition (Scenario A). L1: y = 1.75 m, L2: y = 3.25 m. t_c: circulation time, t_s: shut-in time. DTS: measured temperatures. Dash-dot line: phase transition interval.

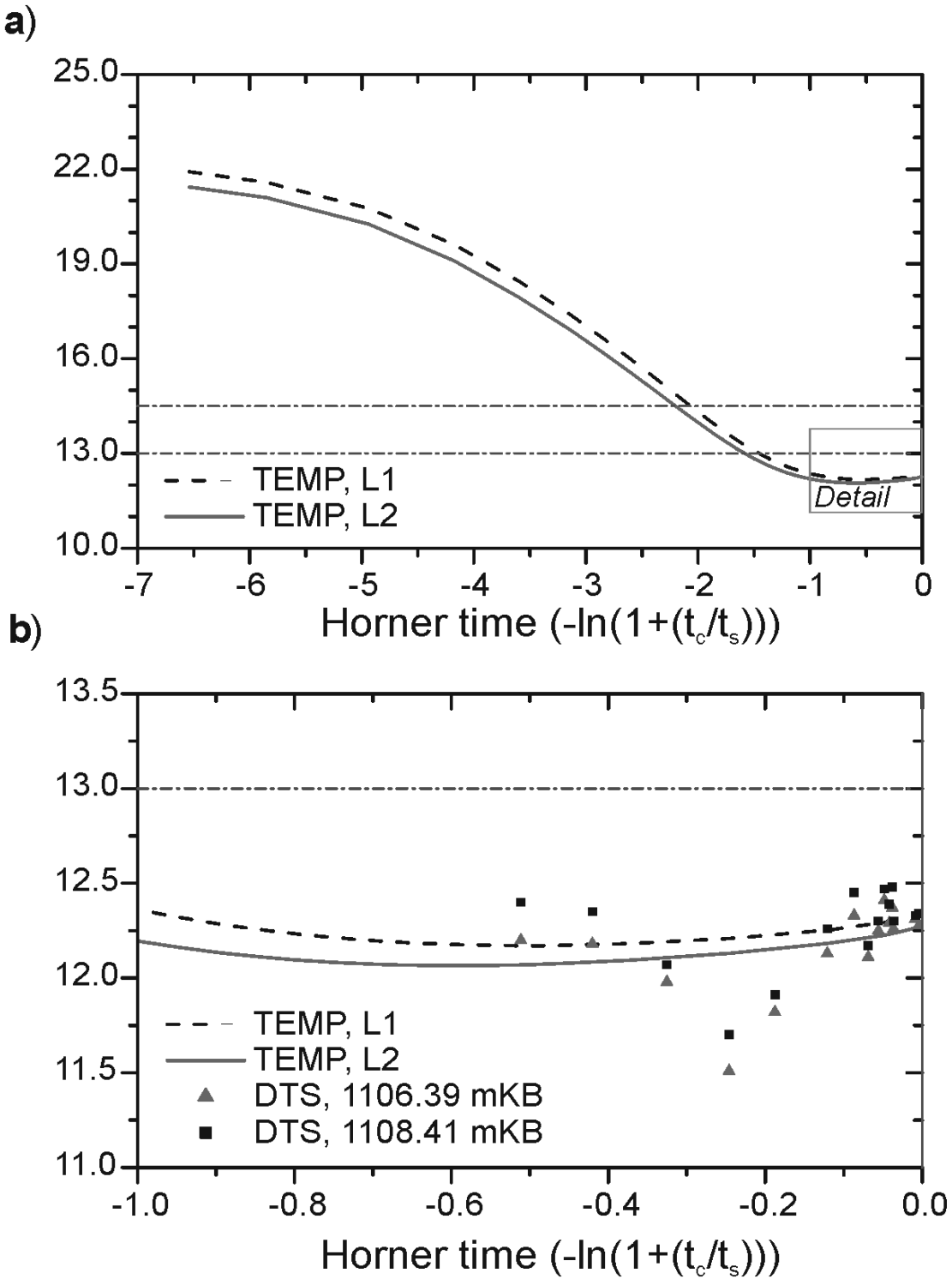

Figure D.2.: Horner plot of calculated temperatures (TEMP) during temperature recovery period (LS 9-10) at r = 0.07 m, inhibited hydrate regeneration (Scenario B1). L1: y = 1.75 m, L2: y = 3.25 m. t_c: circulation time, t_s: shut-in time. DTS: measured temperatures. Dash-dot line: phase transition interval.

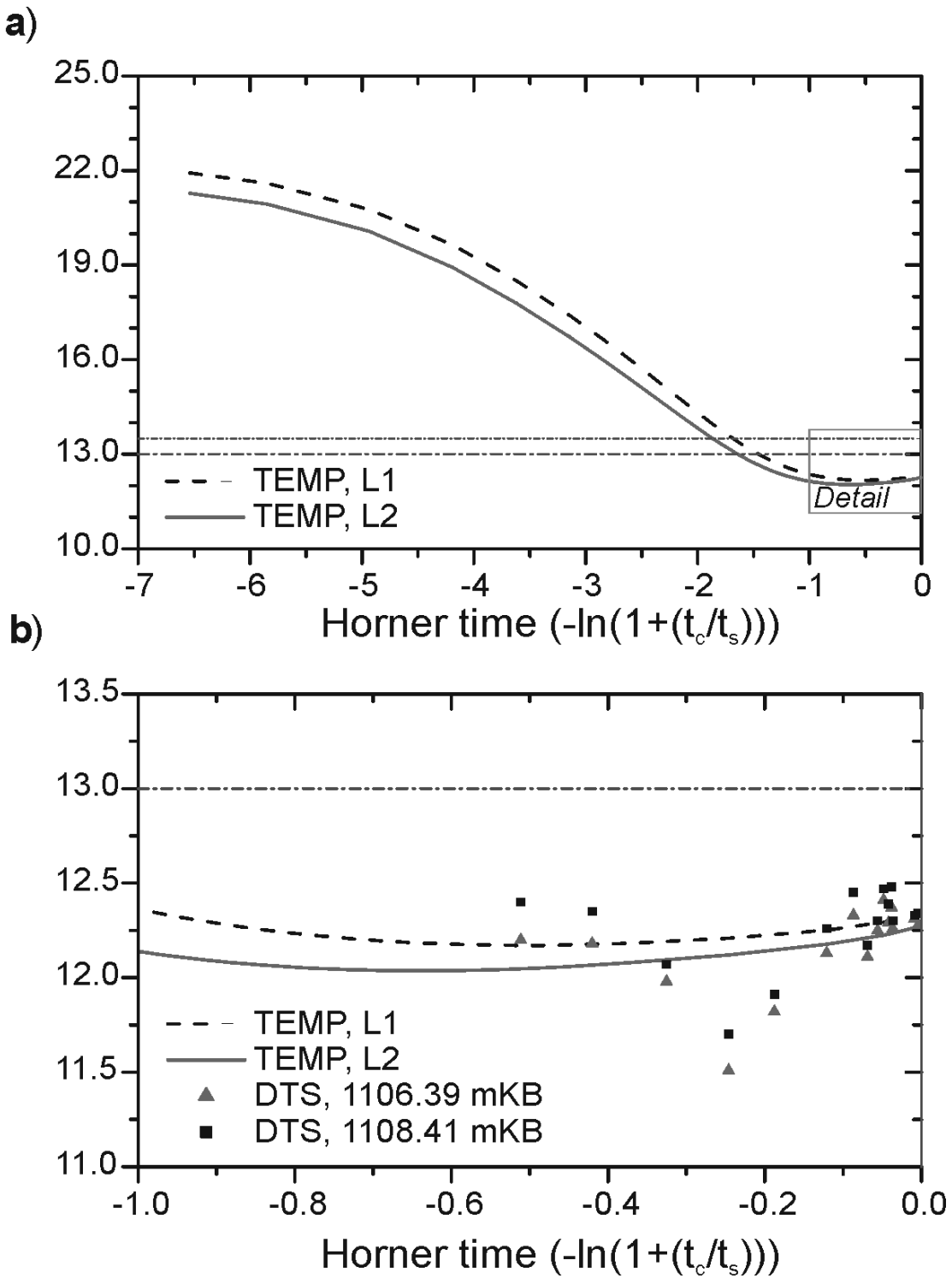

Figure D.3.: Horner plot of calculated temperatures (TEMP) during temperature recovery period (LS 9-10) at r = 0.07 m, inhibited hydrate regeneration (Scenario B2). L1: y = 1.75 m, L2: y = 3.25 m. t_c: circulation time, t_s: shut-in time. DTS: measured temperatures. Dash-dot line: phase transition interval.

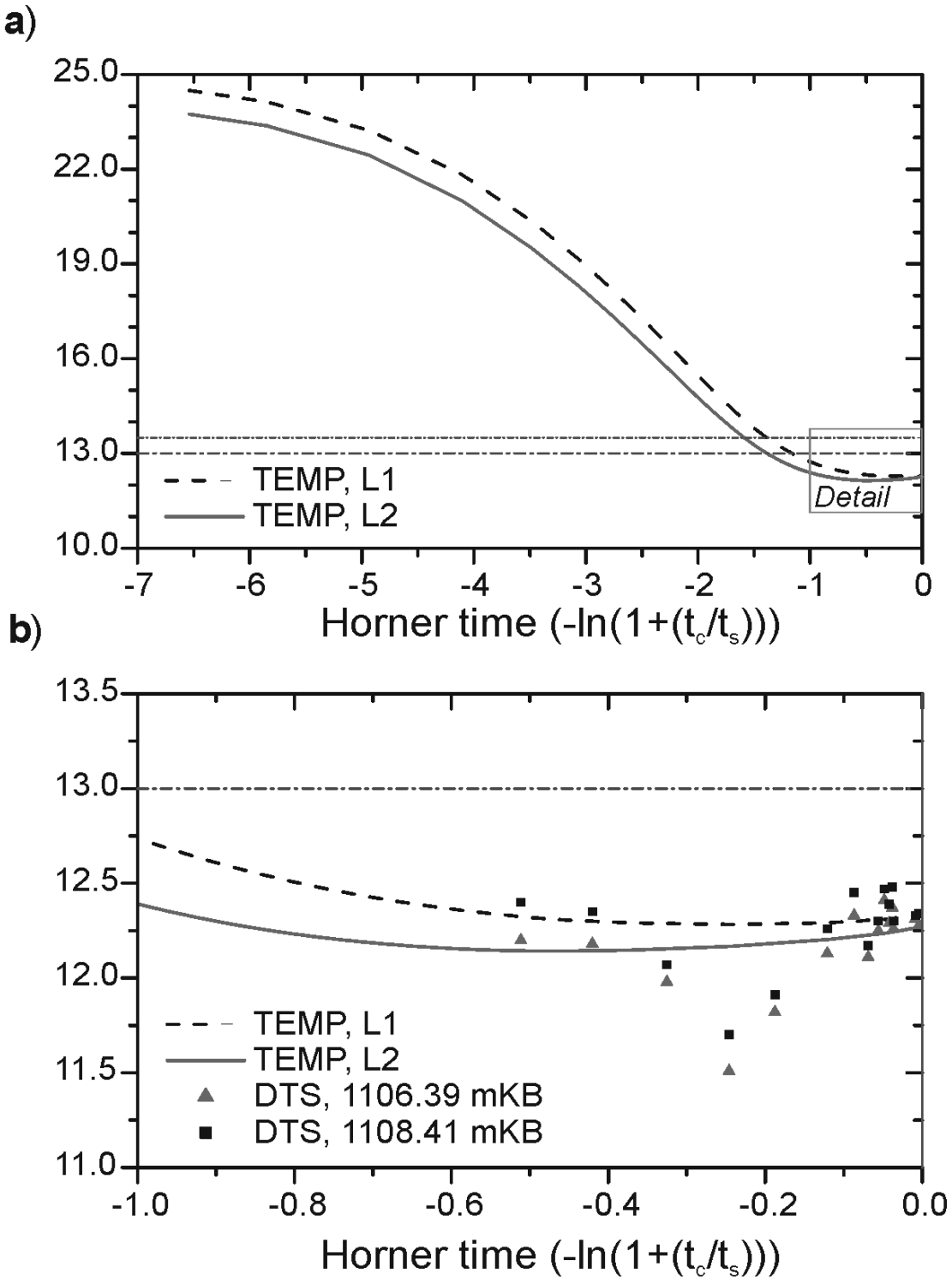

Figure D.4.: Horner plot of calculated temperatures (TEMP) during temperature recovery period (LS 9-10) at r = 0.07 m, inhibited hydrate regeneration (Scenario B3). L1: y = 1.75 m, L2: y = 3.25 m. t_c: circulation time, t_s: shut-in time. DTS: measured temperatures. Dash-dot line: phase transition interval.

E. Simulation Results: Radial Profiles of Calculated Temperatures

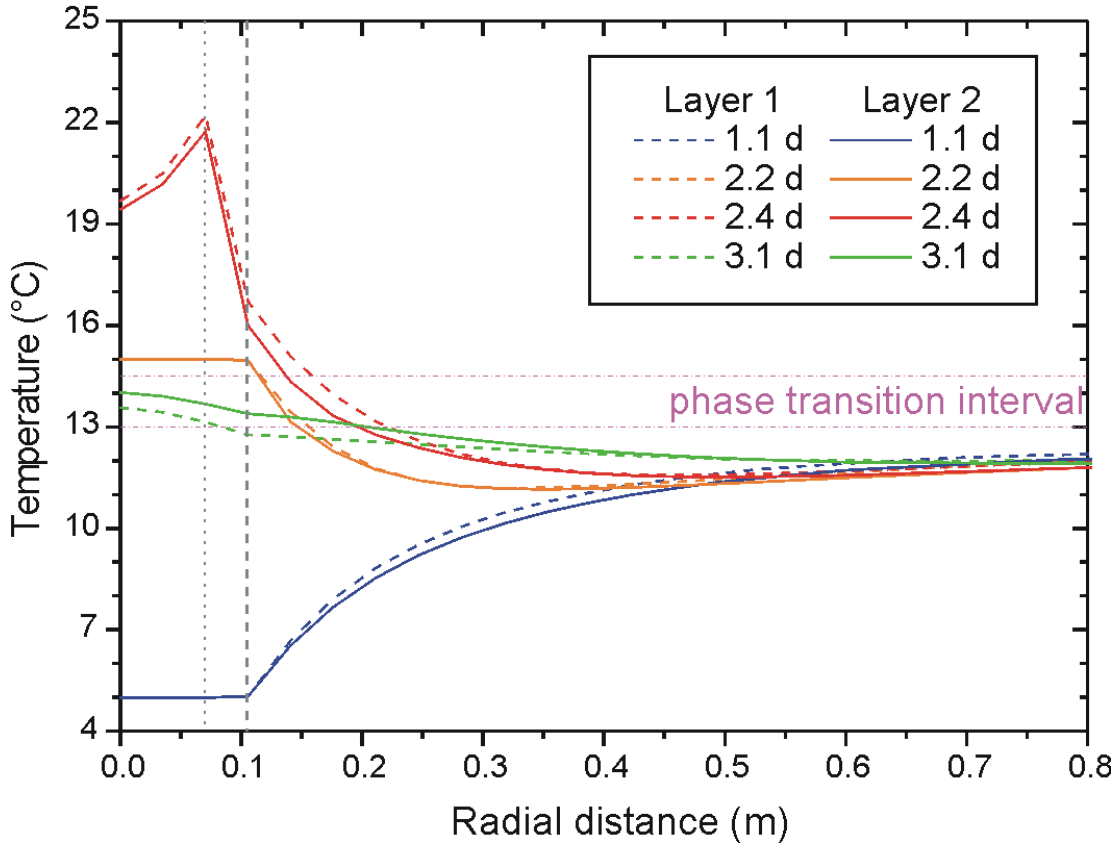

Figure E.1.: Radial temperature profiles, reversible phase transition (Scenario A). L1: y = 1.75 m, L2: y = 3.25 m. Grey dotted line: borehole casing, grey dashed line: borehole wall, dash-dot line: phase transition interval. Time given as total simulation time (days). 1.1 d: end of circulation period (LS 5), 2.2 d: end of pumping of cement (LS 7), 2.4 d: end of release of heat of hydration (LS 8), 3.1 d: during temperature recovery period (LS 9).

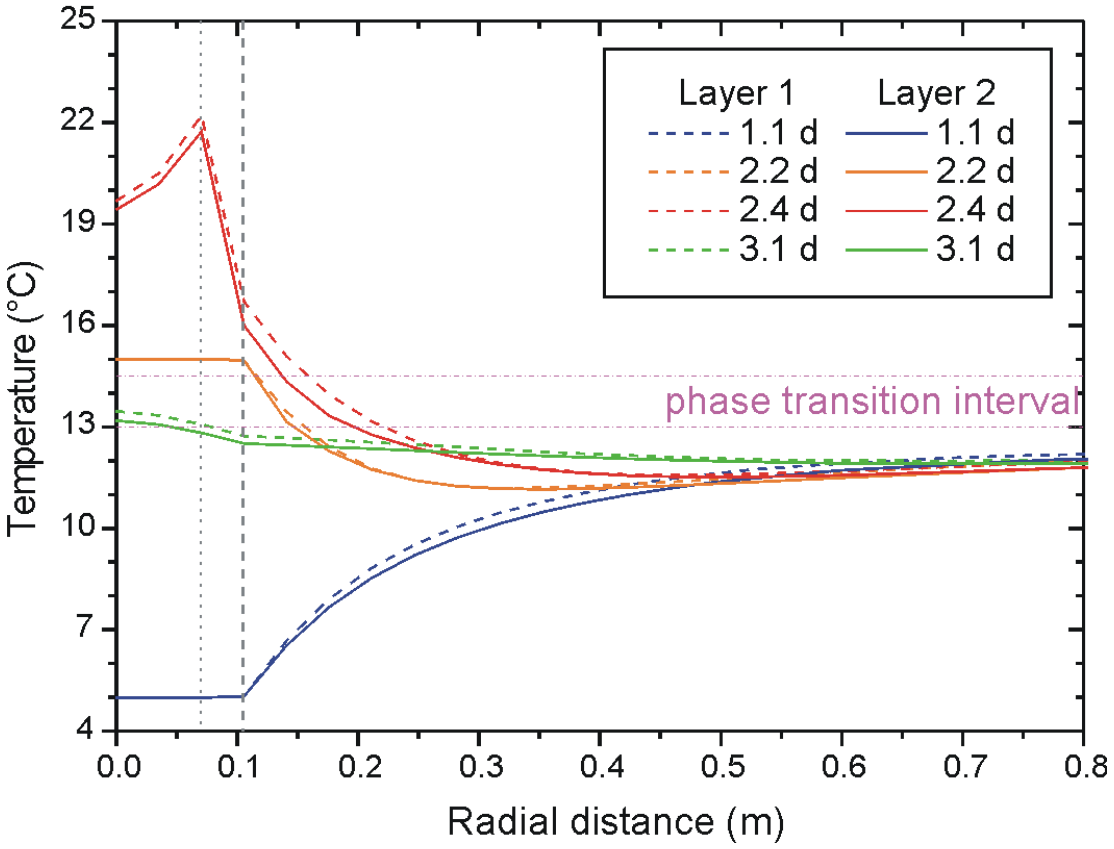

Figure E.2.: Radial temperature profiles, inhibited hydrate regeneration (Scenario B1). L1: y = 1.75 m, L2: y = 3.25 m. Grey dotted line: borehole casing, grey dashed line: borehole wall, dash-dot line: phase transition interval. Time given as total simulation time (days). 1.1 d: end of circulation period (LS 5), 2.2 d: end of pumping of cement (LS 7), 2.4 d: end of release of heat of hydration (LS 8), 3.1 d: during temperature recovery period (LS 9).

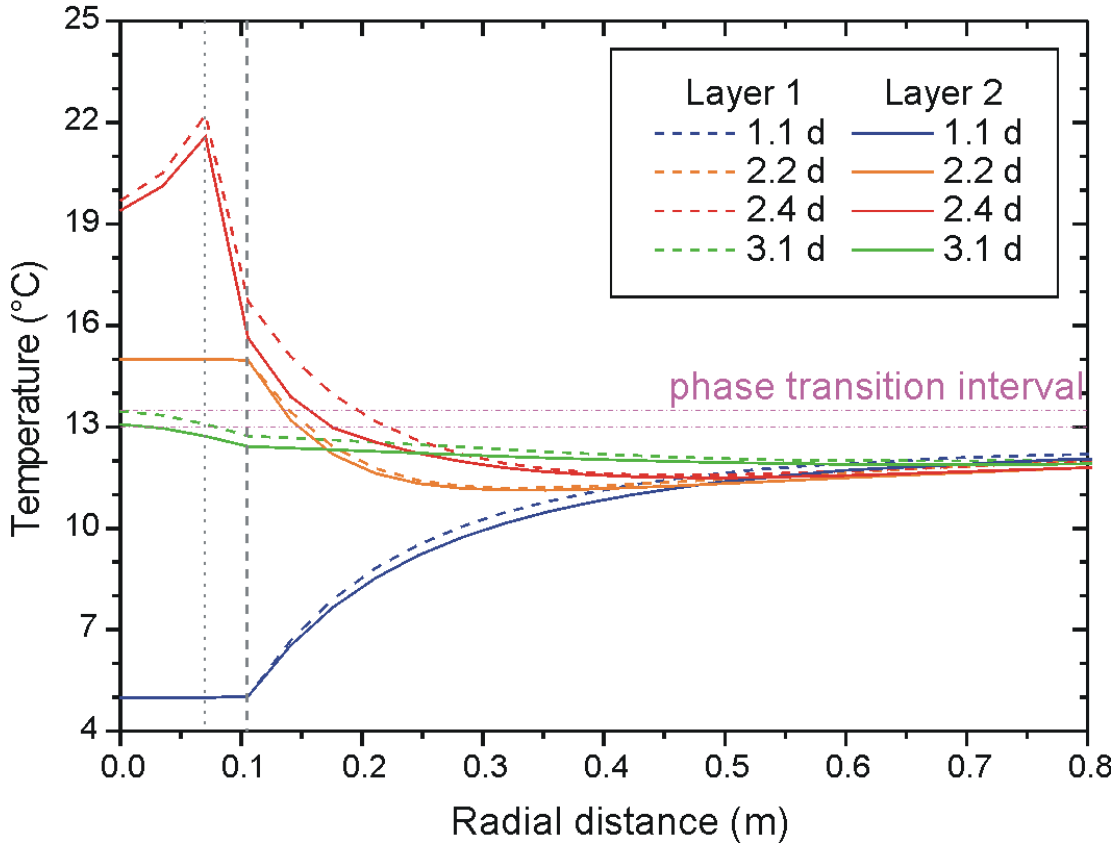

Figure E.3.: Radial temperature profiles, inhibited hydrate regeneration (Scenario B2). L1: y = 1.75 m, L2: y = 3.25 m. Grey dotted line: borehole casing, grey dashed line: borehole wall, dash-dot line: phase transition interval. Time given as total simulation time (days). 1.1 d: end of circulation period (LS 5), 2.2 d: end of pumping of cement (LS 7), 2.4 d: end of release of heat of hydration (LS 8), 3.1 d: during temperature recovery period (LS 9).

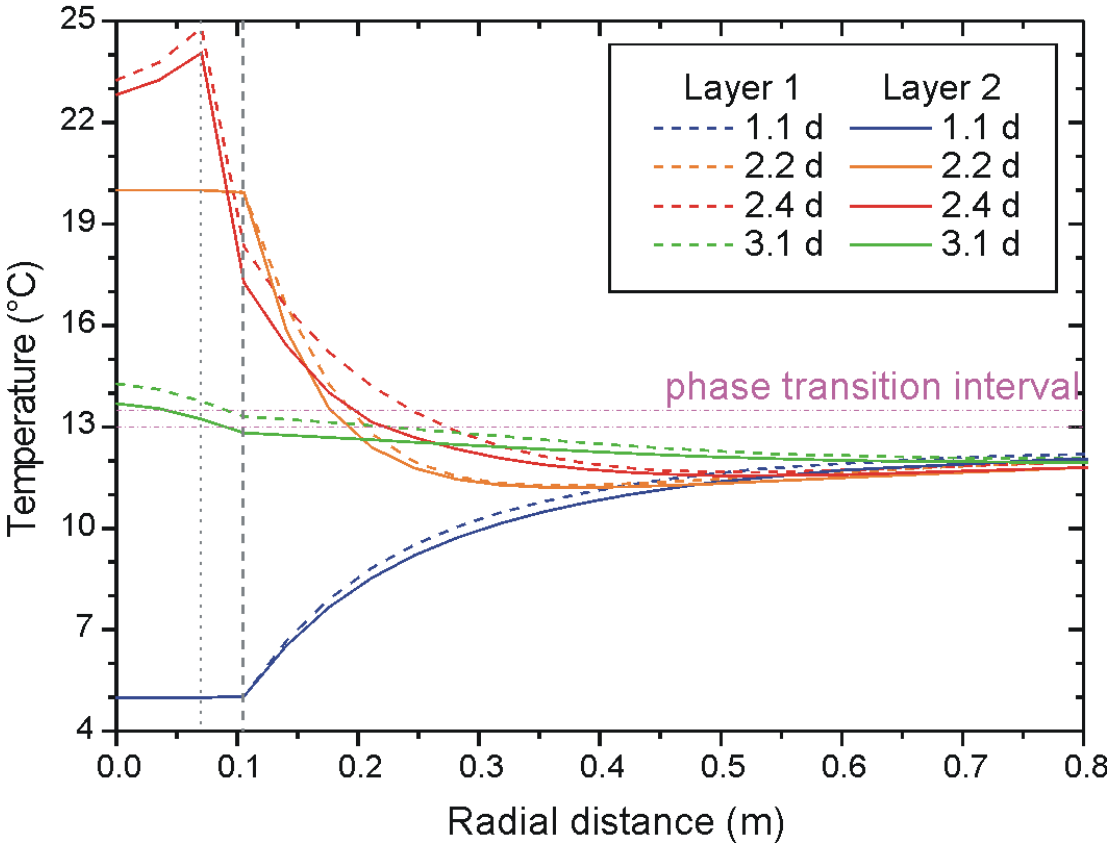

Figure E.4.: Radial temperature profiles, inhibited hydrate regeneration (Scenario B3). L1: y = 1.75 m, L2: y = 3.25 m. Grey dotted line: borehole casing, grey dashed line: borehole wall, dash-dot line: phase transition interval. Time given as total simulation time (days). 1.1 d: end of circulation period (LS 5), 2.2 d: end of pumping of cement (LS 7), 2.4 d: end of release of heat of hydration (LS 8), 3.1 d: during temperature recovery period (LS 9).

Bibliography

Alexiades, V., and A. D. Solomon (1993), *Mathematical modeling of melting and freezing processes*, 323 pp., Hemisphere Publishing Corporation, Washington.

Beck, A. E. (1988), Methods for determining thermal conductivity and thermal diffusivity, in *Handbook of Terrestrial Heat-Flow Density Determination*, edited by R. Haenel, L. Rybach, and L. Stegena, pp. 87–124, Kluwer Academic Publishers, Dordrecht, Netherlands.

Bily, C., and J. W. L. Dick (1974), Naturally occurring gas hydrates in the Mackenzie Delta, N.W.T, *Bulletin of Canadian Petroleum Geology*, *22*(3), 340–352.

Brigaud, F., and G. Vasseur (1989), Mineralogy, porosity and fluid control on thermal conductivity of sedimentary rocks, *Geophysical Journal International*, *98*(3), 525–542.

Bullard, E. C. (1947), The time necessary for a borehole to attain temperature equilibrium, *Monthly Notices of the Royal Astronomical Society, Geophysical Supplement*, *5*(5), 127–130.

Büttner, G., and E. Huenges (2003), The heat transfer in the region of the Mauna Kea (Hawaii)-constraints from borehole temperature measurements and coupled thermo-hydraulic modeling, *Tectonophysics*, *371*(1-4), 23–40.

Cermak, V., and L. Rybach (1982), Thermal properties, in *Physical Properties of Rocks*, *Landolt-Börnstein / Numerical Data and Functional Relationships in Science and Technology*, vol. V/1a, edited by G. Angenheister, pp. 305–371, Springer, Berlin.

Clauser, C., and E. Huenges (1995), Thermal conductivity of rocks and minerals, in *Rock Physics and Phase Relations: A Handbook of Physical Constants*, edited by T. J. Ahrens, pp. 105–126, American Geophysical Union, Washington.

Collett, T. S. (1993), Natural gas hydrates of the Prudhoe Bay and Kuparuk River area, North Slope, Alaska, *AAPG Bulletin*, *77*(5), 793–812.

Collett, T. S. (2001), A review of well-log analysis techniques used to assess gas-hydrate-bearing reservoirs, in *Natural Gas Hydrates - Occurrence, Distribution, and Detection*, *Geophysical Monograph*, vol. 124, edited by C. K. Paull and W. P. Dillon, pp. 189–210, American Geophysical Union, Washington.

Collett, T. S., M. W. Lee, S. R. Dallimore, and W. F. Agena (1999), Seismic- and well-log-inferred gas hydrate accumulations on Richards Island, in *Scientific Results from*

JAPEX/JNOC/GSC Mallik 2L-38 Gas Hydrate Research Well, Mackenzie Delta, Northwest Territories, Canada, edited by S. R. Dallimore, T. Uchida, and T. S. Collett, Bulletin 544, pp. 357–376, Geological Survey of Canada, Ottawa.

Cook, J. G., and D. G. Leaist (1983), An exploratory study of the thermal conductivity of methane hydrate, *Geophysical Research Letters*, *10*(5), 397–399.

Dallimore, S. R., and C. R. Burn (1997), Setting of the delta, in *The Mackenzie Delta Borehole Project, Environmental Studies Research Funds Report 135*, edited by S. R. Dallimore and J. V. Matthews, Geological Survey of Canada, Calgary, CD-ROM.

Dallimore, S. R., and T. S. Collett (1995), Intrapermafrost gas hydrates from a deep core hole in the Mackenzie Delta, Northwest Territories, Canada, *Geology*, *23*(6), 527–530.

Dallimore, S. R., and T. S. Collett (1999), Regional gas hydrate occurrences, permafrost conditions, and Cenozoic geology, Mackenzie Delta area, in *Scientific Results from JAPEX/JNOC/GSC Mallik 2L-38 Gas Hydrate Research Well, Mackenzie Delta, Northwest Territories, Canada*, edited by S. R. Dallimore, T. Uchida, and T. S. Collett, Bulletin 544, pp. 31–43, Geological Survey of Canada, Ottawa.

Dallimore, S. R., and T. S. Collett (2005), *Scientific Results from the Mallik 2002 Gas Hydrate Production Research Well Program, Mackenzie Delta, Northwest Territories, Canada*, Geological Survey of Canada Bulletin 585, Ottawa.

Dallimore, S. R., T. S. Collett, and T. Uchida (1999), Overview of science program, JAPEX/JNOC/GSC Mallik 2L-38 gas hydrate research well, in *Scientific Results from JAPEX/JNOC/GSC Mallik 2L-38 Gas Hydrate Research Well, Mackenzie Delta, Northwest Territories, Canada*, edited by S. R. Dallimore, T. Uchida, and T. S. Collett, Bulletin 544, pp. 11–17, Geological Survey of Canada, Ottawa.

Dallimore, S. R., T. S. Collett, M. Weber, and T. Uchida (2002), Drilling program investigates permafrost gas hydrates, *Eos, Transactions, American Geophysical Union*, *83*(18), 193, 198.

Dallimore, S. R., A. E. Taylor, J. F. Wright, F. M. Nixon, T. S. Collett, and T. Uchida (2005), Overview of the coring program for the JAPEX/JNOC/GSC et al. Mallik 5L-38 gas hydrate production research well, in *Scientific Results from the Mallik 2002 Gas Hydrate Production Research Well Program, Mackenzie Delta, Northwest Territories, Canada*, edited by S. R. Dallimore and T. S. Collett, Bulletin 585, Geological Survey of Canada, Ottawa, 17 p.

Dantzig, J. A. (1989), Modeling liquid-solid phase changes with melt convection, *International Journal for Numerical Methods in Engineering*, *28*, 1769–1785.

Davie, M. K., O. Y. Zatsepina, and B. A. Buffett (2004), Methane solubility in marine hydrate environments, *Marine Geology*, *203*(1-2), 177–184.

Dickens, G. R., and M. S. Quinby-Hunt (1994), Methane hydrate stability in seawater, *Geophysical Research Letters*, *21*(19), 2115–2118.

Dixon, J. (1996), Geological atlas of the Beaufort-Mackenzie area, *Miscellaneous report 59*, Geological Survey of Canada, Ottawa, Ontario, 173 p., 73 maps.

Dixon, J., and J. R. Dietrich (1990), Canadian Beaufort Sea and adjacent land areas, in *The Arctic Ocean region*, *The Geology of North America*, vol. L, edited by A. Grantz, L. Johnson, and J. F. Sweeney, pp. 239–256, The Geological Society of America, Boulder.

Dixon, J., J. R. Dietrich, and D. H. McNeil (1992), Upper Cretaceous to Pleistocene sequence stratigraphy of the Beaufort-Mackenzie and Banks Island areas, Northwest Canada, *Bulletin 407*, Geological Survey of Canada, Ottawa, 90 p.

Ellis, D. V. (1987), *Well logging for earth scientists*, Elsevier, New York.

Farouki, O. T. (1981), Thermal properties of soils, *Tech. Rep. CRREL Monograph 81-1*, United States Army Corps of Engineers, Cold Regions Research and Engineering Laboratory.

Fofonoff, N. P., and R. C. Millard (1982), Algorithms for computation of fundamental properties of seawater, *Unesco Technical Papers in Marine Science*, *44*, 53.

Förster, A., J. Schrötter, D. F. Merriam, and D. D. Blackwell (1997), Application of optical-fiber temperature logging; an example in a sedimentary environment, *Geophysics*, *62*(4), 1107–1113.

Grattan, K. T. V., and B. T. Meggitt (1995), *Optical Fiber Sensor Technology*, 499 pp., Chapman & Hall, London.

Grosswig, S., E. Hurtig, K. Kühn, and F. Rudolph (2001), Distributed fibre-optic temperature sensing technique (DTS) for surveying underground gas storage facilities, *Oil, Gas (Hamburg)*, *27*(4), 31–34.

Hancock, S., T. S. Collett, S. R. Dallimore, T. Satoh, T. Inoue, E. Huenges, J. Henninges, and B. Weatherill (2005a), Overview of thermal-stimulation production-test results for the JAPEX/JNOC/GSC et al. Mallik 5L-38 gas hydrate production research well, in *Scientific Results from the Mallik 2002 Gas Hydrate Production Research Well Program, Mackenzie Delta, Northwest Territories, Canada*, edited by S. R. Dallimore and T. S. Collett, Bulletin 585, Geological Survey of Canada, Ottawa, 15 p.

Hancock, S., S. R. Dallimore, T. S. Collett, D. Carle, B. Weatherill, T. Satoh, and T. Inoue (2005b), Overview of pressure-drawdown production-test results for the JAPEX/JNOC/GSC et al. Mallik 5L-38 gas hydrate production research well, in *Scientific Results from the Mallik 2002 Gas Hydrate Production Research Well Program, Mackenzie Delta, Northwest Territories, Canada*, edited by S. R. Dallimore and T. S. Collett, Bulletin 585, Geological Survey of Canada, Ottawa, 16 p.

Hartog, A., and G. Gamble (1991), Photonic distributed sensing, *Physics World*, *3*, 45–49.

Hartog, A. H. (1995), Distributed fiber-optic sensors, in *Optical Fiber Sensor Technology*, edited by K. T. V. Grattan and B. T. Meggitt, pp. 347–382, Chapman & Hall, London.

Hayes, W., and R. Loudon (1978), *Scattering of Light by Crystals*, Wiley-Interscience publication, 360 pp., Wiley, New York.

Henninges, J., S. Böde, J. Schrötter, K. Erbas, E. Huenges, and the Mallik Working Group (2003), Permanent installation of fibre-optic DTS-cables in boreholes for temperature monitoring, in *EGS-AGU-EUG Joint Assembly*, *EGS Geophys. Research Abstracts*, vol. 5, Nice, CD-ROM.

Henninges, J., J. Schrötter, K. Erbas, and E. Huenges (2005a), Temperature field of the Mallik gas hydrate occurrence - implications on phase changes and thermal properties, in *Scientific Results from the Mallik 2002 Gas Hydrate Production Research Well Program, Mackenzie Delta, Northwest Territories, Canada*, edited by S. R. Dallimore and T. S. Collett, Bulletin 585, Geological Survey of Canada, Ottawa, 14 p.

Henninges, J., G. Zimmermann, G. Büttner, J. Schrötter, K. Erbas, and E. Huenges (2005b), Wireline distributed temperature measurements and permanent installations behind casing, in *World Geothermal Congress*, Antalya, Turkey, paper 1021.

Holder, G. D., and J. H. Hand (1982), Multiple-phase equilibria in hydrates from methane, ethane, propane and water mixtures, *American Institute of Chemical Engineers Journal*, *28*(3), 440–447.

Hurtig, E., J. Schrötter, S. Grosswig, K. Kühn, B. Harjes, W. Wieferig, and R. P. Orrell (1993), Borehole temperature measurements using distributed fibre optic sensing, *Scientific Drilling*, *3*(6), 283–286.

Jenner, K. A., S. R. Dallimore, I. D. Clark, D. Paré, and B. E. Medioli (1999), Sedimentology of gas hydrate host strata from the JAPEX/JNOC/GSC Mallik 2L-38 gas hydrate research well, in *Scientific Results from JAPEX/JNOC/GSC Mallik 2L-38 Gas Hydrate Research Well, Mackenzie Delta, Northwest Territories, Canada*, edited by S. R. Dallimore, T. Uchida, and T. S. Collett, Bulletin 544, pp. 57–68, Geological Survey of Canada, Ottawa.

Johansen, O. (1975), Thermal conductivity of soils, Ph.D. thesis, Trondheim, Norway.

Judge, A. S., and J. A. Majorowicz (1992), Geothermal conditions for gas hydrate stability in the Beaufort-Mackenzie area: the global change aspect, *Palaeogeography, Palaeoclimatology, Palaeoecology*, *98*(2-4), 251–263.

Judge, A. S., B. R. Pelletier, and I. Norquay (1987), Permafrost base and distribution of gas hydrates, in *Marine Science Atlas of the Beaufort Sea - Geology and Geophysics*, edited by B. R. Pelletier, Miscellaneous Report 40, p. 39, Geological Survey of Canada, Ottawa.

Kleinberg, R. L., C. Flaum, C. Straley, P. G. Brewer, G. E. Malby, E. T. Peltzer III, G. Friederich, and J. P. Yesinowski (2003), Seafloor nuclear magnetic resonance assay

of methane hydrate in sediment and rock, *Journal of Geophysical Research*, *108*(B3), 2137, doi:10.1029/2001JB000919.

Kleinberg, R. L., C. Flaum, and T. S. Collett (2005), Magnetic resonance log of JAPEX/JNOC/GSC et al. Mallik 5L-38 gas hydrate production research well: gas hydrate saturation, growth habit, and relative permeability, in *Scientific Results from the Mallik 2002 Gas Hydrate Production Research Well Program, Mackenzie Delta, Northwest Territories, Canada*, edited by S. R. Dallimore and T. S. Collett, Bulletin 585, Geological Survey of Canada, Ottawa, 10 p.

Kulenkampff, J., and E. Spangenberg (2005), Physical properties of cores from the JAPEX/JNOC/GSC et al. Mallik 5L-38 gas hydrate production research well under simulated in situ conditions using the Field Laboratory Experimental Core Analysis System (FLECAS), in *Scientific Results from the Mallik 2002 Gas Hydrate Production Research Well Program, Mackenzie Delta, Northwest Territories, Canada*, edited by S. R. Dallimore and T. S. Collett, Bulletin 585, Geological Survey of Canada, Ottawa, 16 p.

Kurihara, M., H. Ouchi, T. Inoue, T. Yonezawa, Y. Masuda, S. R. Dallimore, and T. S. Collett (2005), Analysis of the JAPEX/JNOC/GSC et al. Mallik 5L-38 gas hydrate thermal-production test through numerical simulation, in *Scientific Results from the Mallik 2002 Gas Hydrate Production Research Well Program, Mackenzie Delta, Northwest Territories, Canada*, edited by S. R. Dallimore and T. S. Collett, Bulletin 585, Geological Survey of Canada, Ottawa, 20 p.

Kvenvolden, K. A. (1988), Methane hydrate; a major reservoir of carbon in the shallow geosphere?, *Chemical Geology*, *71*, 41–51.

Kvenvolden, K. A. (1999), Potential effects of gas hydrate on human welfare, in *Papers from a National Academy of Sciences colloquium on Geology, mineralogy, and human welfare*, vol. 96; 7, pp. 3420–3426, National Academy of Sciences, Washington, DC, United States.

Lachenbruch, A. H., and M. C. Brewer (1959), Dissipation of the temperature effect of drilling a well in Arctic Alaska, Geological Survey Bulletin 1083-C, pp. 73–109, United States Geological Survey, Washington.

Lachenbruch, A. H., and B. V. Marshall (1986), Changing climate; geothermal evidence from permafrost in the Alaskan Arctic, *Science*, *234*(4777), 689–696.

Lachenbruch, A. H., J. H. Sass, B. V. Marshall, and T. H. Moses, Jr. (1982), Permafrost, heat flow, and the geothermal regime at Prudhoe Bay, Alaska, *Journal of Geophysical Research*, *87*(B11), 9301–9316.

Langseth, M. G., A. H. Lachenbruch, and B. V. Marshall (1990), Geothermal observations in the Arctic region, in *The Arctic Ocean region*, *The Geology of North America*, vol. L, edited by A. Grantz, L. Johnson, and J. F. Sweeney, pp. 133–151, The Geological Society of America, Boulder.

Laurence, O. S., and G. A. Brown (2000), Using real-time fibre optic distributed temperature data for optimising reservoir performance. spe/ps-cim 65478, in *SPE/PS-CIM International Conference on Horizontal Well Technology*, Calgary, Alberta.

Majorowicz, J. A., and K. G. Osadetz (2001), Gas hydrate distribution and volume in Canada, *AAPG Bulletin*, *85*(7), 1211–1230.

Majorowicz, J. A., and S. L. Smith (1999), Review of ground temperatures in the Mallik field area; a constraint to the methane hydrate stability, in *Scientific Results from JAPEX/JNOC/GSC Mallik 2L-38 Gas Hydrate Research Well, Mackenzie Delta, Northwest Territories, Canada*, edited by S. R. Dallimore, T. Uchida, and T. S. Collett, Bulletin 544, pp. 45–56, Geological Survey of Canada, Ottawa.

Majorowicz, J. A., F. W. Jones, and A. S. Judge (1990), Deep subpermafrost thermal regime in the Mackenzie Delta basin, northern Canada; analysis from petroleum bottom-hole temperature data, *Geophysics*, *55*(3), 362–371.

Matsumoto, R., H. Tomaru, Y. Chen, H. Lu, and I. D. Clark (2005), Geochemistry of the interstitial waters of the JAPEX/JNOC/GSC et al. Mallik 5L-38 gas hydrate production research well, in *Scientific Results from the Mallik 2002 Gas Hydrate Production Research Well Program, Mackenzie Delta, Northwest Territories, Canada*, edited by S. R. Dallimore and T. S. Collett, Bulletin 585, Geological Survey of Canada, Ottawa, 14 p.

Medioli, B. E., N. Wilson, S. R. Dallimore, D. Paré, P. Brennan-Alpert, and H. Oda (2005), Sedimentology of the cored interval, JAPEX/JNOC/GSC et al. Mallik 5L-38 gas hydrate production well, Mackenzie Delta, Northwest Territories, in *Scientific Results from the Mallik 2002 Gas Hydrate Production Research Well Program, Mackenzie Delta, Northwest Territories, Canada*, edited by S. R. Dallimore and T. S. Collett, Bulletin 585, Geological Survey of Canada, Ottawa, 21 p.

Moridis, G. J. (2002), Numerical studies of gas production from methane hydrates; SPE paper 75691, in *SPE Gas Technology Symposium*, Calgary, Canada.

Moridis, G. J., T. S. Collett, S. R. Dallimore, T. Inoue, and T. Mroz (2005), Analysis and interpretation of the thermal test of gas hydrate dissociation in the JAPEX/JNOC/GSC et al. Mallik 5L-38 gas hydrate production research well, in *Scientific Results from the Mallik 2002 Gas Hydrate Production Research Well Program, Mackenzie Delta, Northwest Territories, Canada*, edited by S. R. Dallimore and T. S. Collett, Bulletin 585, Geological Survey of Canada, Ottawa, 21 p.

Peltzer, E. T., and P. G. Brewer (2000), Practical physical chemistry and empirical predictions of methane hydrate stability, in *Natural Gas Hydrate in Oceanic and Permafrost Environments*, edited by M. D. Max, pp. 17–28, Kluwer Academic Publishers, Dordrecht, Netherlands.

Pruess, K. (1991), TOUGH2 - A General Purpose Numerical Simulator for Multiphase Fluid and Heat Flow, Lawrence Berkeley Laboratory Report LBL-15227, *Tech. rep.*

Revil, A. (2000), Thermal conductivity of unconsolidated sediments with geophysical applications, *Journal of Geophysical Research*, *105*(B7), 16,749–16,768.

Rider, M. H. (1996), *The geological interpretation of well logs*, 2 ed., Whittles Publishing, Caithness, Scotland.

Rogers, A. J. (1995), Nonlinear effects in optical fibers, in *Optical Fiber Sensor Technology*, edited by K. T. V. Grattan and B. T. Meggitt, pp. 313–346, Chapman & Hall, London.

Rueff, R. M., E. D. Sloan, and V. F. Yesavage (1988), Heat capacity and heat of dissociation of methane hydrates, *American Institute of Chemical Engineers Journal*, *34*(9), 1468–1476.

Ruppel, C. (2000), Thermal state of the gas hydrate reservoir, in *Natural Gas Hydrate in Oceanic and Permafrost Environments*, edited by M. D. Max, pp. 29–42, Kluwer Academic Publishers, Dordrecht, Netherlands.

Sass, J. H., A. H. Lachenbruch, and R. J. Munroe (1971), Thermal conductivity of rocks from measurements on fragments and its application to heat-flow determinations, *Journal of Geophysical Research*, *76*(14), 3391–3401.

Schön, J. H. (1996), *Physical Properties of Rocks*, *Handbook of Geophysical Exploration. Section I, Seismic Exploration*, vol. 18, Pergamon, Oxford, U.K.

Sloan, E. D. (1998), *Clathrate hydrates of natural gases*, 2 ed., 705 pp., Marcel Dekker, Inc., New York.

Somerton, W. H. (1992), *Thermal Properties and Temperature-Related Behavior of Rock/Fluid Systems*, *Developments in Petroleum Science*, vol. 37, 257 pp., Elsevier, Amsterdam, Netherlands.

Spangenberg, E. (2001), Modeling of the influence of gas hydrate content on the electrical properties of porous sediments, *Journal of Geophysical Research*, *106*(B4), 6535–6548.

Stefan, J. (1891), Über die Theorie der Eisbildung, insbesondere über die Eisbildung im Polarmeere, *Annalen der Physik und Chemie*, *42*, 269–286.

Stoll, R. D., and G. M. Bryan (1979), Physical properties of sediments containing gas hydrates, *Journal of Geophysical Research*, *84*(B4), 1629–1634.

Takahashi, H., E. Fercho, and S. R. Dallimore (2005), Drilling and operations overview of the Mallik 2002 Production Research Well Program, in *Scientific Results from the Mallik 2002 Gas Hydrate Production Research Well Program, Mackenzie Delta, Northwest Territories, Canada*, edited by S. R. Dallimore and T. S. Collett, Bulletin 585, Geological Survey of Canada, Ottawa, 17 p.

Taylor, A. E. (1979), Thermal regime modelled for drilling and producing in permafrost, *Journal of Canadian Petroleum Technology*, *18*(2), 59–66.

Taylor, A. E. (1999), Modelling the thermal regime of permafrost and gas hydrate deposits to determine the impact of climate warming, Mallik field area, in *Scientific Results from JAPEX/JNOC/GSC Mallik 2L-38 Gas Hydrate Research Well, Mackenzie Delta, Northwest Territories, Canada*, edited by S. R. Dallimore, T. Uchida, and T. S. Collett, Bulletin 544, pp. 391–401, Geological Survey of Canada, Ottawa.

Taylor, A. E., and A. S. Judge (1981), Measurement and prediction of permafrost thickness, arctic Canada, in *51st Annual Meeting*, vol. 6, pp. 3964–3977, Society of Exploration Geophysicists, Los Angeles, CA, United States.

Taylor, A. E., M. M. Burgess, A. S. Judge, V. Allen, and A. Wilkinson (1998), Canadian Geothermal Data Collection - deep permafrost temperatures and thickness of permafrost, in *Global Geocryological Database, CAPS version 1, CD-ROM*, International Permafrost Association and the National Snow and Ice Data Centre, Boulder.

Troschke, B., and H. Burkhardt (1998), Thermal conductivity models for two-phase systems, *Physics and Chemisty of the Earth*, *23*(3), 351–355.

Waite, W. F., B. J. deMartin, S. H. Kirby, J. Pinkston, and C. D. Ruppel (2002), Thermal conductivity measurements in porous mixtures of methane hydrate and quartz sand, *Geophysical Research Letters*, *29*(24), 2229, doi:10.1029/2002GL015988.

Wiersberg, T., J. Erzinger, M. Zimmer, J. Schicks, and E. Dahms (2005), Real-time gas analysis at the JAPEX/JNOC/GSC et al. Mallik 5L-38 gas hydrate production research well, in *Scientific Results from the Mallik 2002 Gas Hydrate Production Research Well Program, Mackenzie Delta, Northwest Territories, Canada*, edited by S. R. Dallimore and T. S. Collett, Bulletin 585, Geological Survey of Canada, Ottawa, 15 p.

Winters, W. J., S. R. Dallimore, T. S. Collett, B. E. Medioli, R. Matsumoto, T. J. Katsube, and P. Brennan-Alpert (2005), Relationships of sediment physical properties from the JAPEX/JNOC/GSC et al. Mallik 5L-38 gas hydrate production research well, in *Scientific Results from the Mallik 2002 Gas Hydrate Production Research Well Program, Mackenzie Delta, Northwest Territories, Canada*, edited by S. R. Dallimore and T. S. Collett, Bulletin 585, Geological Survey of Canada, Ottawa, 9 p.

Wisian, K. W., D. D. Blackwell, S. Bellani, J. A. Henfling, R. A. Normann, P. C. Lysne, A. Förster, and J. Schrötter (1998), Field comparison of conventional and new technology temperature logging systems, *Geothermics*, *27*(2), 131–141.

Woodside, W., and J. H. Messmer (1961), Thermal conductivity of porous media, *Journal of Applied Physics*, *32*, 1688–1699.

Wright, J. F., F. M. Nixon, S. R. Dallimore, J. Henninges, and M. M. Côté (2005), Thermal conductivity of sediments within the gas-hydrate-bearing interval at the JAPEX/JNOC/GSC et al. Mallik 5L-38 gas hydrate production research well, in *Scientific Results from the Mallik 2002 Gas Hydrate Production Research Well Program, Mackenzie Delta, Northwest Territories, Canada*, edited by S. R. Dallimore and T. S. Collett, Bulletin 585, Geological Survey of Canada, Ottawa, 10 p.